Heat Transfer Correlations in Nuclear Reactor Safety Calculations

Vol. II

HEAT TRANSFER CORRELATIONS IN
NUCLEAR REACTOR SAFETY CALCULATIONS
SÄK-5

H. Abel-Larsen, Risø
A. Olsen,   Risø
J. Miettinen,   VTT
T. Siikonen,   VTT
J. Rasmussen,   IFE
A. Sjöberg,   Studsvik
K. Becker,   KTH

June 1985

Risø: Risø National Laboratory, Denmark
VTT: Technical Research Centre of Finland
IFE: Institute for Energy Technology, Norway
Studsvik: Studsvik Energiteknik AB, Sweden
KTH: Royal Institute of Technology, Stockholm, Sweden

LIST OF CONTENTS

FIGURES.   Page

TABLES

APPENDIX A. PRESENT KNOWLEDGE

A1. Nucleate boiling and forced convective boiling

A literature search is reported in (7). Table A1.I taken from (18) contains four of the best known correlations for nucleate boiling and forced convective flow. Both experimental data and comparisons with different correlations are reported. The comcomparisons are of correlations with experimental data typical for steam generator conditions.

Correlations by Levy and Borishansky gave the best results with an RMS-error of 22-23%.

Two new correlations for bulk boiling and subcooled boiling are also presented in (18). They gave RMS-errors of 16 and 12%, respectively, for their own experimental data. The correlations are given in Table A1.II.

Stephan and Auracher (19) have presented new correlations for nucleate boiling and forced convective boiling heat transfer. The correlations are developed from a large set of data points (5000) using regression analysis. The correlations are given in Table A1.II.

It should be noted that these new correlations in Table A1.II can be written in the form:

$$h_{NcB} = F(B) \cdot q''^A$$

with $A \sim 0.65 - 0.7$.

This is also the case for the correlations by Levy and Borishansky.

TABLE A1.I.

Authors	Correlations	RMS with CNEN data %
Thom	$$T_w - T_{SAT} = 22.52 \cdot \left(\frac{q''}{10^6} \right)^{1/2} \cdot \exp(-0.0115 \cdot P)$$ P in bar	59.6
Levy	$$T_w - T_{SAT} = 0.9128 \cdot q''^{1/3} \cdot P^{-4/9}$$ P in bar	22.4
Chen	$$h_b = h_{mac} + h_{mic}$$ $$h_{mac} = h_f \cdot F$$ $$h_{mic} = 0.00122 \cdot \left(\frac{k_f^{0.49} \cdot C_{pf}^{0.45} \cdot \rho_f^{0.49}}{\sigma^{0.5} \cdot \mu_f^{0.29} \cdot H_{fg}^{0.24} \cdot \rho_g^{0.24}} \right) \cdot$$ $$\left(\frac{H_{fg}}{T_{SAT}(v_g - v_f)} \right)^{0.75} \cdot \Delta T_{SAT} \cdot S$$ $$F = f\left(\frac{1}{X_{tt}} \right) \; ; \; S = f(Re_{TP}); \; Re_{TP} = Re_f \cdot F^{1.25}$$	35.0
Borishansky	$$h_b = h_{pk} \cdot \left(1 + 7 \cdot 10^{-9} \cdot \left(\frac{w_m \cdot H_{fg} \cdot \rho_f}{q''} \right)^{3/2} \right)^{1/2}$$ $$w_m = \frac{G}{\rho_f} \cdot \left(1 + \frac{\rho_f - \rho_g}{\rho_g} \cdot X \right)$$ $$h_{pk} = h_k \cdot \left(1 + \left(\frac{h_\infty}{h_k} \right)^2 \right)^{1/2}$$ $$h_k = 0.023 \cdot \frac{k_f}{D} \cdot \left(\frac{G \cdot D}{\mu_f} \right)^{0.8} \cdot Pr_f^{0.4}$$ $$h_\infty = 0.1379 \cdot (P^{0.14} + 1.88 \cdot 10^4 \cdot P^2) \cdot \left(\frac{q''}{10^4} \right)^{0.7}$$ P in bar	22.9

TABLE A1.II.

Origin	New correlations for boiling heat transfer	RMS %
CNEN (bulk boiling)	$$h_b = 150 \cdot \frac{k_\ell}{D} \left(\frac{q'' \cdot \sqrt{\frac{\sigma}{g \cdot (\rho_\ell - \rho_g)}}}{H_{fg} \cdot \mu_\ell} \right)^{0.65}$$ $$\cdot \left(1 + 10^{-4} \cdot \frac{H_{fg} \cdot G}{q''} \right) \cdot \left(1 + \frac{1}{X_{tt}} \right)^{0.13} \cdot Pr_g$$	16
CNEN (subcooled boiling)	$$h_{sb} = \frac{q''}{\Delta T_{CNEN} + (\Delta T_{DB} - \Delta T_{CNEN}) \cdot \left(\frac{H_{SAT} - H(z)}{H_{SAT} - H_o} \right)^{0.5}}$$ $\Delta T_{CNEN} = q''/h_b$ and $\Delta T_{DB} = q''/h_{DB}$ (DB: Dittus-Boelter)	12
Stephan & Auracher (nucleate boiling)	$$h_{NcB} = \frac{k_\ell}{D} \cdot 0.246 \cdot 10^7 \cdot \left(\frac{\kappa_\ell^2}{H_{fg} \cdot D^2} \right)^{1.58}$$ $$\cdot \left(\frac{q'' \cdot D}{k_\ell \cdot T_{SAT}} \right)^{0.673} \cdot \left(\frac{c_{p\,\ell} \cdot T_{SAT} \cdot D^2}{\kappa_\ell^2} \right)^{1.26}$$ $$\cdot \left(\frac{\rho_\ell - \rho_g}{\rho_\ell} \right)^{5.22}$$	11.3
Stephan & Auracher (forced convective boiling	$$h = h_{NcB} \cdot 29 \cdot (Re_\ell)^{-0.3} \cdot (Fr_\ell)^{0.2}$$ $$Re_\ell = \frac{G \cdot (1-X) \cdot D}{\mu_\ell} \quad ; \quad Fr_\ell = \frac{G^2 \cdot (1-X)^2}{\rho_\ell^2 \cdot g \cdot D}$$	10
J. Rasmussen	$h_{NcB} = B1(P) \cdot (T_w - T_{SAT})$ $B1(P) = 2000 + 80 \cdot P - 1548 \cdot \exp(-0.175 \cdot P)$ $\qquad\qquad + 37.5 \cdot (\exp(0.04815 \cdot P - 1) \quad ;$ P in bar	

The correlations by Stephan and Auracher seem to perform quite well. They should, however, also be tested against the data base in (18). If this test comes out well, the correlations may be recommended for steam generator calculations.

Chen's correlation is considered as one of the best candidates for nuclear reactor core calculations. It should be remembered, however, that Chen's correlation is based mainly on low-pressure data with only a few data at higher pressures (P < 70 bar). A correlation that interpolates between Chen and Thom is suggested in (7) for pressures from 70 to 140 bar. This correlation is a simplification of Chen and is much simpler to use in a computer programme.

A2. Critical heat flux

A literature search is reported in (7). There are two classes of CHF-situations; DNB (Departure from Nucleate Boiling) in liquid continuous flow and DO (Dry Out) or DFCB (Departure from Forced Convective Boiling) in vapour continuous flow.

Most of the CHF-corelations are based on the concept of equilibrium flow with one vapour and one liquid component. The determination of CHF follows, using an appropriate correlation. One of four methods are used:

1. Heat flux versus local quality (q_c''/X).
    ("Local conditions" hypothesis).

    It is assumed that there is an unique relationship between CHF and l o c a l vapour quality. The method has a tendency to fail when applied to data with strong non-uniformity in axial heat flux.

2. The "Overall power" hypothesis.

    This method suggests that the total power that can be fed into a non-uniformly heated channel will be the same

as for a uniformly heated channel with the same geometry and inlet conditions. No prediction of the location of CHF is carried out. This method is found (20) to be slightly more accurate than the above-mentioned method for axially symmetrical non-uniform heat flux.

3. Critical quality versus boiling length (X_c/L_b).
    ("Equivalent length" hypothesis).

    The method suggests that the CHF is not a local phenomenon but an integral one i.e. it is dependent on the history of what has occurred upstream. The equivalent length is defined as:

    $$L_e = \frac{1}{q''} \cdot \int_0^L q''(z) \, dz$$

    The method tends to perform better for non-uniform heat flux situations.

4. The F-factor method by Tong.

    Similar to the equivalent length method, this is an integral method. The F-factor is defined as:

    $$F = \frac{(q''_c)_U}{(q''_c)_{NU}}$$

    where $(q''_c)_U$ is the value of the critical heat flux at any given local enthalpy for the uniform heat flux case and $(q''_c)_{NU}$ is the value of the critical heat flux at the same local enthalpy for the particular non-uniform heat flux case.

Another class of correlations or models are the so-called phenomenological models, which actually attempt to model the physical effects. Hewitt states in (21) that analytical models on CHF produce results which are comparable in accuracy to empirical correlations and which can be extrapolated over

much wider ranges. At present, these models are developed and tested for only simple geometries and annuli. More development is also needed in improving these models and obtaining better confidence in the description of the different processes such as deposition and entrainment. These models would require computer programmes where the different flow components are actually modelled.

Computer programmes like RELAP, TRAC and NORA model only one liquid component, and the application of any phenomenological model for CHF would need considerable programming effort. In a LOCA situation one therefore usually relies on empirical correlations based on the local conditions hypothesis. Leung (22) has made a comparison of such correlations with experimental observations from transient experiments.

Table A2.I reviews the correlations tested by Leung. The Westinghouse correlation (W-3), which is still used for design, was developed for low-quality CHF (DNB) at or above 7 MPa. At qualities > 0.5 and pressures below 12 MPa, the correlation yields negative CHF values. The W-3 correlation was not used by Leung due to this abnormal behaviour.

The correlations mentioned in Table A2.I are all listed in (7). The data base used by Leung consisted of more recent data on CHF in transient conditions.

Leung concluded that an appropriate steady-state CHF correlation was adequate to use for the prediction of CHF onset during a wide range of flow transients. The local conditions hypothesis was demonstrated to predict the trend of CHF data better than the equivalent-length hypothesis. In one test, the incapability to predict a CHF was a result of a discrepancy found in correlating the steady-state CHF data.

Further, it was recommended to use Griffith-Zuber in the following mass flux range:

$$-240 < G < 100 \text{ kg/m}^2/\text{s}.$$

TABLE A2.I. CHF correlations tested by Leung

Correlations	Geometry	Pressure MPa	Mass flux kg/m^2/s	Quality	Remarks
Bowring	Round tube	0.2-19	136-18600	all X	3792 points
Biasi	Round tube	0.3-14	100- 6000	~ 0-1.0	4500 points
CISE	Round tube	4.5-15	~ 100- 4000	~ 0-1.0	Freon data
B & W-2	Rod bundle	14 -16.6	1017- 5430	-0.03 to 0.20	Only DNB data
CONDIE MOD7	Rod bundle	3.0-17	70- 4700	-0.1 to 1.0	5163 points
GE	Rod bundle	6.9	< 680	0-0.84	Low flow data
Hsu-Beckner	Rod bundle	6-15	All	~ 0-1.0	Blowdown data
Griffith	Short annulus	All range	Low G	0-1.0	Counter current

Outside this mass flux range Biasi and CISE are said to be equally good possibilities.

Some work on steady-state CHF for steam generator conditions is described in (23). Their own experimental data in addition to data from CISE (24) and Becker (25) were compared with some CHF correlations. The data were from vapour continuous region, i.e. in the deposition-controlled region, and the transition region between liquid continuous (DNB-region) and the vapour continuous region (DO-region). The results of the comparison are summarized in Table A2.II.

TABLE A2.II. Testing of CHF correlations

Correlation	Dep. contr. region 137 data points		Dep. contr. + trans. region 290 data points	
	RMS %	Av. error %	RMS %	Av. error %
Biasi	12.6	8.7	18.7	15.2
Becker	11.9	8.2	17.9	14.3
Bowring	23.7	19.6	17.9	13.3
CISE	9.7	8.6	7.9	6.5
Macbeth-Th.	8.7	6.9	10.2	7.9
ROKO	7.8	6.2	17.5	13.8
CNEN	4.5	3.9	4.6	3.6

Besides their own correlation developed to fit these data, the CISE correlation seems to give the best performance. These results may therefore be seen as a support for the general applicability of the CISE correlation. It is remarked that according to Becker (private communication), his correlation is here in part used outside the range of applicability.

A3. Transition boiling

The heat transfer in the transition boiling region (C-D in Fig. 1) is described in (26). A literature search is reported in (27).

Groeneveld gives in (28) an excellent review of post-CHF heat transfer up to ~ 1974. Table A3.I shows three newer transition boiling heat transfer correlations from his compilation (nos. 1 to 3).

A few correlations have been published since then. In Table A3.I two correlations are shown. Number 4 is the correlation by Chen et al. (29). The correlation is together with no. 1 an attempt to make a phenomenological correlation. The last correlation in the table (no. 5) is an example of a purely empirical one. It is proposed by Bjornard and Griffith and used in TRAC.

Iloeje et al. (30) proposed a 3-step model as indicated in the table and illustrated in Fig. A3.1. Iloeje has only one step covering the contact period, B, C and D in Fig. A3.1. Chen uses also a 3-step model with all 3 steps in the touching period: waiting period, bubble nucleation- and growth-period and a liquid film evaporation period. Convection to bulk vapour is calculated using the Reynold's momentum analogy modified by Colburn.

The fraction of wall hit and wetted by droplets is determined empirically from experimental data taken from 8 different references (4167 points) ranging in pressures from 4 to 195 bar, mass fluxes from 15 to 3000 kg/m^2/sec, heat fluxes from 3 to 165 watt/cm^2 and equilibrium qualities from 0.5 to 1.7.

The fraction is determined using the relation:

$$FL = \frac{q_T'' - q_{Vc}''}{q_{Lc}'' - q_{Vc}''}$$

where q_T'' is the total heat flux, q_{Vc}'' the convective heat flux calculated, as mentioned above, and q_{Lc}'' the liquid contact heat flux.

The liquid contact area fraction, or the decay factor as designated by Tong and Young (see below), FL could be correlated as:

TABLE A3.I.

Correlations	Range of applicability
$$q'' = C \left[\frac{R \cdot \sigma \cdot C_{p\ell} \cdot \rho_\ell \cdot T_{SAT}^2}{P_\ell \cdot H_{fg}} \right] \cdot \left[\frac{1-XE}{XE} \right] \cdot$$ $$\frac{U_g \sqrt{f}}{\delta} \cdot \exp\left[-\frac{\Delta T_{SAT}}{\Delta T_{max}} \right] +$$	Heat transfer to a single drop touching the wall
$$\lambda \cdot (1-\alpha) \cdot \left[1 - \exp\left(-\frac{\Delta T_{SAT}}{\Delta T_{max}} \right) \right] \cdot \frac{4 \cdot k_{vg}}{\delta} \cdot$$ $$\left[\left(1 + \frac{2 \cdot \lambda_{mw}}{\delta} \right) \cdot \ln\left(1 + \frac{\delta}{2 \cdot \lambda_{mw}} \right) - 1 \right] \cdot \Delta T_{SAT}$$	Heat transfer to drops in thermal boundary layer, but not touching the wall
$$+ 0.023 \cdot \frac{k_g}{D} \left[\frac{G \cdot D}{\mu_g} \left(XE + (1-XE) \frac{\rho_g}{\rho_\ell} \right) \right]^{0.8} \cdot$$ $$\left(\frac{\mu C_p}{k} \right)_g^{0.4} \cdot \Delta T_{SAT} \ ;$$	Heat transfer to bulk vapour
$$\lambda_{mw} = \varepsilon \cdot \left[\frac{\Delta T_{SAT}}{\Delta T_{max}} \Big/ \left[1 - \exp\left(\frac{\Delta T_{SAT}}{\Delta T_{max}} \right) \cdot \right. \right.$$ $$\left. \left. \left(1 + \frac{\Delta T_{SAT}}{\Delta T_{max}} \right) \right] \right]^{1/3}$$ ΔT_{max} given by $$\frac{k_g \cdot \Delta T_{max}}{G \cdot D \cdot H_{fg}} = 3.27 \cdot 10^{-5} \ (2.93 +$$ $$4.44 \cdot XE + 2.923 \cdot 10^{-6} \cdot (G \cdot XE)^2 -$$ $$1.51 \cdot 10^{-6} \cdot (G \cdot XE)^3) \Big/ \left(\frac{G \cdot D}{\mu_g} \right)^{0.477}$$ C: Correlation constant λ: Geometric parameter	P: 6.89 MPa G: 410-1700 kg/m$^2 \cdot$s X: 0.1-0.7 Geometry: tube
Iloeje et al. (30) 1.	

TABLE A3.I.   (cont.)

Correlations	Range of applicability

$q''_{TB} = q''_{NCB} \cdot FLT + q''_{VCT} \cdot (1-FLT)$
 	
 q''_{NCB} e.g. Chen
 	
 $q''_{VCT} = \dfrac{k_v}{D} \cdot (Re)^{0.8} \cdot (Pr)^{0.4} \cdot 0.023 \cdot$
 	
 $(T_w - T_v)$;
 	
 $Re = \dfrac{V_m \cdot \rho_v \cdot D}{\mu_v}$;
 	
 $V_m = \dfrac{G}{\rho_\ell} \cdot \dfrac{S \cdot (1-XA) + XA \cdot \rho_\ell / \rho_g}{S \cdot (1-XA) + XA}$;
 	
 $FLT = \exp\left[-3.937 \cdot 10^{-2} \cdot \dfrac{XE^{0.667}}{dXE/dL} \cdot \right.$
 	
 $\left. (1.8 \cdot 10^{-2} \cdot (T_w - T_{SAT}))^{(1+2.88 \cdot 10^{-3} \cdot (T_w - T_{SAT}))} \right]$
 	
 Tong & Young (31)
 	
 2.
	P: 6.89 MPa
	  G: 410–5160
	  $kg/m^2 \cdot s$
	 XE: 0.2–1.45
	  Geometry: tube
	
	 P: 3.45–9.65 MPa
	
	  G: 680–4210
	  $kg/m^2 \cdot s$
	
	  XE: 0.15–1.10
	
	  Geometry: annulus
	 & rod bundle
	
	 5.6 < ΔT_{SAT} < 560
	
	 ρ_g: Density at
	   saturation
	
	 ρ_v: Density at
	   superheating

$q''_{TB} = (h_{FB} + h_C) \cdot (T_w - T_{SAT})$;
 	
 $h_{FB} = 0.62 \cdot \left[\dfrac{k_v^3 \cdot g \cdot \rho_v (\rho_\ell - \rho_v) \cdot H'_{fg} \cdot LaP}{\mu_v \cdot \Delta T_{SAT}} \right]^{1/4}$;
 	
 $LaP = \dfrac{1}{2\pi} \cdot \sqrt{\dfrac{g \cdot (\rho_\ell - \rho_v)}{\sigma}}$;
 	
 $H'_{fg} = H_{fg} + 0.55 \cdot c_{p,v} \cdot \Delta T_{SAT}$
 	
 p.t.o.
	P: 0.103–0.620 MPa
	
	 G: 50–250
	  $kg/m^2 \cdot s$
	
	 Geometry: 100 rod
	  bundle (FLECHT)

TABLE A3.I.   (cont.)

Correlations	Range of applicability
$h_c = A \cdot \exp(-B \cdot (T_w - T_{SAT}))$ $A = 59.68 \cdot (P)^{0.558}$ $B = 1.459 \cdot 10^{-3} \cdot (P)^{0.1733}$ Hsu (32) 3.	
$q''_{TB} = q''_{LC} \cdot FL + q''_{VC} \cdot (1-FL)$ $q''_{VC} = h_{VC} \cdot (T_w - T_v)$ $h_{VC} = f/2 \cdot G \cdot XA \cdot c_{pv} \cdot Pr^{-2/3}$ $1/\sqrt{f} = 3.48 - 4 . LOG\left(\dfrac{\varepsilon}{D} + \dfrac{9.35}{(Re \cdot \sqrt{f})}\right)$ $Re = \dfrac{D \cdot \rho_v \cdot j}{\mu_v}$ $j = \dfrac{G \cdot XA}{\rho_v} + \dfrac{G \cdot (1-XA)}{\rho_\ell}$ $\dfrac{XA}{XE} = \dfrac{H_{fg}}{H_{fg} + c_{pv} \cdot (T_w - T_{SAT}) \cdot \left(\dfrac{TD}{1+TD}\right)}$ and $\dfrac{XA}{XE} = 1 - B(P) \cdot TD$ $T_D = \dfrac{T_v - T_{SAT}}{T_w - T_v}$ p.t.o.	P: 4-195 bar G: 16-3000 $kg/m^2 \cdot s$ XE: 0.5-1.7 q'': 3-165 W/cm^2 (4167 data points 8 refs.)

TABLE A3.I.   (cont.)

Correlations	Range of applicability
$$B(P) = \frac{0.26}{1.15 - (P/P_c)^{0.65}}$$ $$q''_{LC} = \frac{q''_a + q''_b + q''_c}{t_1 + t_2 + t_3}$$ **Waiting period** $$q''_a = \frac{R \cdot \sigma \cdot \rho_\ell \cdot c_{p\ell} \cdot T_{SAT}^2}{0.213 \cdot P \cdot H_{fg}}$$ $$t_1 = \frac{R \cdot \sigma \cdot T_{SAT}^2}{0.24 \cdot P \cdot H_{fg} \cdot \sqrt{a_\ell}} \cdot \left(\frac{R_T + 1}{R_T} \cdot \frac{1}{T_w - T_{SAT}} \right)^2$$ $$R_T = \left(\frac{k_w \cdot \rho_w \cdot c_{pw}}{k_\ell \cdot \rho_\ell \cdot c_{p\ell}} \right)^{0.5}$$ **Nucleation period** $$q''_b = 0$$ $$R^+ = 2/3 \cdot \left[(t^+ + 1)^{2/3} - (t^+)^{2/3} - 1 \right]$$ $$R^+ = \frac{M1}{(M2)^2} \cdot R(t) \quad ; \quad R(t) \text{ input}$$ $$t^+ = \frac{(M1)^2}{(M2)^2} \cdot t_2$$ $$M2 = \left(\frac{12 \cdot a_\ell}{\pi} \right)^{0.5} \cdot \left(\frac{\rho_\ell}{\rho_v} \right) \cdot \left(\frac{c_{pf}}{H_{fg}} \right) \cdot (T_w - T_{SAT})$$ $$M1 = \left[2/3 \cdot \left(\frac{\rho_v}{\rho_\ell} \right) \cdot \frac{T_w - T_{SAT}}{T_{SAT}} \cdot H_{fg} \right]^{0.5}$$ p.t.o.	

TABLE A3.I.   (cont.)

Correlations	Range of applicability
Evaporation period $$q_c'' = \frac{8 \cdot \sigma \cdot T_{SAT}}{T_w - T_{SAT}} \cdot \frac{\rho_\ell}{\rho_g}$$ $$t_3 = \frac{32 \cdot \rho_\ell \cdot \sigma^2}{k_\ell \cdot \rho g \cdot H_{fg}} \cdot \frac{T_{SAT}^2}{(T_w - T_{SAT})^3}$$ $$FL = \exp(-\lambda \cdot (T_w - T_{SAT})^{0.5})$$ $$C2 = \frac{5.0 \cdot 10^{-3}}{(1-\alpha)^{40} + 9.0 \cdot 10^{-3} \cdot \alpha}$$ $C1 = 24 \cdot C2$ $C3 = 0.2 \cdot C2$ $C4 = 7.3733 \cdot 10^{-4}$ $(\lambda 1) = (C1 - C2 \cdot C4 \cdot G) \cdot 1.341$ $(\lambda 2) = C3 \cdot C4 \cdot G \cdot 1.341$ $\lambda 1$ or $\lambda 2$, whichever is greater Chen et al. (29) **4.**	
$$q_{TB}'' = q_{CHF}'' \cdot FLB + q_{MFB}'' \cdot (1 - FLB)$$ $$FLB = \left(\frac{T_w - T_{MFB}}{T_{CHF} - T_{MFB}} \right)^2$$ $$T_{MFB} = T_{MS} + \frac{T_{MS} - T_{SAT}}{R_T}$$ $$T_{MS} = T_K \cdot \left(1 - 0.095 \cdot \left(1 - \frac{T_{SAT}}{T_K} \right)^8 \right)$$ Bjornard & Griffith (33) **5.**	
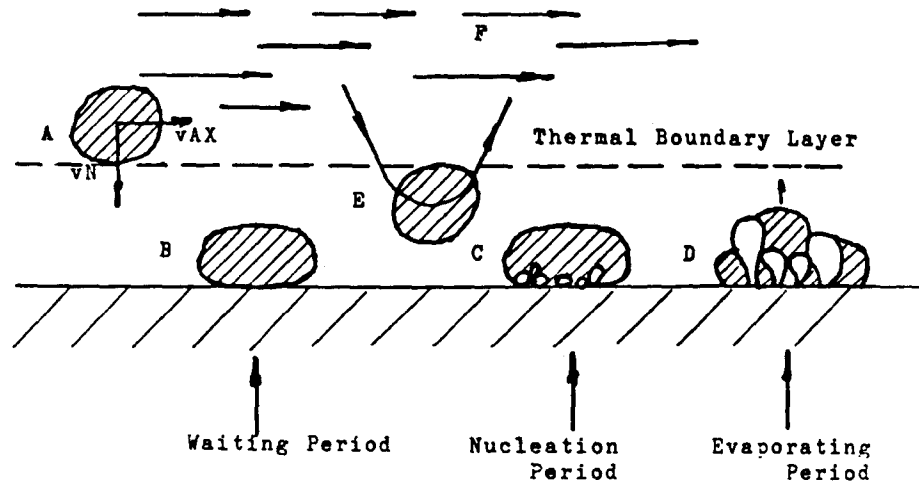
A. Liquid drop entering thermal boundary layer with
   velocity $[v_N]$ normal to wall.
B. Liquid drop of higher kinetic energy based on $[v_N]$
   arriving on wall and beginning to absorb heat
   from wall via conduction.
C. Nucleation and bubble growth in liquid drop on wall.
D. End of bubble growth period. Part of liquid drop is
   ejected into the main stream by escaping vapour
   bubbles, part is left on wall to evaporate.
E. Liquid drop of lower kinetic energy in thermal
   boundary layer and being reversed into the main
   flow without touching the wall.
F. Bulk vapour flow.

FIGURE A3.1.

$$FL = \exp(-\lambda \cdot (T_w - T_{SAT})^n)$$

λ is a function of void and mass flux as shown in Table A3.I. The exponent n was determined to be 0.5.

The Chen correlation does take the thermodynamic nonequilibrium into account, i.e. part of the heat goes to superheat the vapour instead of evaporating the droplets and the actual vapour quality, XA, is less than the equilibrium quality, XE.

The Tong and Young correlation is also discussed in (26). It is a two-term correlation as the Chen correlation with a boiling term and a convective term. Tong and Young use the nucleate boiling heat flux at CHF as the boiling term and a modified single-phase heat tansfer correlation (Dittus-Boelter) as the convective term.

The decay factor has been empirically determined from some high-pressure experimental data (69 bar). It shows also an exponential decay and depends on the wall temperature and the quality.

The Chen- and Tong & Young-correlations are based on experimental data in vapour continuous flow and may be used only under such flow conditions.

The Hsu correlation, no. 3 in Table A3.I, is based on FLECHT data (subcooled data), and can be used in liquid continuous flow (inverse annular flow).

As a consequence of the scarcity of reliable and consistent data on transition boiling heat transfer,the simple interpolation between the CHF and the minimum film boiling heat flux is still used. The Bjornard and Griffith corelation, no. 5 in Table A3.I, is an example.

Kirchner and Griffith (34) have proposed another way of interpolating the boiling curve in the transition region:

$$h_{TB} = \frac{q''_{TB}}{\Delta T} = \frac{q''_{CHF}}{\Delta T} \cdot \left(\frac{T_w}{T_{CHF}} \right)^{XPNT}$$

where

$$XPNT = \frac{\ln(q''_{CHF}) - \ln(q''_{MFB})}{\ln(T_{CHF}) - \ln(T_{MFB})}$$

The correlation has been tested against FLECHT data with reasonable agreement.

The Bjornard & Griffith-, the Chen- and the Tong & Young-correlations are compared with experimental, temperature-controlled data. The results of this comparison are discussed in Appendix B4.2.

The following phenomenological decomposition of the heat transfer not only in the transition boiling region, but in all post-CHF regions, where droplets may be of importance in the total transport of energy from a heated surface to a two-phase mixture, is generally accepted:

1. Heat transfer from the surface to liquid droplets, which impinge on the wall ("wet" collisions)

2. Heat transfer from the surface to liquid droplets, which enter the thermal boundary layer without wetting the surface ("dry" collisions)

3. Convective heat transfer from the surface to the vapour

4. Convective heat transfer from the vapour to the dispersed droplets in the vapour (interfacial heat transfer)

5. Heat transfer by thermal radiation from the surface to the liquid

6. Heat transfer by thermal radiation from the surface to the vapour.

A4. Rewetting

Introduction and recommendation

In the middle of 1970 the experimental and modelling work around the rewetting mechanism by bottom reflooding and by top spray cooling was comprehensive, but very dispersed without any well-defined goal. The studies produced several mathematical models and many empirical proposals for the fitting factors in the models. In bottom reflooding and falling film cooling of the overheated fuel rod the length of the transition boiling region is short compared with other flow regions. This transition boiling region is in fact normally considered as a rewetting front. Due to the sharp temperature gradient over the front the heat from the hot, unwetted part is moved to the cold, wetted part by an axial conduction in the fuel rod cladding.

Because most of the computer programmes don't divide the heat structure into mesh intervals on the order of few millimeters, the usual heat structure models are unable to calculate properly the axial conduction effect, although the two dimensional heat conduction was solved for the rod structure. That is the reason why there are good arguments for a special handling of the rewetting mechanism in emergency core cooling programmes.

RELAP-4/MOD-6 includes a model describing the rewetting mechanism with the moving-mesh techniques. The axial conduction is not modelled in the programme and the axial conduction effect was replaced by an increment in the transition boiling coefficient. The result, e.g. from the CSNI standard problem 7 for reflooding indicated that no universally good user dials may be proposed for RELAP-4/Mod-6 users, when the transition boiling approach has been used.

RELAP5/Mod2 includes a rewetting model that uses the two-dimensional heat conduction equation for the core heat slabs. In the rewetting front the programme doubles or halves the structure nodes, depending on the temperature gradient in the rewetting front. The recommendation for fixed-core heat slab

dimensions is on the order of 0.10 m. For the fine-mesh division a minimum mesh length of 0.001 m is recommended. According to earlier calculations as well as the numerical study with the PHOENICS programme, numerical modelling of the two-dimensional heat conduction equations for the rewetting is close to the analytical solution if the mesh length in the front is less than 0.001 m. Thus in the rewetting calculation the recommended minimum 0.001 m may be seen as the maximum. There has been no known experience with the RELAP5/MOD2 rewetting model to date. It may may be expected that the use of a very fine mesh division increases the computation time.

The German programme for emergency core cooling (FLUT), having six field equations has been developed in the last 7 years and results obtained for the reflooding process show a good agreement with experimental results. The programme applies the old techniques where the axial conduction is modelled with a mathematical correlation and usually with two fitting factors.

Work reported in (35) showed that the experimental data published in the 1970's and expressed as correlations with fitting factors gave a large scatter between different proposals for the fitting factors in the correlations. The correlations are asymptotic solutions of the original differential equations. The advantage with this kind of correlations is that in the temperature solution only one halving procedure is needed for the axial heat structure around the rewetting front and thus no extra computing time is needed for the fine mesh.

Due to these experiences two possibilities may by seen with respect to the rewetting modelling. The classical method describing the rewetting mechanism as a mathematical formula and as fitting factors in it may be recommended as one possibility. The method may be recommended especially when large computational times for the fine mesh structure have to be avoided.

The other possibility is the method using the fine-mesh techniques, i.e. the coarse mesh interval around the rewetting front is divided into a fine mesh ranging from 0.0002 to 0.001 m.

The method may be recommended if the computing time is avail-
able. If meshes are used that are too coarse for the rewetting
front, the rewetting speed resulting from the calculation
deviates totally from the exact solution. Thus the method is
recommended only if a sufficiently fine mesh is possible to
use. In many applications the exact modelling of temperatures
close to the rewetting front is not as interesting as the maxi-
mum wall temperatures.

Due to these experiences it may be recommended that the re-
wetting mechanism should be described by using the classical
method:a correlation with two fitting parameters. This classical
approach is considered more closely below.

Mathematical rewetting models

For reasons of simplicity the fuel rod cladding is considered
as a slab. The unstationary heat conduction may be written as

$$\rho \cdot c \cdot \frac{\partial T}{\partial t} = k \left(\frac{\partial^2 T}{\partial y^2} + \frac{\partial^2 T}{\partial z^2} \right) \qquad (1$$

In the moving mesh method this equation is solved numerically.
For the space derivatives the space-centred differencing may
be used. For the time derivative only the backward differencing
is possible, i.e. the implicit solution and thus the solution
needs a matrix inversion technique. The solution of the two-di-
mensional, time-dependent heat conduction equation is included
into RELAP5/MOD2 and TRAC and the equation is solved for core
fuel rods. Around the rewetting front the heat structure is
halved in the axial and radial directions if the temperature
difference between two adjacent mesh cells becomes too high.

In the formulation of the mathematical correlation for the
rewetting front the time-dependent heat conduction equation
(1) is transformed by assuming moving coordinates that move with
the velocity of the rewetting front. The rewetting velocity
is assumed to be constant. The transformation applies the
relationship:

$$\frac{\partial T}{\partial t} = \frac{\partial T}{\partial z} \cdot \frac{\partial z}{\partial t} = u \cdot \frac{\partial T}{\partial z} \tag{2}$$

Further, via relationships:

$$\theta = \frac{T - T_{SAT}}{T_o - T_{SAT}}, \qquad T_o = \text{quenching temperature} \tag{3}$$

$$\eta = z/\delta, \qquad \delta = \text{wall thickness} \tag{4}$$

$$\zeta = y/\delta \tag{5}$$

$$Bi = \frac{h \cdot \delta}{k_w} \qquad h = \text{heat transfer coefficient} \tag{6}$$

$$Pe = \frac{\delta \cdot \rho w \cdot c \cdot u}{k_w} \tag{7}$$

The nondimensional form of the equation may be written:

$$\theta_{\eta\eta} + \theta_{\zeta\zeta} + Pe \cdot \theta_\eta = 0 \tag{8}$$

The boundary conditions are:

$$\theta = 0 \text{ at } \eta = -\infty, \qquad \theta = \theta_w \text{ at } \eta = +\infty \tag{9}$$

$$\theta_\zeta = -0 \qquad \text{at } \zeta = 0, \qquad \theta_\zeta = -Bi \cdot \theta \quad \text{at } \zeta = 1 \tag{10}$$

Equation (8 cannot be solved analytically only the asymptotes may be calculated. If the wall is assumed thin and the rewetting velocity low, the radial derivative $\theta_{\zeta\zeta}$ may be dropped. Further, by assuming $\theta_w \gg 1$, $\theta_w = \theta(T_w)$, the solution for the equation is a widely used formula of Yamanouchi:

$$Pe = Bi^{0.5}/(\theta_w - 1) \tag{11}$$

The two-dimensional approximation may be formulated as the a-symptotic solution for the original equation, by assuming a large rewetting velocity (Pe large) and Pe > Bi. The asymptote of the pure two-dimensional formulation is not very practical because it strongly overpredicts the rewetting velocity at low rewetting velocities. The use of the Yamanouchi model for the rapid rewetting regime underpredicts the velocity, but this can be accepted more easily than the overprediction (conservative).

Dua and Tien have made a useful proposal, however, which fits the fast rewetting and slow rewetting region as well. The calculations with the correlation have shown a good fit to the exact solution. The work is based on the original work of J.G.M. Andersen of Risø, and the following correlation is recommended as a correlation for the rewetting front propagation:

$$Pe = (Bi* \cdot (1 + 0.40 \cdot Bi*))^{0.5}$$
(12

where

$$Bi* = \frac{Bi}{\theta_w \cdot (\theta_w - 1)}$$
(13

Heat transfer correlations for the moving mesh methods

Since reflooding cases have not been included in the test matrix in the SÄK-5 project and because RELAP5/MOD2 was unavailable before the end of 1984, no recommedations may be presented based on computer runs for the heat transfer correlations around the rewetting front. The heat transfer logic of RELAP5/MOD2 is listed, however:

• Nucleate boiling: Jens & Lottes subcooled boiling or Chen correlation.
• Critical heat flux: Zuber correlation multiplied by the correction proposed by Griffith (1-α) and multiplied by the large flow correction $(G/67.82)^{0.33}$, if the mass flux G > 67.82 kg/m$^2\cdot$s.
• Transition boiling: Weissman correlation.

Fitting parameters for the correlation

The fitting parameters in the correlation are the heat transfer coefficient h in the Biot number Bi and the nondimensional re-rewetting temperature θ_0.

Previous work (35) showed that the proposal based on the experimental work of the 1970's is not directly useful due to large scatter. The German FLUT programme, using the rewetting velocity correlation, and RELAP5/MOD2 have similar proposals for the critical heat flux. The proposed critical heat flux may therefore be used as a basis of the heat transfer correlation. It is recommended that the heat transfer coefficient in Biot's number be determined from the Zuber critical heat flux correlation multiplied by the Griffith's correction factor $(1- \alpha)$. The Weisman correction $(G/67.82)^{0.33}$ may be used as well. The heat transfer coefficient is calculated by dividing the critical heat flux by the temperature difference $\Delta T_{CHF} = T_{w,CHF} - T_{SAT}$, which results from the heat transfer calculation in the nucleate boiling region, where e.g. Chen's correlation is used. The heat transfer coefficient h in Biot's number is then:

$$h = q^*_{CHF,Zuber} \cdot (1-\alpha)/(\Delta T_{SAT, \text{Chen NB}}) \tag{14}$$

(For $G>67.82$ $h = h \cdot (67.82)^{0.33}$ may be used)

The minimum film boiling temperature may be defined as the rewetting temperature T_0. One possibility is therefore to use a correlation for this. Another possibility is mentioned, viz. the choice in FLUT:

$$T_0 = T_{SAT} + 160 + 6 \cdot \Delta T_{sub} \tag{15}$$

The third term on the right side takes the subcooling effect into consideration.

The recommended values should be considered as a first guess. The functioning of the rewetting model should be tested together with the whole heat transfer package.

A5. Film Boiling

In order to determine the wall fluid heat transfer when the CHF has been exceeded, it is important to identify the flow regions appearing at different conditions. The different types of post-CHF flow regions are described in Chapter 1.3.

The post-CHF flow regions are generally categorized according to the distribution of the vapour and liquid phases, vapour continuous or liquid continuous (see Fig. 2). The distribution is strongly dependent on the prevailing pre-CHF flow regions and the type of CHF that has occurred. At low quality-CHF the bubbly pre-CHF region will experience a transition to inverted annular flow and further downstream a new transition to inverted slug and finally dispersed droplet flow (Fig. A5.1). At moderate quality CHF the slug or churn-turbulent pre-CHF region will undergo a transition to inverted slug flow with a subsequent transition to dispersed droplet flow. At high quality-CHF the annular or annular mist pre-CHF region will change to dispersed droplet flow (Fig. A5.1).

The transition criteria may be evaluated from (10):
Liquid continuous (Inverted annular flow), when

$$\alpha < \alpha_{tran} - 0.1$$

Transition flow (churn/slug flow), when

$$\alpha_{tran} - 0.1 < \alpha < \alpha_{tran}$$

Vapour continuous (dispersed flow), when

$$\alpha \underset{=}{>} \alpha_{tran}$$

where

$$\alpha_{tran} = \left(1 + \frac{4}{(\rho_\ell / \rho_g)}\right) \cdot \frac{1}{C_0} - \frac{4}{(\rho_\ell / \rho_g)}$$

and

$$C_O = C_\infty - (C_\infty - 1) \cdot (\rho_g/\rho_\ell)^{0.5}$$

$$C_\infty = 1.393 - 0.015 \cdot \ln(Re)$$

$$Re = \frac{\rho_\ell \cdot j \cdot D}{\mu_\ell}$$

The dispersed flow film boiling region has been subjected to quite intense research efforts, especially in recent years.

Inverted Annular Film Boiling

Figure A5.2 shows three possible types of inverted annular flow. The continuous liquid core is separated from the wall by a low viscosity vapour film which can accomodate steep velocity gradients. The velocity in the liquid core is usually fairly uniform. At low velocities the vapour film is laminar with a rather smooth vapour - liquid interface (Fig. A5.2a). If the velocity is increased the vapour film becomes turbulent and the interface will be wavy and unstable (Fig. A5.2b). If the velocity is further increased liquid droplets will be torn away from the wavy interface thus giving rise to entrainment in the vapour film (Fig. A5.2c).

As long as the wall temperature is greater than the minimum film boiling temperature the heat is transferred from the wall to the vapour film and subsequently from the vapour to the vapour-liquid interface. If the liquid core is subcooled a significant fraction of the heat flux will be used for heating the liquid; if the liquid is saturated the heat transferred from the interface will be used for evaporation thus increasing the vapour velocity. The increased velocity differential across the interface will lead to an increased entrainment in the vapour film and also to a higher turbulence level in the vapour annulus. This will increase the wall-vapour and the vapour-liquid core heat

transfer which in turn will lower the wall temperature. If the wall temperature drops below the minimum film boiling temperature rewetting of the wall may occur.

Different types of correlations have been developed for calculating the heat transfer coefficient in the inverted annular flow region (see (12)). The correlations can be divided into the following categories:

* Correlations applicable to pool boiling conditions and heat transfer at low mass fluxes. A well-known example of these is the Bromley correlation. Most of the correlations of this type have the form

$$
h = a \cdot \left[\frac{k_v^3 \cdot \rho_v \cdot (\rho_\ell - \rho_v) H_{fg}' g}{\mu_v \cdot \Delta T_{SAT}} \right]^{1/4} f(V,\lambda)
$$

The latent heat H_{fg}' is usually modified to include the vapour superheat while the velocity effect is included through the function $f(V,\lambda)$ where λ is equal either to the hydraulic diameter, the critical wavelength, or the most unstable wavelength.

* Correlations of the modified McAdams type. These correlations basically have the form

$$
Nu = a \cdot Re^b \cdot Pr^c \cdot F
$$

where F usually is a function of quality or vapour film temperature.

* Phenomenological correlations based on the different mechanisms governing this type of heat transfer.

The literature search reported in (12) resulted in a recommedation to use a modified Bromley correlation when evaluating the heat transfer for the inverted annular flow. This correlation can be written as

$$
q'' = h \cdot (T_w - T_{SAT})
$$

$$h = 0.62 \cdot \left[\frac{k_v^3 \cdot \rho_v \cdot (\rho_\ell - \rho_v) H_{fg}' \cdot g}{\lambda_c \cdot \mu_v \cdot \Delta T_{SAT}} \right]^{1/4}$$

where

$$\lambda_c = 2\pi \cdot \left[\frac{\sigma}{g(\rho_\ell - \rho_v)} \right]^{1/2}$$

λ_c is the critical wavelength of Taylor instability. This correlation seems to fit the data reasonably well within the parameter range

Pressure	0.1 - 0.7 MPa
Wall Heat Flux	30 - 130 kW/m^2
Subcooling	< 78 K
Velocity	< 0.3 m/s
Void	< 0.4

An interesting study of the low flow film boiling heat transfer coeffiecient of Bromley was carried out by GE, USA (36,37). In a recent study (38) some deficiencies of the modified Bromley models were pointed out. Specifically mentioned were the lack of influence of the distance from the CHF location and the exclusion of flowrate and subcooling effects. In that context a new model was also developed, based on the Bromley type of analysis but including the above mentioned effects. The analysis terminated in a differential equation that was integrated numerically with adequate boundary conditions. The result was compared to some new data from a single tube reflooding experiment and the comparison was quite satisfactory (Fig. A5.3). The result using the modified Bromley model was much less successful, as shown in Fig. A5.4. However one major drawback with this new model is the difficulty of implementing it in the numerical scheme of an already existing computer code like RELAP5 and TRAC due to the differential form of the model.

Breakdown of Inverted Annular Flow

The breakdown of the liquid core into slugs and further down-

stream to droplets has also been related by some authors to a critical Weber number based on the diameter of the liquid core (approximately equal to the channel hydraulic diameter) and the relative velocity between the phases at this point:

$$We_{tr} = \frac{\rho_g \cdot (v_g - v_\ell)^2 \cdot D}{\sigma}$$

According to (12) a We-number of approximately 10 seems to fairly well correlate the data obtained in reflooding experiments. However in (38) We ~ 20 is obtained. This We-number was based on the vapour velocity only, but as the liquid velocity was rather small in that study the result would be only slighty lower if the relative velocity definition was used. Thus when a We-number of 10 to 20 is exceeded the liquid core can be assumed to break down.

Dispersed Droplet Film Boiling Region

In the dispersed droplet flow region the liquid phase exists as droplets of different sizes carried along in the vapour flow. Several investigations have shown that the vapour phase in general is superheated (12) with respect to the local saturation temperature while the liquid phase normally is found to be close to saturated conditions. These nonequilibrium effects have been found to be of major importance when describing the pertinent heat transfer mechanisms and the development of this region.

Due to the difficulty of measuring the vapour superheat when liquid droplets are present, the exact mechanisms for the heat transfer are poorly understood despite the intense research efforts made during the last years. In most of the experiments only the wall temperatures were measured and the nonequilibrium vapour conditions had to be inferred from these temperatures by use of a single-phase convective heat transfer correlation and the assumption that the wall-to-droplet heat transfer was negligible.

However, a leap forward was taken when a technique was developed to measure the vapour temperature by means of a specially designed aspiration thermocouple probe (39,40). In those studies the vapour superheat was measured at only one location downstream of the CHF-front though, so the axial behaviour of the nonequilibrium effect was unknown. Quite recently two experimental test series were conducted (41,42) in which the axial variation of the nonequilibrium conditions downstream of the CHF-front was also measured. From the results of these experiments it was evident that the vapour generation was quite high near the CHF location and decreased further downstream. The increased vapour generation near the CHF location was hypothesized to be caused by some sputtering effects when the wall liquid film was violently driven off the wall at the CHF location (17).

This indicates that the vapour generation has to be separated into a near field region where the vapour generation rate is relatively high, and a far-field region with a lower vapour generation rate. Thus, different mechanisms can be assumed to be dominant in each region.

Prediction Methods
Basically, two main groups of models can be identified when analyzing the approaches utilized for calculating the heat transfer in the dispersed droplet film boiling region (12,43): equilibrium correlations and nonequilibrium models.

Equilibrium Correlations
This approach is based on two assumptions:

*   Thermodynamic equilibrium exists between the two phases

*   Heat transfer at the heated walls occur primarily by turbulent vapour convection.

This can be expressed mathematically as

$$q'' = h_c \cdot (T_w - T_{SAT})$$

The heat transfer coefficient h_c is calculated from an equilibrium correlation, for instance, Groeneveld and Dougall-Rohsenow correlations (12). Also the Condie-Bengston correlation is of this type and is currently utilized in the RELAP5/ MOD1 computer code (44).

When compared with experimental data these types of correlations seem to predict reasonable trends, the quantitative disagreements can be substantial though (43). It is also questionable whether these types of correlations in nonequilibrium computer programmes like, eg. RELAP5, should be utilized (45).

Nonequilibrium Models
The nonequilibrium models recognize the importance of vapour superheating when calculating the heat transfer. The models can be grouped into two categories (12): a) local correlations, b) separate phase models.

a)   Local Correlations

This type of correlation calculates the local vapour superheat and heat transfer coefficient from local thermal hydraulic parameters. Examples are the Groeneveld-Delorme correlations and the CSO correlation of Chen, Sundaram and Ozkaynak. Both of these correlations are given in (12). They relate either the actual quality or the vapour superheat and the wall heat transfer coefficient to such parameters as the vapour Reynolds number and equilibrium quality. They are easy to implement into existing thermohydraulic codes but due to their highly empirical nature the prediction results usually reveal quite substantial scatter although the average result from a large number of calculations can be rather good.

b)   Separate Phases Models

In these models the degree of nonequilibrium at any axial location is dependent on the upstream development of different competitive heat transfer mechanisms. The models can be brought to different levels of sophistication where the highest level includes the full set of conservation equations for each phase. Inherent in this approach is the need to specify the interfacial transport phenomena as well as the partition of the wall heat transfer between the phases.

In the dispersed droplet flow the nonequilibrium effects are basically determined by a balance between the wall to vapour heat transfer and the evaporation of entrained liquid droplets. The wall-to-vapour heat transfer can be evaluated by means of an ordinary single phase heat transfer correlation or more preferably by a specially developed correlation (e.g. the heat transfer equation in the CSO correlation). The evaporation is determined by a volumetric vapour source term giving the rate of vaporization per unit mixture volume. Various models have been proposed for estimating the vapour source function but no final conclusion can be made yet (see A6). One example is the correlation of Webb and Chen (6):

$$\Gamma = 1.32 \left[\frac{P}{P_c}\right]^{-1.1} \left[\frac{G \cdot XA}{\alpha_h}\right]^2 \frac{(1-\alpha_h)^{2/3} \cdot (T_v - T_{SAT}) \cdot k_v}{\rho_v \cdot \sigma \cdot H_{fg} \cdot D}$$

This correlation was implemented in NORAS and RELAP5 computer codes and some-steady state post-dryout experiments were analysed assuming a two-step heat transfer process, e.g. the heat was transferred from the wall to the vapour phase and from the vapour to the liquid droplets (46, 47). As only the wall temperature was measured it could only be concluded that the complete model was fairly accurate in the prediction of the wall surface temperature, but no assessment of the calculated vapour superheat could be given. A comparison of different correlation predictions with measured nonequilibrium conditions revealed that the above equation correctly predicted some of the experimental data, showing a large scatter though (48).

As can be seen from the above equation the vapour generation rate is directly proportional to the local vapour superheat T_V-T_{SAT}. Near the CHF-front where the vapour superheat is very minor a small vapour generation rate will thus be predicted. This is in direct conflict with the new findings that the vapour generation is dependent on the distance from the CFH-front with a high vaporization in the region near the CHF location.

In order to improve the predictions and take these new observations into account a new model for the vapour source term was recently developed (17). In the near-field region of CHF the vapour generation rate was postulated to vary with:

1. Wall superheat T_W-T_{SAT}
   Due to the repulsive evaporative forces on the liquid the vapour generation rate is expected to decrease when the wall superheat increases.

2. Distance from the CHF-front L/D
   The near-field vapour generation rate should decrease when the distance increases.

3. Liquid mass $G \cdot (1-XA)$
   The vapour generation rate should be directly proportional to the liquid mass flux.

The near-field vapour generation was then suggested to be

$$\Gamma_{NF} = \frac{4 \cdot q''}{D \cdot H_{fg}} \cdot \exp\left[-C \, \frac{T_W-T_{SAT}) \cdot L/D}{G \cdot (1-XA)}\right]$$

where the empirical constant was found to be independent of pressure having the value

$$C = 0.0016 \ kg/(m^2 \ s \ K)$$

In the far-field region, the vapour generation rate was determined by a revised form of the Webb and Chen correlation (6):

$$\Gamma_{FF} = 2.0 \cdot 10^3 \cdot j_v^2 \cdot \frac{(1-\alpha_h)^{2/3} \cdot (T_v - T_{SAT})}{H_{fg} \cdot D}$$

The total vapour generation rate was then simply the sum of the near-field and the far-field contributions:

$$\Gamma = \Gamma_{NF} + \Gamma_{FF}$$

This model was compared to experimental data obtained at Lehigh University (41) and at INEL (42). The model was able to predict the experimental values for both sets of data with reasonable agreement.

The parameter range of the model is

Pressure	0.2 - 7.0 MPa
Mass Flux	12 - 100 kg/m^2 s
CHF Quality	0.0 - 0.99
Wall Heat Flux	8 - 225 kW/m^2

The above given model for vapour generation rate was also used along with a new heat transfer correlation to predict the vapour superheat (17). The heat transfer correlation was a revised version of the modified CSO correlation and can be written as

$$h = h_{mod\ CSO} \,(1+F_s)(1+0.8/(L/D))$$

$$F_s = 250 \left(\frac{P}{P_c}\right)^{0.69} \left(\frac{1-XA}{XA}\right)^{0.49} Re_v^{-0.55}$$

$$h_{mod\ CSO} = \frac{f}{2} \cdot C_{pv\ell} \cdot G \cdot XA \cdot Pr_{v\ell}^{-2/3}$$
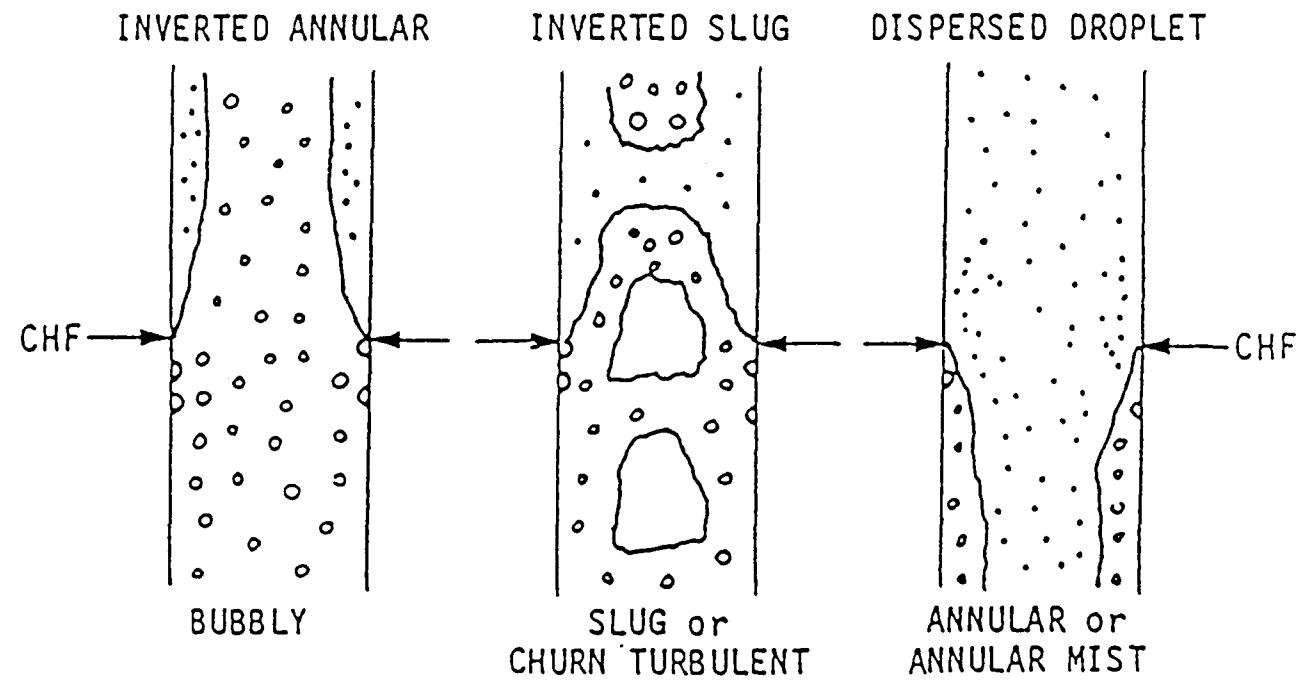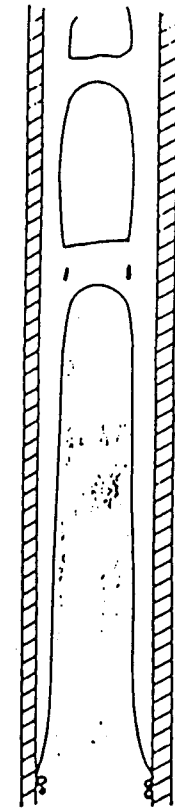
FIGURE A5.1 FLOW REGIONS, TRANSITIONS, AT CHF
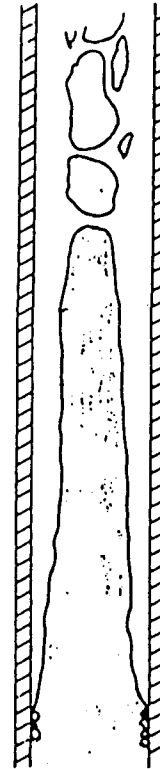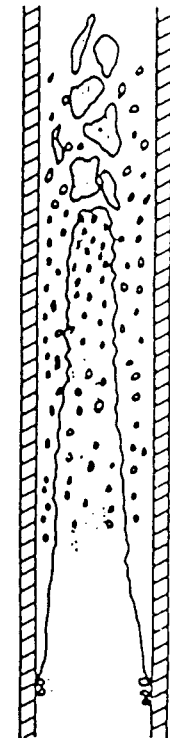
a) LAMINAR FLOW

b) TURBULENT FLOW
WITHOUT ENTRAINMENT

c) TURBULENT FLOW
WITH ENTRAINMENT

← INCREASING MASS FLUX

FIGURE A5.2
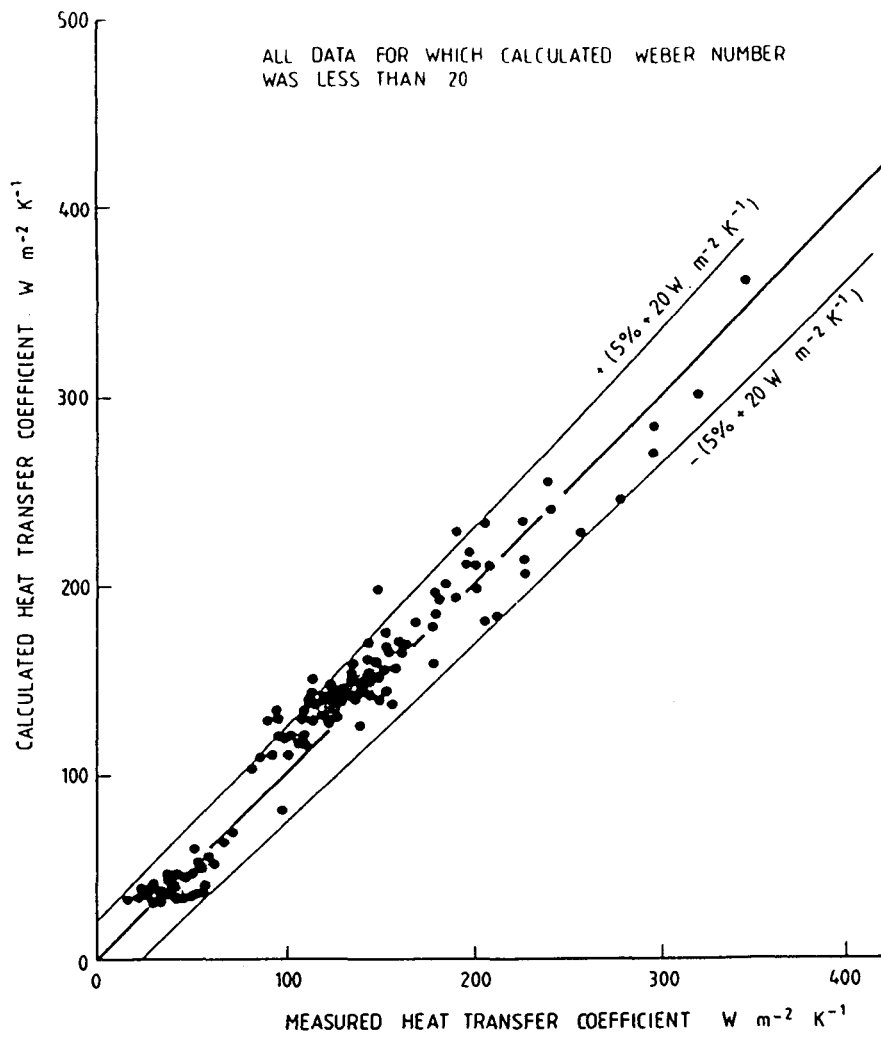TYPES OF INVERTED ANNULAR FILM BOILING

FIGURE A5.3
COMPARISON OF MEASURED AND CALCULATED HEAT TRANSFER
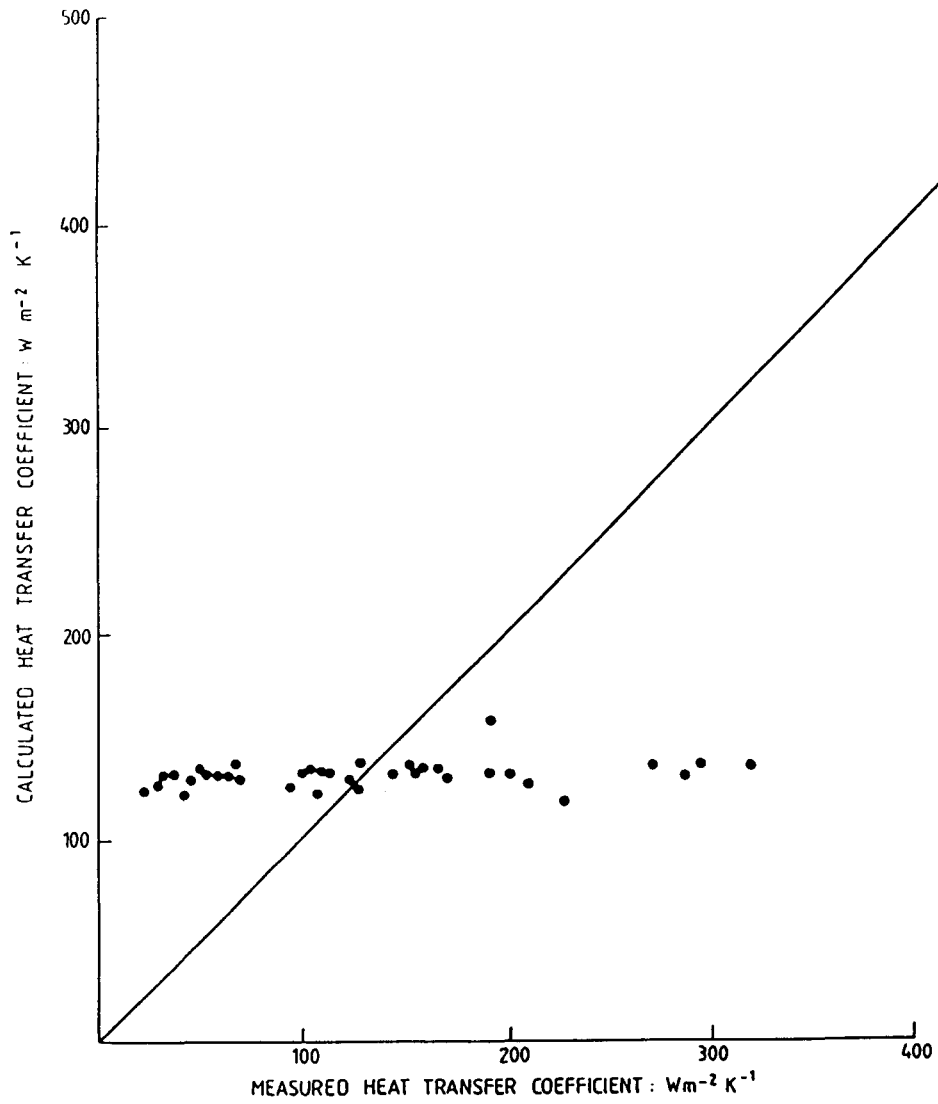COEFFICIENTS - PRESENT WORK (FROM REF. 38)

FIGURE A5.4

COMPARISON OF MEASURED HEAT TRANSFER COEFFICIENTS
WITH "MODIFIED BROMLEY" MODEL (FROM REF. 38)

$$f = f_o \cdot \left(\frac{T_w}{T_v}\right)^{-0.1}$$

$$\frac{1}{\sqrt{f_o}} = 3.48 - 4 \cdot \log_{10}\left[\frac{2\varepsilon}{D} + \frac{9.35}{Re_v \sqrt{f_o}}\right]$$

The predicted vapour superheat from this film boiling model was compared with nonequilibrium experimental data. There was still some scatter but the model was an improvement compared to earlier models.

A6. Interfacial Heat Transfer

When a two-fluid model is used, interfacial mass-transfer rate Γ is calculated from

$$\Gamma = -\frac{Q_{i\ell} + Q_{ig}}{H_{fg}}$$

where $Q_{i\ell}$ is the heat transferred from the interface to the liquid phase, Q_{ig} is the heat transferred from the interface to the vapour phase and H_{fg} is latent heat of evaporation. The interfacial heat transfer rates are calculated from

$$Q_{ik} = h_{ik} \cdot (T_k - T_{SAT})$$

where T is the temperature, h_{ik} is the volumetric heat transfer coefficient, and the subscript k is either ℓ or v. Some correlations are expressed in terms of enthalphy or quality. From a computational point of view the use of enthalphy instead of temperature is more convenient, because usually enthalphy (or enthalpies) is one of the dependent variables to be evaluated. All the correlations can be transformed to a suitable form, for example

$$Q_{ik} = \frac{h_{ik}}{c_{pk}} (H_k - H_{kSAT})$$

where c_{pk} is specific heat.

Often the correlations are expressed in a form giving the mass transfer rate Γ. From a computional point of view it is however, convenient to have correlations for h_{ig} and $h_{i\ell}$ and to calculate Q_{ig} and $Q_{i\ell}$. Then Γ can be calculated from the first equation. If the original correlation is for the mass transfer rate, it can be transformed to a more suitable form by taking into account the fact that usually either

$$Q_{i\ell} \quad \gg \quad Q_{ig}$$

or

$$Q_{ig} \gg Q_{i\ell}$$

The first condition is valid when the mass fraction of liquid is larger than the mass fraction of vapour and the second condition holds in the opposite case. The conditions imply also that usually only one correlation for either h_{ig} or for $h_{i\ell}$ is needed. The other coefficient can be replaced with a sufficiently large value, which keeps the least massive phase near the saturated state.

There are four different interfacial heat transfer regions where either h_{ig} or $h_{i\ell}$ must be specified. These are summarized in the following:

1. $T_l > T_{\ell SAT}$ i.e. liquid is superheated. In this case liquid evaporates to vapour (flashing phenomemon).

2. $T_l < T_{\ell SAT}$. Vapour is condensed by the subcooled liquid

3. $T_g > T_{gSAT}$. Liquid is evaporated by the superheated vapour

4. $T_g < T_{gSAT}$. Subcooled vapour is condensed to liquid.

The first regions may occur in liquid-continuous flow and the two last regions in vapour-continuous flow. In vapour-continuous flow the different temperature conditions in the liquid phase do not lead to evaporation or condensation as

described in items 1 and 2, because the flashing rate is controlled by Q_{ig}. The same concerns the vapour phase in the low quality region. Four different correlations for interfacial heat transfer are therefore needed, two for $h_{i\ell}$ and two for h_{ig}. Furthermore, the correlations used for evaporation or condensation must be continuous at the point $T_k = T_{kSAT}$, because discontinuity may trigger an instability, where mass transfer rate and pressure are oscillating.

In addition to the flow boiling, a wall boiling (or condensation) model must be specified. In that case the total mass transfer rate Γ_{tot} is

$$\Gamma_{tot} = \Gamma + \Gamma_g$$

where Γ is calculated from the first equation and the mass transfer rate at the wall Γ_w is calculated using a separate model. This kind of model is needed for suncooled boiling, because in that case no evaporation is predicted using the two first equations. Another case is condensatipon of vapour at the cold wall. In these cases both Γ_w and Γ must be tailored so that the total mass transfer rate is correct.

Although the interfacial heat transfer is of great inportance in all two-phase flow calculations, very few empirical correlations exist at present. Very often the lack of a correlation must be compensated for by using a suitable large value for the interfacial heat transfer coefficient. This approach has also been used in the large system programmes like RELAP5 (see for example Appendix B3). Furthermore, in many cases the correlation developed are "semi-empirical", which means that a correlation is based on an analytical approach and it is tuned using some experimental data. Very often this tuning is based on a limited number of tests and consequently the correlation is not a reliable one for general purposes.

In SÄK-5 work interfacial heat transfer correlations have been tested for flashing and for post-dryout heat transfer (50, 46). In the case of flashing the correlations were tested by

calculating blowdown-experiments where the pressure undershoot below the saturated value is significant (51, 52), and by calculating critical flow experiments (52, 53). Five different correlations were tested and only the correlation of Bauer et al. was satisfactory. This correlation is a simple relaxation type model

$$\frac{\Gamma}{\rho} = \frac{XE - XA}{\tau}$$

where XA is the actual quality, XE is equilibrium quality, ρ is density and τ is time constant. In the case of flashing the condition $Q_{i\ell} \gg Q_{ig}$ holds and the following heat transfer coefficient is obtained

$$h_{i\ell} = \frac{(1-\alpha) \cdot \rho_\ell \cdot C_{p\ell}}{\tau}$$

the time constant τ has been correlated using Moby Dick test as

$$\tau = \frac{660}{(\alpha + \alpha_0)(u + u_0)^2 \sqrt{P}}$$

where α is void fraction, u is velocity in m/s and P is pressure in N/m^2. In the original model $\alpha_0 = u_0 = 0$, but in that case the above equation for τ cannot be used for initial flashing. The correlation is valid in the range of $0.01 < \alpha < 0.96$ and 5 m/s $< u <$ 54 m/s. In the present work the correlation has been extrapolated to cover also the early flashing process. For that purpose the constants were determined to be

$\alpha_0 = 0.003$

$u_0 = 4$ m/s

These values are so small that they do not significantly change the correlation within its validity range, but they predict reasonable values for $h_{i\ell}$ when $\alpha = 0$ or $u = 0$. An alternative for this approach is presented in (54), where the time constant is the minimum of τ calculated from the above equation and the following

$$\tau = \frac{2.7 \cdot 10^{-5} H_{fg}^2}{(H_\ell - H_{\ell SAT})^2}$$

This approach has not been tested in the present work. When the first approach is used to predict the pressure recovery during the blowdown, the result seems to depend on the flow area. When medium-size pipes (D ~ 0.5 m) are simulated the calculated result is close to the experimental one (see Fig. A6.1). When the diameter is smaller, as in Edwards' pipe test, the predicted pressure recovery is too slow. In the case of a large vessel the predicted pressure recovery is too fast (50). This kind of deviation from the experimental data is not so harmful because the error is significant during only a very short period. Furthermore, it is difficult to obtain better results, because the initial flashing is a complicated phenomenon depending on soluble gases, surface roughness etc. It is obvious that in many cases the flashing correlation must be tuned in order to take into account these effects properly.

Better results were obtained from critical flow calculations. When the pipe length was 0.14 m and the diameter 0.014 m, the calculated results were close to the experimental ones on pressure range from 0.3 MPa to 9 MPa (Fig. A6 2). When the pressure was fixed, the correlation was able to predict the increase in mass flux when the pipe length was decreased (Fig. A6.3).

Because at present it seems that there are no better correlations for flashing, Bauer's correlation is recommended. In the test cases calculated it gave moderately good results.
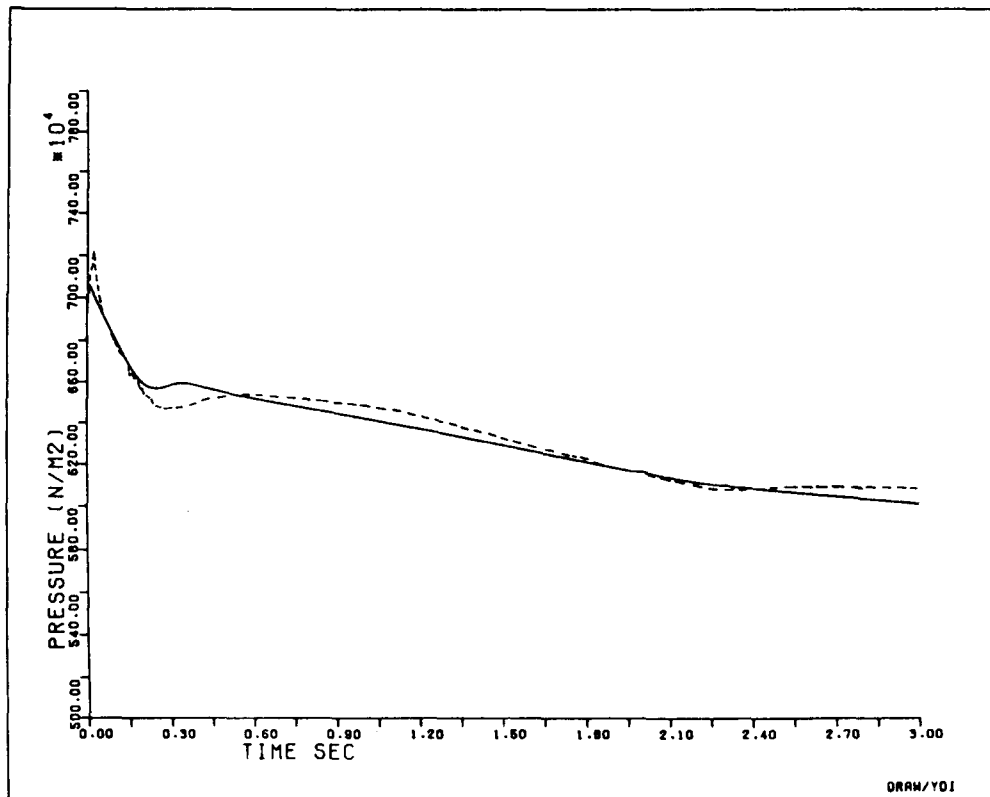
Fig.A6.1 OECD Standard Problem No. 6. Measured (-----) and
calculated (———) pressures at the exit node. The
correlation of Bauer et al. is used for interfacial
heat transfer.

Fig.A6.2 Critical mass flux of saturated water as a function
of pressure. Pipe diameter is 0.014 m and length is
o.14 m. A factor Cl is used to see the sensitivity
of critical flow rate on flashing.

Fig.A6.3 Critical mass flux of saturated water as a function
of pipe length. Pipe diameter is 0.014 m.

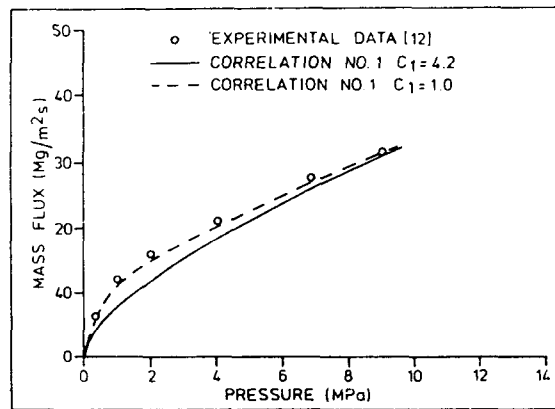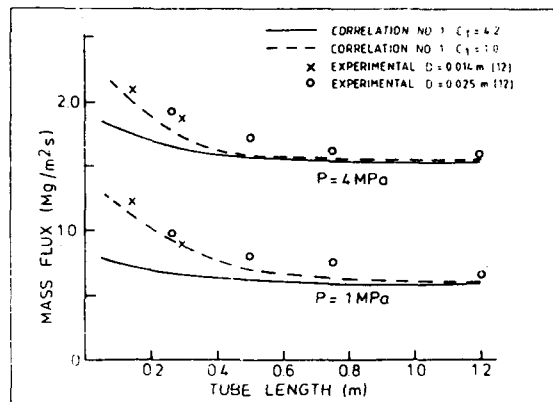APPENDIX B COMPARISON WITH DATA

B1 Heat Transfer Package.

B1.1 RELAP-5

The heat transfer package of RELAP5/MOD1 was originally developed for the RELAP4-programme. In RELAP4 thermal equilibrium between the phases was assumed. RELAP5/MOD1 is a nonequilibrium programme, which utilizes only one energy equation for the thermal energy mixture . It is therefore possible to use the same heat transfer package as in RELAP4. However, certain modifications have to be made, because several heat transfer correlations are based on variables used in equilibrium calculations. When the calculation is based on a nonequilibrium assumption these variables must be calculated using the dependent variables of the nonequilibrium programme. An example is the equilibrium flow quality used in several critical heat flux correlations. The equilibrium quality is not directly solved in computer programmes, that allow thermal nonequilibrium.

The RELAP5/MOD1 heat transfer package (HTRC1) consists of a forced convection (flow related) group of correlation adopted from RELAP4/MOD6 and a pool boiling/natural convection (independent of flow) group of correlations. The low flow region is defined for mass fluxes lower than 200 kg/m^{2}s.

The heat transfer selection logic is based on wall temperature, saturation temperature, equilibrium quality and void fraction. The single-phase heat transfer to liquid is selected if equilibrium quality is lower than zero and wall temperature is lower than saturation temperature. The single-phase heat transfer to vapour is selected if wall temperature exceeds saturation temperature and void fraction exceeds 0.999. The condensation heat

transfer is selected if wall temperature is lowere than saturation temperature and the two-phase mixture temperature is greater than the wall temperature. The nucleate boiling heat transfer is selected if equilibrium quality is lower than the critical and wall superheat is lower than the critical wall superheat as calculated from the critical heat flux correlation. In other cases the post CHF heat transfer correlations are used. The film boiling correlations are changed to the transition boiling correlation if the wall temperature is lower than the minimum film boiling temperature,

During the SÄK-5 project the heat transfer package of RELAP5/ MOD1 has been modified in order to use it independently. This modification follows the original as closely as possible, but is altered slightly for a two-fluid (six-equation) mode. For this purpose the heat transfer coefficient has been shared between liquid and vapour phases. In general, the separated heat transfer part has worked well in the test calculations. Some remarks should be made, however, especially concerning the original RELAP5-programme. In RELAP5 the heat transfer is calculated directly as heat flux. The heat transfer coefficient is interpreted as the derivative of heat flux with respect to wall temperature and is used for the implicit integration of wall temperatures. According to the RELAP5 manual, the heat transfer coefficient of transition boiling should be negative. The programme, however, omits the negative values, perhaps for reasons of stability.

Another remark concerns the definition of quality in the heat transfer part. Although the static equilibrium quality may be more reasonable from a calculational point of view, most of the correlations have been developed using flow quality. In vertical channels, the vapour velocity close to the crisis point may be larger than the liquid velocity, and consequently the flow quality is larger than the static quality. Therefore, the original correlation that uses flow quality, predicts smaller critical heat flux than the same correlation in the RELAP5 package.

There are other problems that appear when heat transfer coefficient surfaces are plotted (Figs. B1.1 and B1.2). The crest of the two-dimensional surfaces in the figures correspond to CHF conditions. Above a cutoff void fraction (0.96) post-CHF heat transfer is automatically assumed. If calculations are made above the cutoff value and the wall temperature is close to the saturation line, the heat transfer coefficient may change discontinously from turbulent film condensation to film boiling (see Figures B1.1 and B1.2). The abrupt change may be avoided by removing the void limit, thus activating the transition boiling mode in RELAP5. This modification has been added to the separate RELAP5 package, when others than the default CHF correlations of RELAP5 are used (Figure B1.2).

Another discontinuity appears when there is change from turbulent film condensation to convection from subcooled water to the wall. In fact, the subroutine of RELAP5 that calculates condensation deviates from the description of the manual. In the same subroutine there is also a discontinuous change in laminar film condensation, when a horizontal part is slightly inclined.

The problems concerning the vapour quality and the discontinuities are not important in blowdown analyses. They may be the reasons for unstable oscillations, when the heat transfer package is applied to milder transient or steady-state calculations. It is probably impossible to remove all troubles from such a large package, because there are too many input variables involved for heat transfer correlations. Before starting a new case the graphical study of the heat coefficient surface could therefore be useful in order to avoid instability problems.

B1.2 TRAC (PF1)

The wall-to-fluid heat transfer selection and calculation is concentrated to one major subroutine HTCOR. Some of the heat transfer coefficients and critical heat flux are calculated in subroutines called from HTCOR.
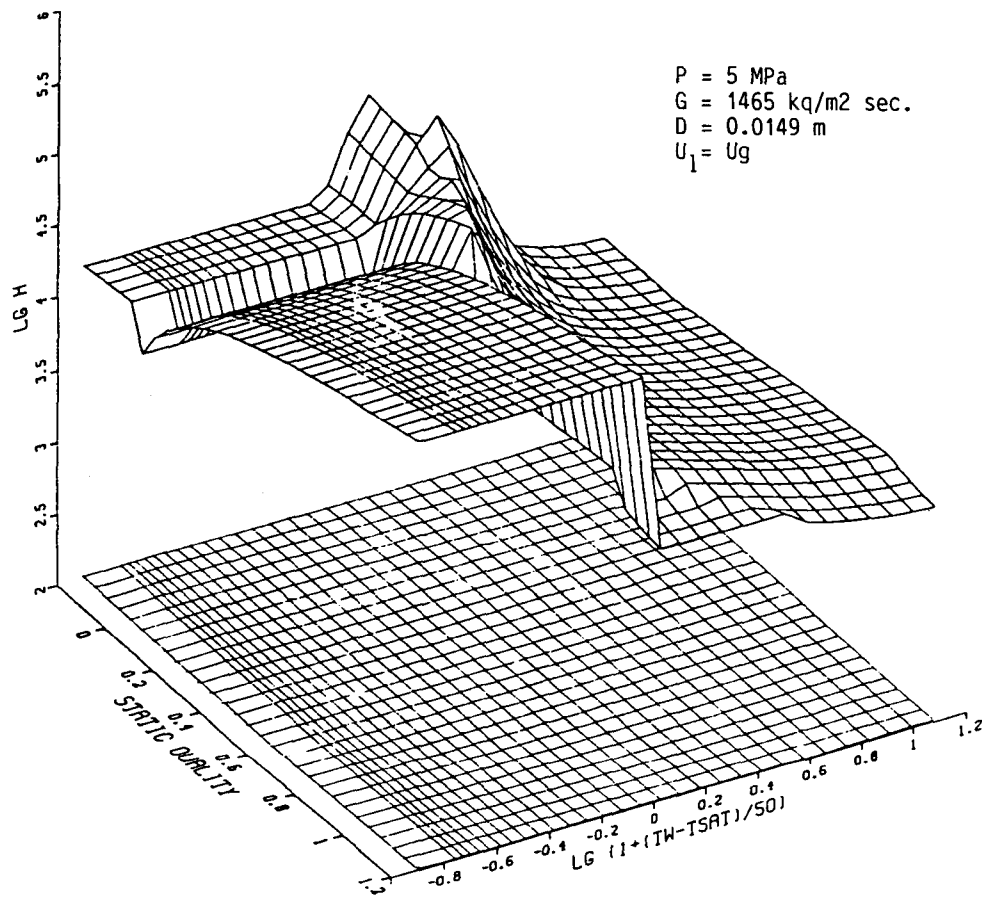
FIG. B1.1 HEAT TRANSFER COEFFICIENT SURFACE USING THE HEAT TRANSFER
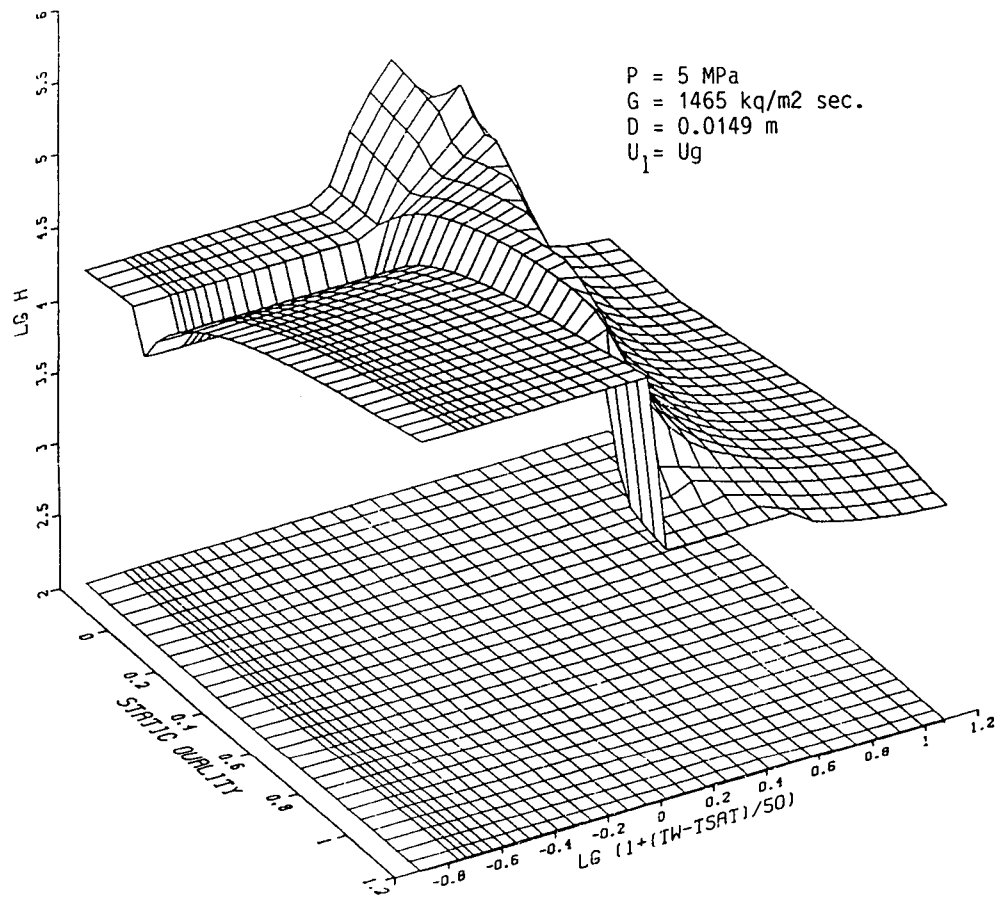PACKAGE OF RELAP 5 WITH DEFAULT CHF-CORRELATION.

FIG. B1.2 HEAT TRANSFER COEFFICIENT SURFACE USING THE HEAT TRANSFER
PACKAGE OF RELAP 5 WITH BECKERS CHF-CORRELATION AND THE VOID
LIMIT EXCLUDED'

The programming in HTCOR is rather straightforward and the exchanging of correlations should not be too difficult. To do it, however, requires a good understanding of the selection and interpolation logic. The exchanging of correlations has not been tried but the fixing of the locus of CHF has been used and was easily made.

The selection is based on the calculated wall temperature, critical temperature, minimum film boiling temperature, bulk temperature, void fraction (vapour quality) and the boiling curve.

Eight modes of heat transfer are considered:

1. Forced convection to single-phase liquid.
2. Nucleate boiling.
3. Transition boiling.
4. Film boiling.
5. Convection to single-phase vapour.
6. Convection to two-phase mixture.
7. Condensation.
8. Liquid natural convection.

The selection of the first five modes are directly attached to the boiling curve.

The modes 6, 7, and 8 are separate modes of heat transfer.

The selection of mode 6, convection to two-phase mixture, is the result of an input option in TRAC. CHF can not occur in this case. The liquid heat transfer coefficient is determined as the maximum of the laminar and the turbulent flow values:

$$h_\ell = \text{max.} \ (h_{\ell, \text{ lam.}}, \ h_{\ell \cdot \text{turb}})$$

$$h_{\ell, \text{ lam}} = 4k_\ell/D \qquad \text{(McAdams)}$$

and Dittus-Boelter for turbulent flow:

$$h_{\ell,turb} = k_\ell/D \cdot 0.023 \cdot (Re_m)^{0.8} \cdot (Pr)^{0.4}$$

$$Re_m = G \cdot D/\mu_m$$

A two-phase viscosity based on actual quality is calculated and used in the calculation of the Reynold's number:

$$\mu_m = 1/(\frac{XA}{\mu_g} + \frac{(1-XA)}{\mu_\ell})$$

If the void fraction is less than a cutoff value, h_l is chosen as the heat transfer coefficient.

If the void is greater than the cutoff value, the vapour heat transfer coefficient is determined as the maximum of the Dittus-Boelter value for vapour and the turbulent natural convection value:

$$h_g = max. \ (h_{vnc}, \ h_{vturb})$$

where

$$h_{vnc} = 0.13 \cdot k_g/D \cdot (Gr \cdot Pr)^{1/3}$$

The mixture heat transfer coefficient is determined from linear interpolation between these values of h_ℓ and h_g and the single-phase values.

Mode 7 is the condensation mode. Condensation heat transfer has not been considered in this project. TRAC uses the Chen-correlation for nucleate boiling (Table A1.I) with the suppression factor S set equal to zero. If the equilibrium vapour quality XE is greater than 0.71, the limit of Chen's data base, then the correlation is evaluated at XE=0.71. Condensation is selected if $T_W < T_\ell$, $T_W < T_{SAT}$ and $\alpha > 0.05$.

Mode 8 is the liquid natural convection mode and is selected if:

$$Gr/Re^2 > 1.0$$

The Grashofs number is defined as:

$$Gr = \frac{\rho_\ell^2 \cdot \beta \cdot g \cdot \Delta T \cdot L_C^3}{\mu_\ell^2} = \frac{\rho_\ell \cdot \beta \cdot g \cdot \Delta T \cdot L_C}{\rho_\ell^2 \cdot u^2} \cdot \left(\frac{\rho_\ell \cdot u \cdot L_C}{\mu_\ell}\right)^2$$

i.e. product of the Reynold number squared and a factor that is the ratio between the buoyancy and the velocity head. This ratio is greater than 1.0 when the buoyancy will prevail and natural convection exists.

The natural convection heat transfer coefficient is then determined from

$$Nu = C \cdot (Gr \cdot Pr)^n$$

where

$C = 0.59$ and $n = 0.25$ in laminar flow ($10^4 < (Gr. Pr) < 10^9$)

and $C = 0.13$ and $n = 0.3333$ in turbulent flow ($10^9 < (Gr. Pr) < 10^{12}$)

The other modes follow the boiling curve.

The single phase liquid heat transfer coefficient is calculated using McAdams correlation (see above) for laminar flow and Dittus-Boelter for turbulent flow, unless natural convection prevails.

Chen's correlation (Table A1.I) is used both in the nucleate and forced convective boiling region.

The Bjornard and Griffith's empirical correlation (Table A3. I) is used in the transition boiling region. The transition boiling is calculated when the surface temperature is above CHF temperature and below the minimum film-boiling temperature i.e. $T_{CHF} < T_w < T_{MFB}$. T_{CHF} is determined from the Biasi CHF correlation. The minimum film-boiling heat-flux correlation has not been studied in this project.

In the film-boiling region thermal radiation and dispersed flow heat transfer occur between the surface and the liquid.

The dispersed flow heat transfer coefficient is calculated using The Forslund and Rohsenow correlation:

$$h_{df} = 0.2552 \cdot ((1-\alpha) \cdot E)^{0.6667} \cdot \left(\frac{k_\ell}{D}\right) \cdot \left(\frac{\rho_\ell \cdot \rho_g \cdot g \cdot H'_{fg}D^3}{(T_w-T_{SAT}) \cdot \mu_g \cdot d \cdot k_\ell}\right)^{0.25}$$

where E is the entrained liquid fraction.

The vapour heat transfer coefficient is the maximum of the Bromley (Table A3. I, h_{FB} in No. 3), natural convection and Dougall and Rohsenow's modification to Dittus-Boelter

$$h_g = 0.223 \cdot \frac{k_g}{D} \cdot [Re_g \cdot (XE + \frac{\rho_g}{\rho_\ell}(1-XE))]^{0.8} \cdot Pr_g^{0.4}$$

In the single phase vapour region the maximum of turbulent natural convection and Dittus-Boelter are used. The selection is determined by XE>1.0, $T_w>T_\ell$ and $T_w>T_{SAT}$.

The interfacial heat transfer correlations are mixed within the programming and it may not be a simple task to change the correlations used.

B1. 3 NORA

The wall-to-fluid heat transfer selection and calculation is concentrated upon one major subroutine, WALLS. The critical heat flux is calculated by calling CHFCOR. The programming in WALLS is straightforward and the exchange of correlations is simple.

The logic for selecting the heat transfer mode is not complicated. First, a set of limiting values on void fraction and quality are calculated in subroutine LIMIT. If equilibrium quality is above a certain value, ALIM(1), a dry wall is always assumed. The heat transfer mode is the forced convection to steam or surface condensation, depending on wall surface temperature.

In all situations heat transfer coefficients based on convection to liquid and boiling are first calculated and a heat transfer mode is chosen such that it gives the highest heat flux. This heat flux is next compared with the critical heat flux. If the heat flux is less than CHF the calculation stops.

If the heat flux is greater than CHF, the minimum film boiling temperature, T_{MFB}, and the heat flux at this temperature are calculated. If the wall temperature is less than T_{MFB} an interpolation is made between heat the fluxes at CHF and T_{MFB} (transition boiling). If the wall temperature is larger than T_{MFB} film boiling or single-phase vapour heat transfer is chosen. The selection logic chooses the highest heat transfer coefficient calculated for the region.

The interface heat transfer calculation is done in two subroutines, FLASH and HPHASE. FLASH calculates the energy transfer due to mass transfer and HPHASE calculates heat transfer that is not directly related to mass transfer.

B2. Comparison with Data.

The different experiments utilized as test cases are summarized in Table 4.2.I. As can be seen from the table the experiments can be divided into four groups assigned as the Roumy experiments, the CE/EPRI experiment, the Becker experiments, and the ORNL experiments. A brief description of each group of experiments will be given in what follows together with some results from the calculations with the computer codes RELAP5/MOD1, TRAC(PF1) and NORA.

The Roumy Experiments

The Roumy experiments (56) utilized a vertical tubular test
section with 0.010 m inside diameter. The heated length was
1.0 m and the initial conditions were to some extent comparable
to those in a PWR core (see Table 4.2.I). Two experiments were
selected from the experimental series, one with only a flow
transient and the other with a flow transient combined with a
power transient. All the remaining operating parameters were
kept unchanged. In both cases the inlet mass flow and the exit
wall surface temperature of the test section were measured. These
parameters are plotted in Figs. B2.1 and B2.2. The wall tempera-
ture plots indicate that the exit in both of the cases experienced
a departure from nucleate boiling (DNB) when the flow was de-
creasing (ascending temperature) with a following return to
nucleate boiling (RNB) when the flow was increasing (descending
temperature). Thus these cases could be used to test the capabi-
lities of the computer programme to deal with transient low-
quality CHF, inverted annular flow heat transfer and rewetting
of a hot surface.

The two cases were calculated with RELAP5/MOD1, TRAC(PF1) and
NORA. The boundary conditions were the outlet pressure, the in-
let water properties, the inlet water flow, and power in the tube
wall. Figures B2.3 to B2.8 exemplify typical RELAP5/MOD1 results
with 20 axial nodes of equal length. As can be seen from the
temperature plots (Figs. B2.5 and B2.8) no CHF was experienced,
although the CHF-ratio was about unity (Figs. B2.4 and B2.7).
The CHF-correlations used in RELAP5 in these calculations were
the W-3 correlation (4) in the high-flow region (mass flux G
>1356 kg/m^2 s) and modified Zuber correlation (58) in the low-
flow region (G<271 kg/m^2 s). For intermediate flows the maximum
CHF-value of W-3 correlation and modified Zuber correlation was
used. This selection logic was the reason for the somewhat odd
behaviour of the CHF-curve in Fig. B2.4 between 0.65 and 1.12
s. At 0.65 s a switch was made from the W-3 correlation to
modified Zuber correlation because at that time the latter corre-
lation began providing the largest CHF-value (G was between 271
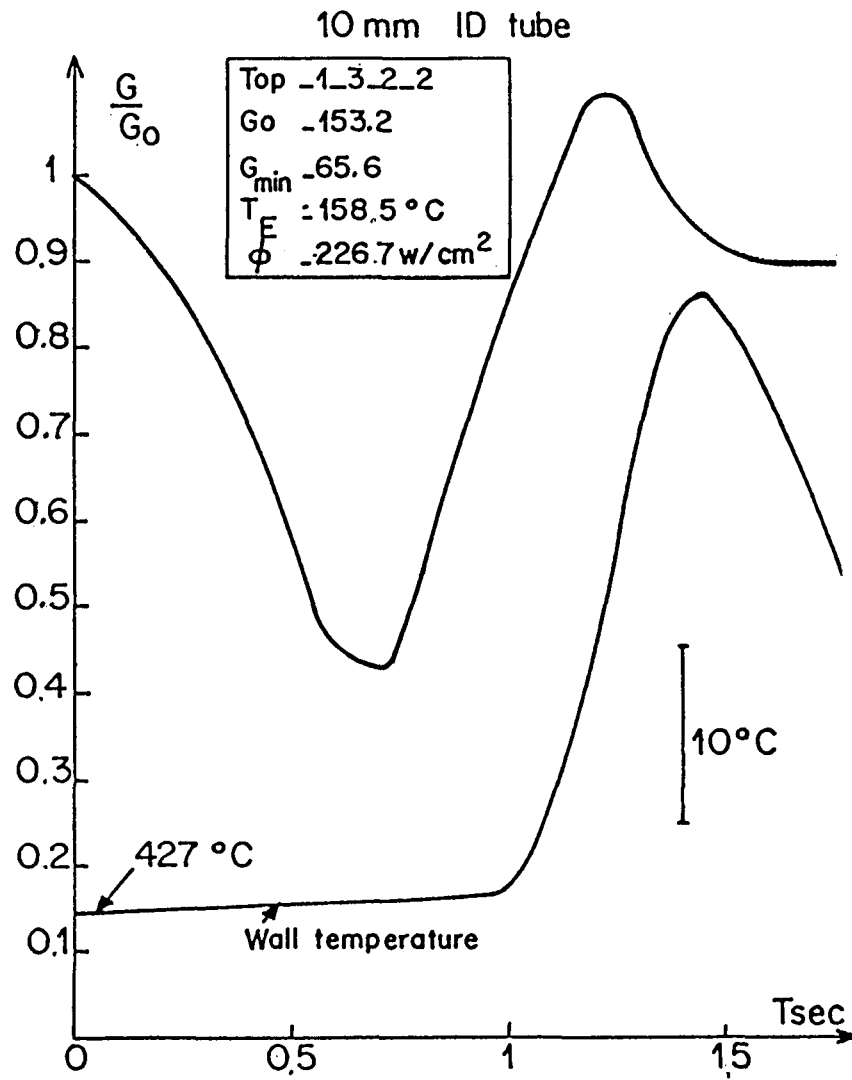and 1365 kg/m^2 s). At 1.12 s a switch back to the W-3 correlation

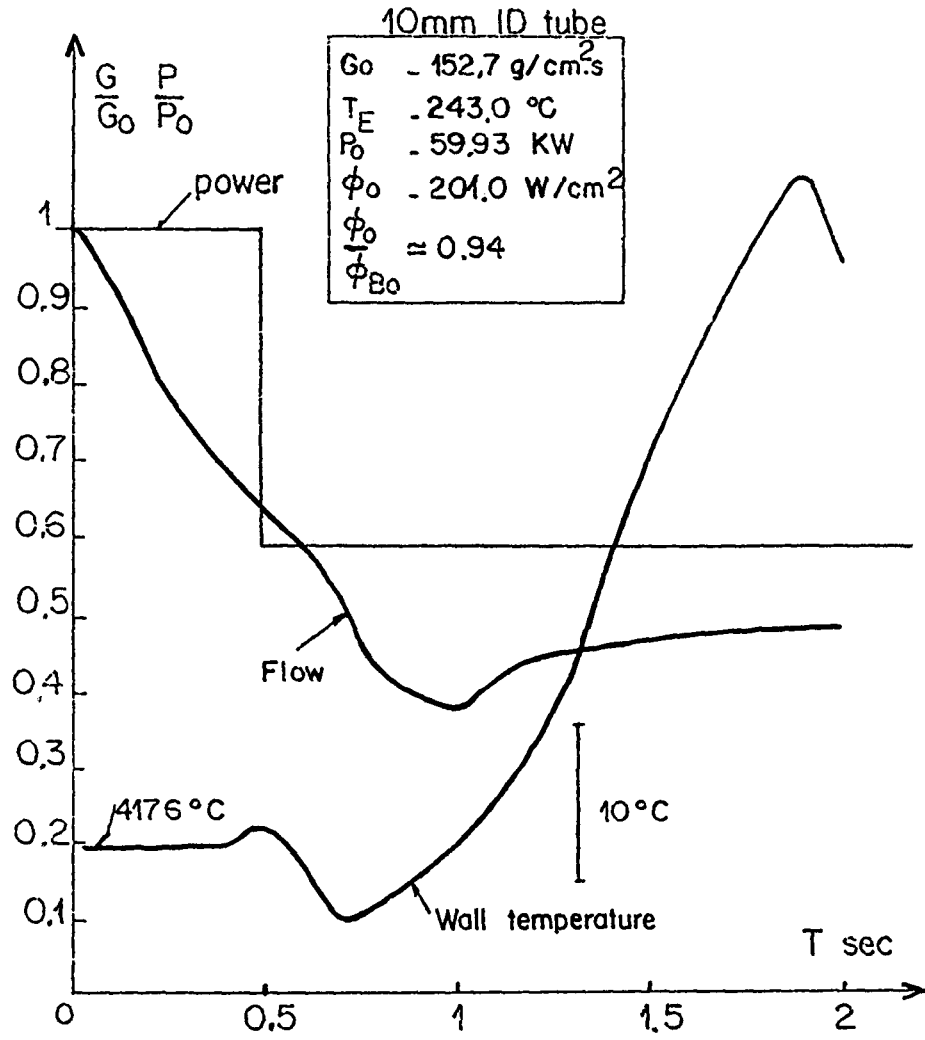FIG. B2.1   ROUMY CASE 1. FLOW TRANSIENT (FROM REF. 56)

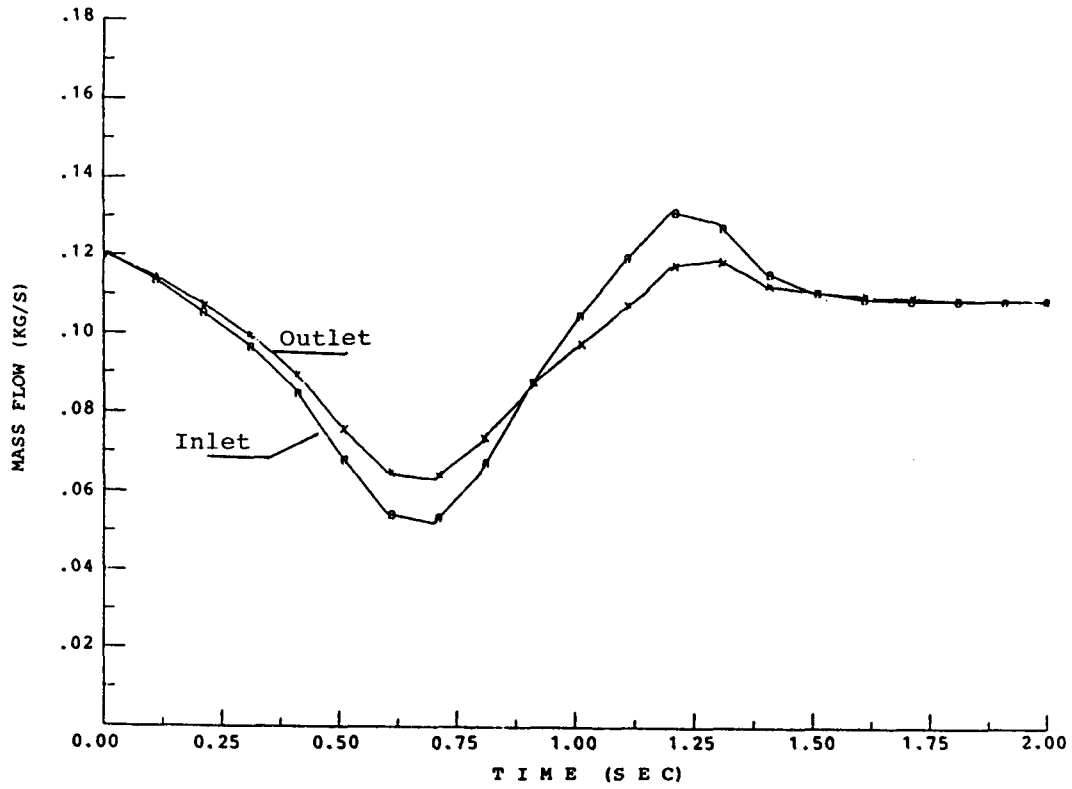FIG. B2.2   ROUMY CASE 2. FLOW AND POWER TRANSIENT (FROM REF. 56)

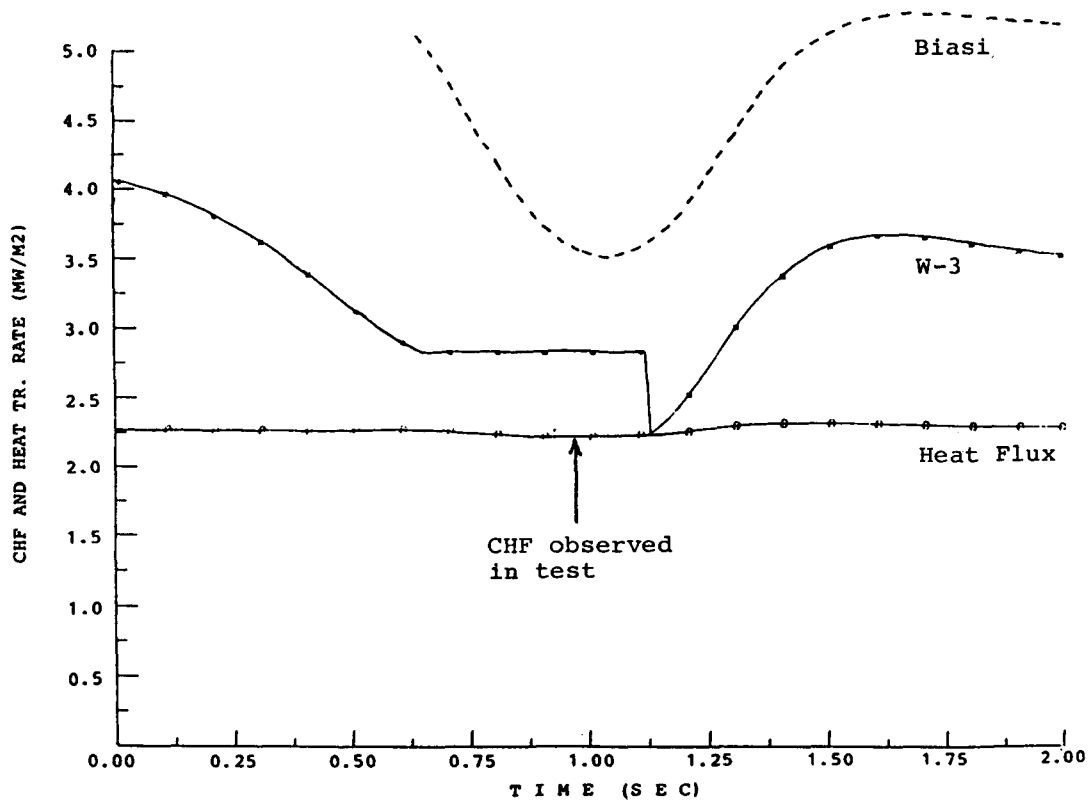Fig. B2.3   RELAP5/MOD1/018   Roumy Case 1

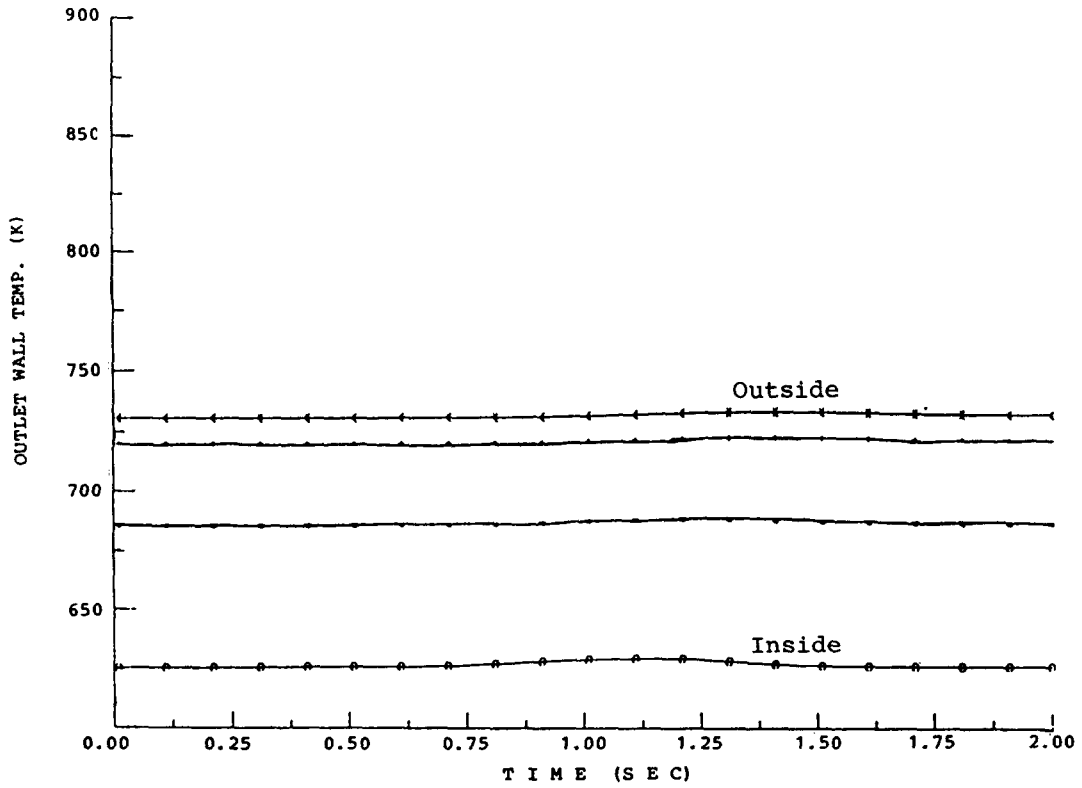Fig. B2.4   RELAP5/MOD1/018   Roumy Case 1

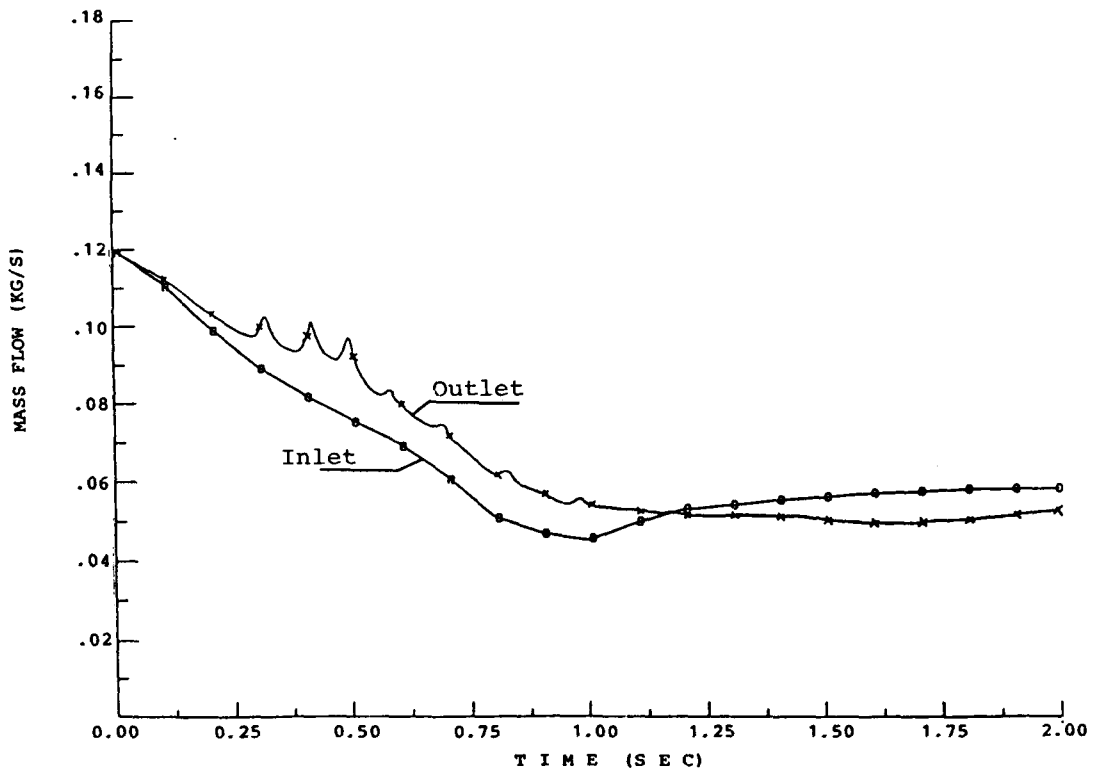Fig. B2.5   RELAP5/MOD1/018   Roumy Case 1
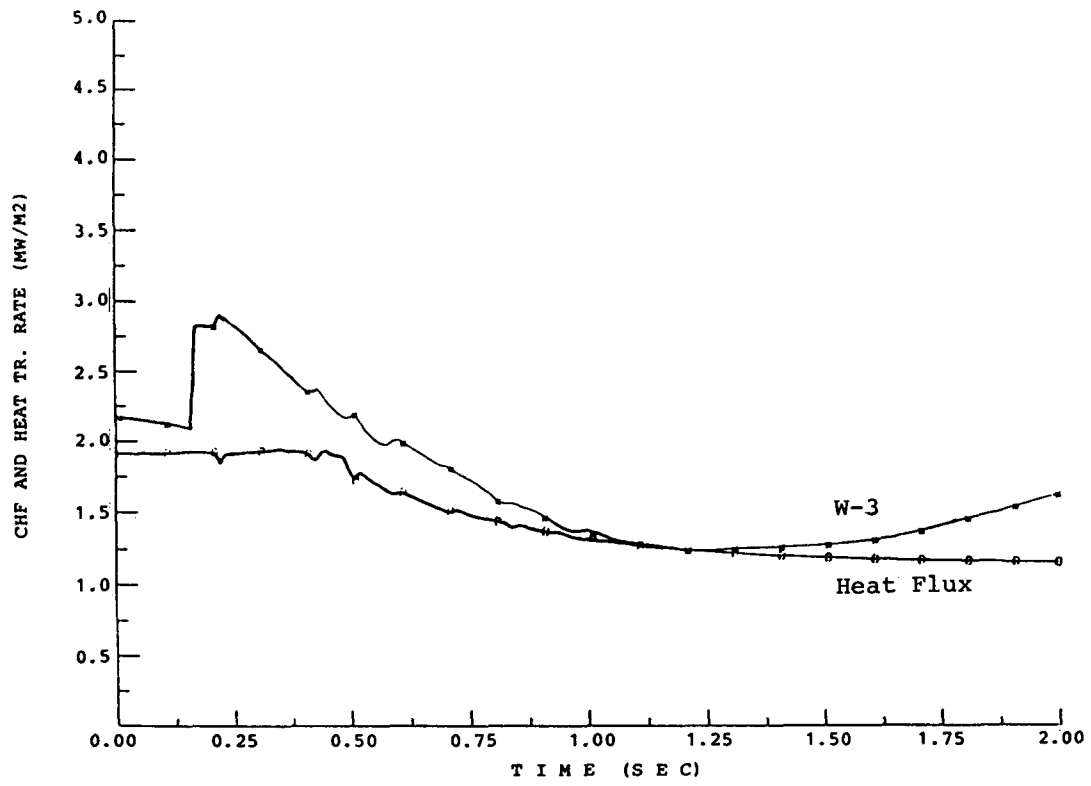

Fig. B2.6   RELAP5/MOD1/018   Roumy Case 2

Fig. B2.7   RELAP5/MOD1/018   Roumy Case 2
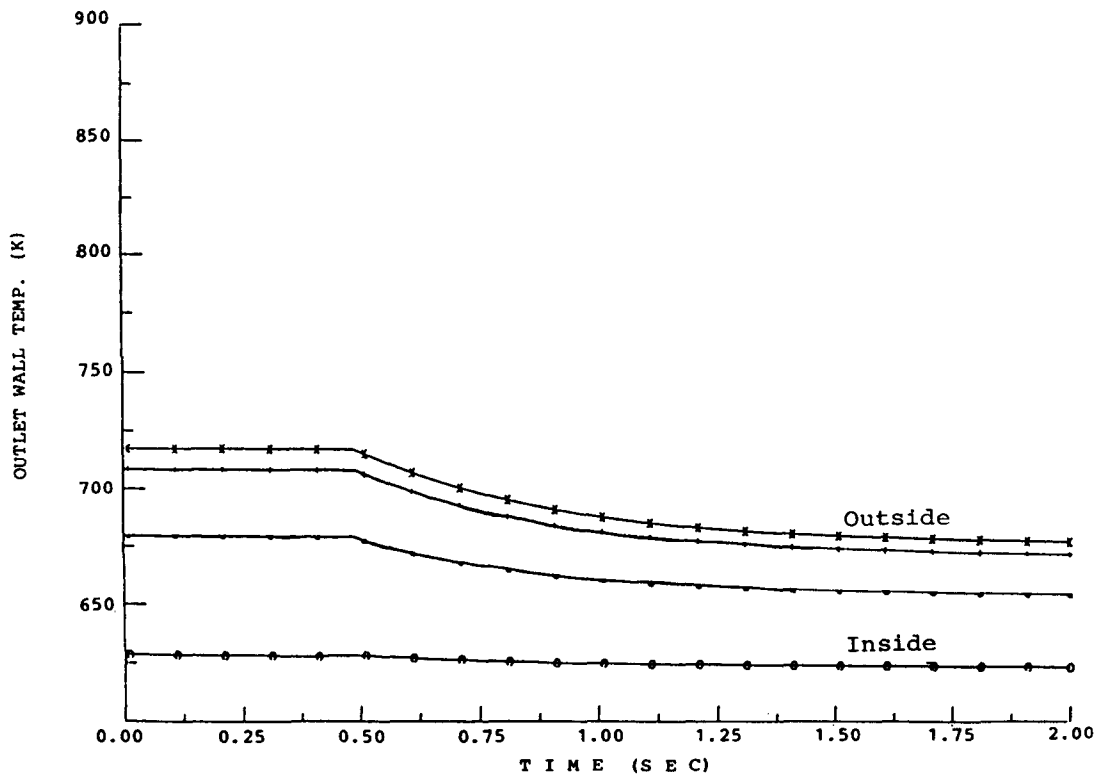

Fig. B2.8   RELAP5/MOD1/018   Roumy Case 2

was made as G exceeded the limit 1356 kg/m^2 s. The utilization
of only the W-3 correlation would probably have given about the
measured time to CHF. In Fig. B2.4 the CHF-value is also plotted
according to the Biasi correlation (5). This correlation provided
larger CHF-values than the combination W-3-modified Zuber corre-
lation.

Similar results were obtained with TRAC(PF1) (Biasi correlation)
and with NORA (modified Zuber correlation). The utilization of
the modified Zuber correlation and the Biasi correlation in this
case requires the calculation of subcooled void or subcooled
actual quality. Since both RELAP5 and TRAC are not yet capable of
calculating subcooled void formation it is not surprising that
they failed in the CHF-predictions when these correlations are
used.

The CE/EPRI Experiment

The CE/EPRI experiment was selected from a series of blowdown
experiments (59) conducted using a loop containing a vertical
single tube as the test section (Fig. B2.9). The heated length
was 3.81 m and the initial conditions were typical for a PWR
(see Table 4.2.I). The test section was a 0.0127 m outside dia-
meter Incoloy-800 tube having a 0.00125 m wall thickness. It
was instrumented with wall thermocouples and differential pres-
sure transducers. The twenty wall thermocouples were distributed
along 12 axial locations as can be seen in Fig. B2.9. The tran-
sient two-phase mass flow rate at the test section inlet and out-
let was measured by two groups of instruments each consisting of
a turbine meter, drag screen meter and gamma densitometer. The
mass flow rate was determined by combining the turbine and den-
sitometer readings assuming homogenous flow*. The test section
inlet and outlet fluid temperatures were also measured. The
measurements of void fractions, fluid temperatures and wall
surface temperatures during the selected blowdown experiment are
shown in Figs. B2.10 to B2.12. The time to CHF was about 1.0 sec.

----

* This assumption is justified for higher mass flows, however
at low mass flow rates its validity is questionable.

In the calculations with the three computer programmes only the test section was modelled. Thus some adequate boundary conditions had to be given. The boundary conditions used in these calculations were the outlet pressure (Fig. B2.13), the inlet massflow (Fig. B2.14) and the test section power (Fig. B2.15). As the programmes required the phasic massflows the total massflux in Fig. B2.14 had to be divided on each phase. This was accomplished by means of Figs. B2.10 and B2.11 with the assumption of saturated homogeneous flow.

The results of the RELAP5/MOD1 calculations are shown in Figs. B2.16 to B2.19. Similar results were obtained with TRAC(PF1) and NORA. The exit void fraction in Fig. B2.16 showed about the same trend as the measured exit void fraction in Fig. B2.10, being on a somewhat higher level though. The measured exit temperature peak shown in Fig. B2.11 was also obtained in the calculations (Fig. B2.17). The temperature peak occurred somewhat earlier in the calculations and, significantly, it was predicted to have a shorter duration, about 1 sec or half of the measured 2-sec duration. In Figs. B2.18 and B2.19 some calculated wall surface temperatures are shown.

A comparison with the measured temperatures in Fig. B2.12 reveals an almost correct calculated time to CHF while the rewetting was predicted to occur too early. A more notable discrepancy was the prediction of fairly uniform CHF and rewetting throughout the test section while the measurements indicated an axial propagation of the CHF and also of the rewetting.

There could apparently be two reasons for these discrepancies: first, of course, some inadequacies of the models used in the programmes, and secondly the utilization of inadequate boundary conditions. One of these is certainly the assumption of saturated homogeneous flow when evaluating the phasic flow components from the measurements.
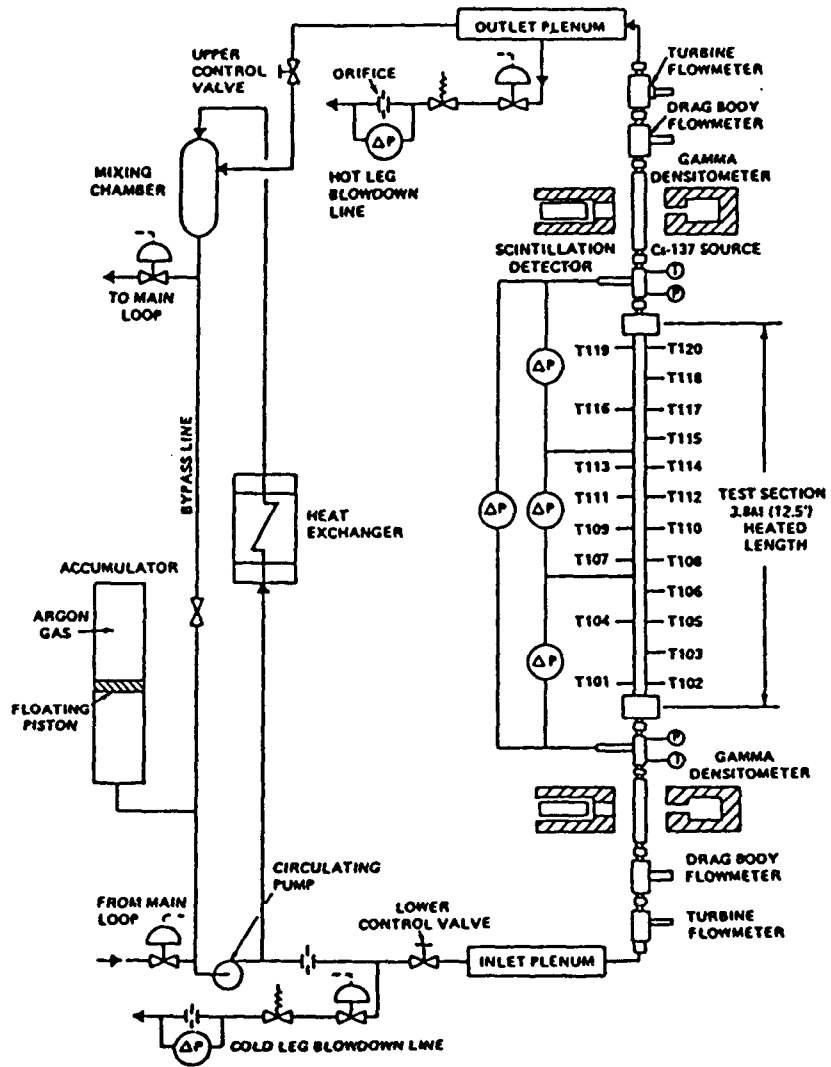
FIG. B2.9   CE/EPRI SINGLE TUBE BLOWDOWN LOOP (FROM REF. 59)
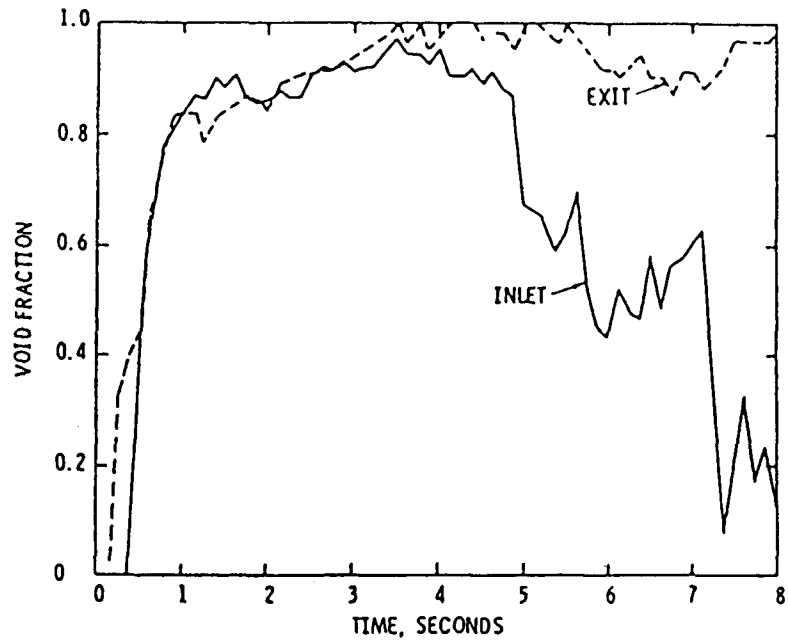
FIG. B2.10 Single tube transient void fractions
(FROM REF. 59)
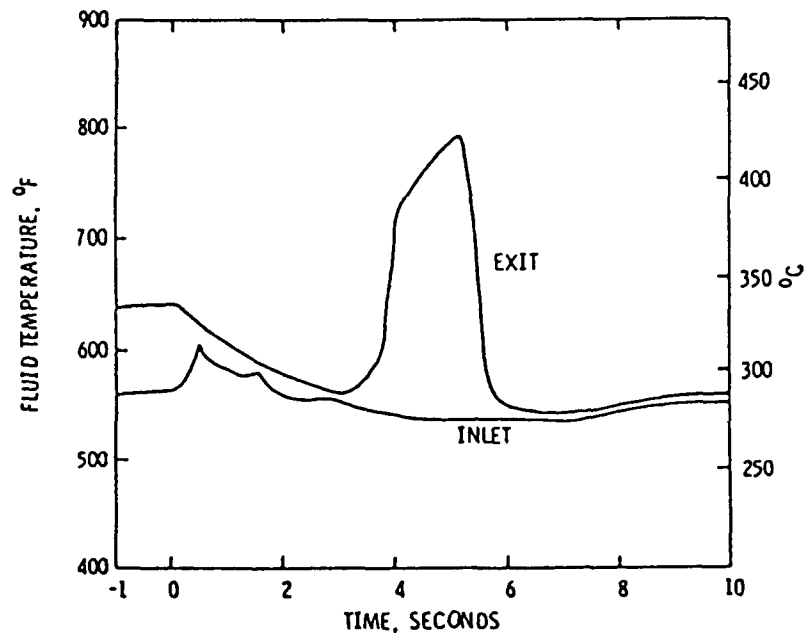
FIG. B2.11 Single tube transient fluid temperatures
(FROM REF. 59)
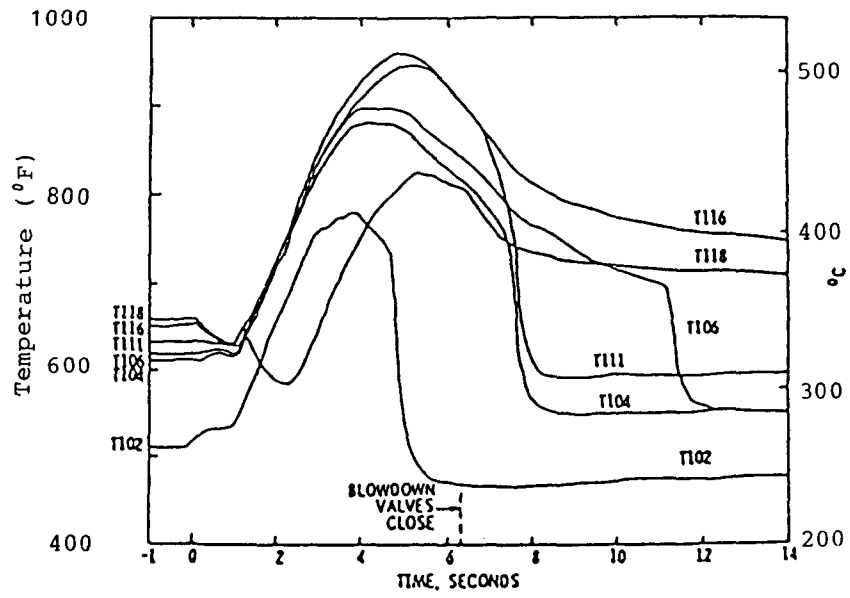
FIG. B2.12   TEST SECTION WALL SURFACE TEMPERATURES (FROM REF. 59)
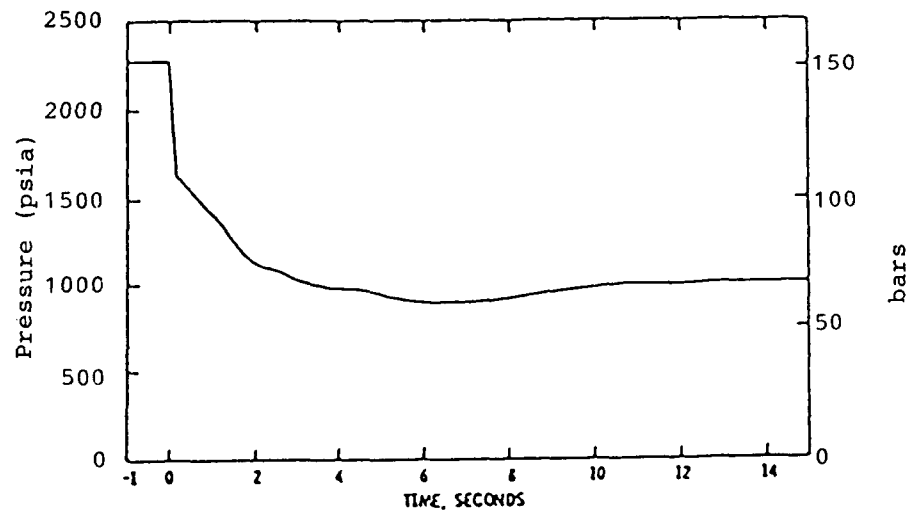
FIG. B2.13   TEST SECTION EXIT PRESSURE (FROM REF. 59)

FIG. B2.14   TEST SECTION INLET MASS FLUX (FROM REF. 59)

FIG. B2.15   TEST SECTION POWER (FROM REF. 59)

Fig. B2.16   CE/EPRI Case

Fig. B2.17   CE/EPRI Case

SAEK-5   RELAP5/MOD1/018   TEST CASE 3.

Fig B2.18   CE/EPRI Case

SAEK-5   RELAP5/MOD1/018   TEST CASE 3.
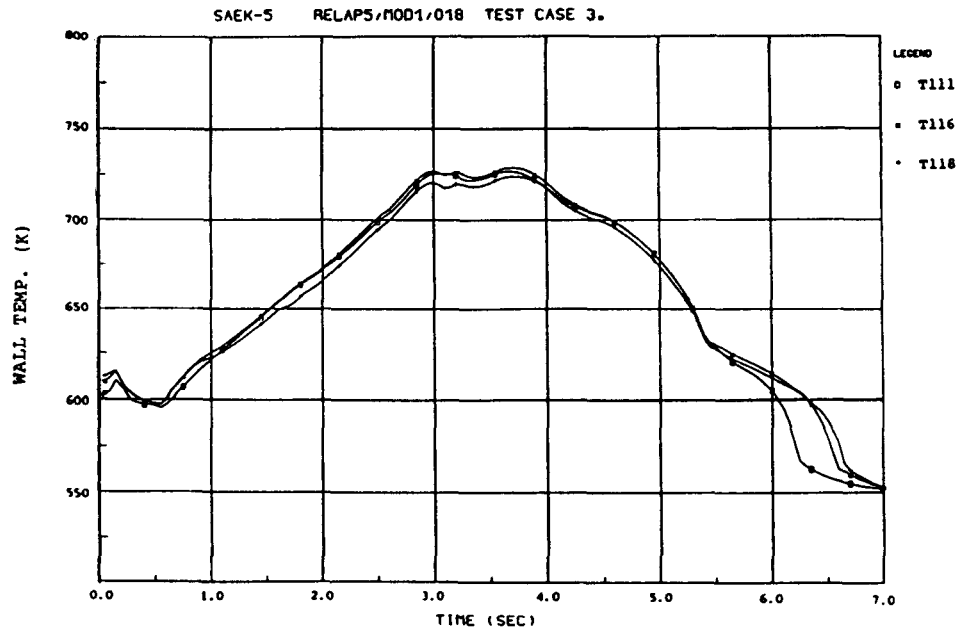
Fig B2.19   CE/EPRI Case

It soon became obvious from the results of the simulations of the three transient test cases described above that the calculations were influenced by a large number of utilized models and empirical correlations apart from the applied boundary conditions. Thus, it would be very difficult to assess the heat transfer correlations alone from these types of transie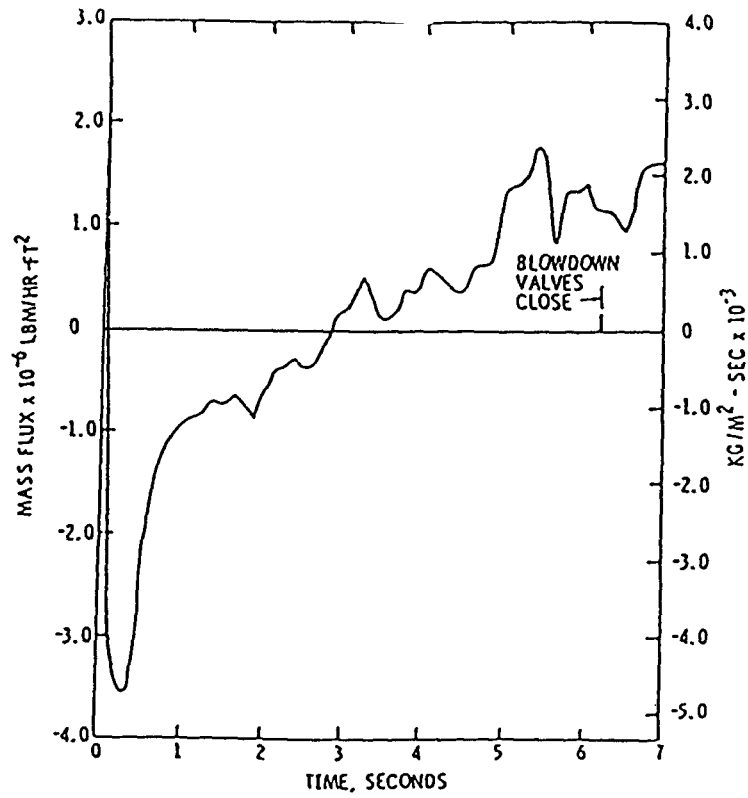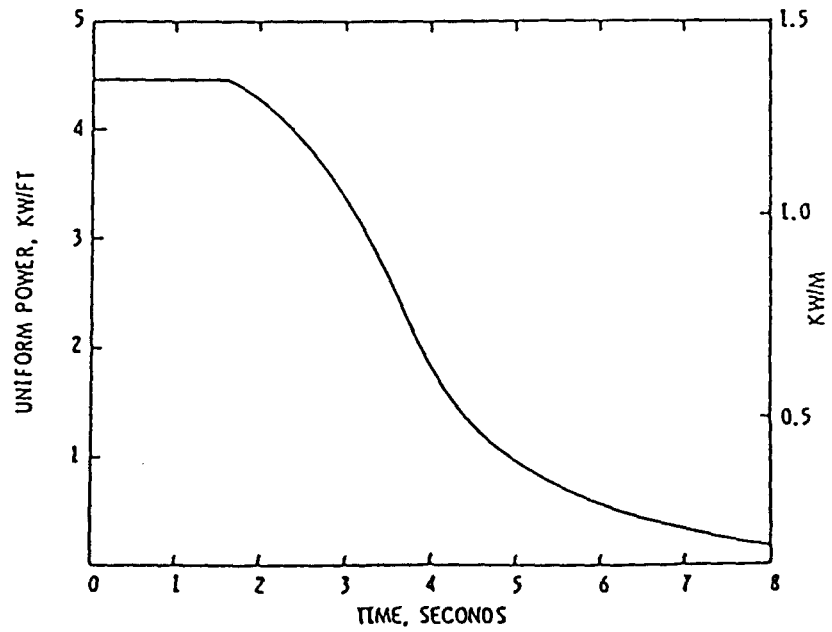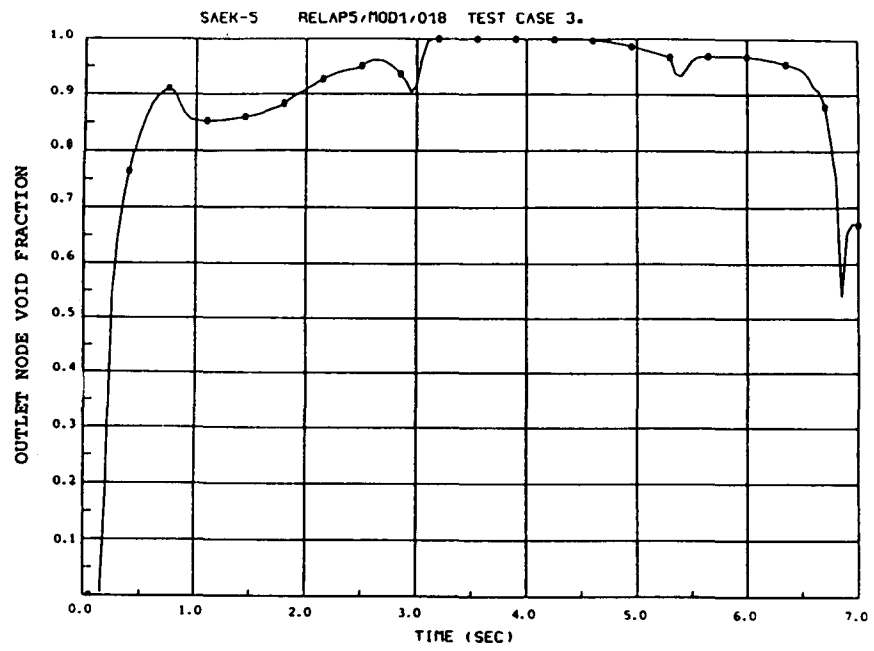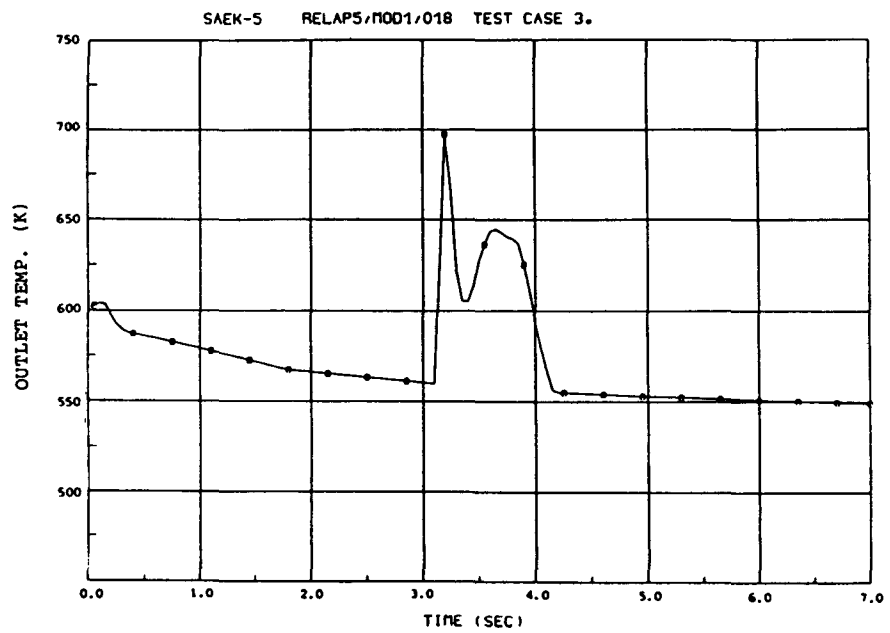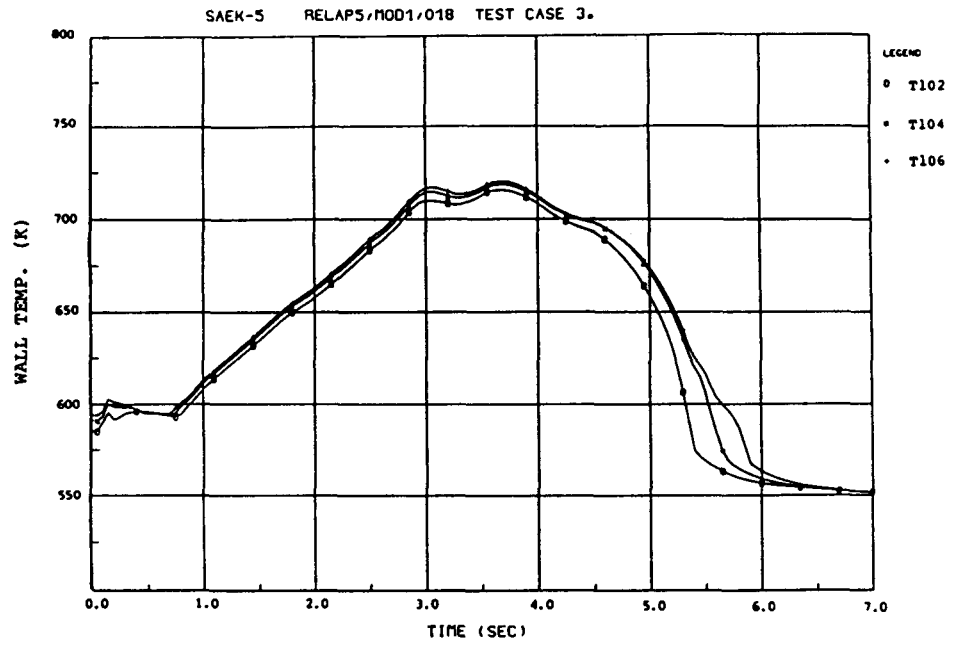nt experiments. More simplified experiments were desirable, preferably steady-state experiments with well-defined boundary conditions. In order to cover the complete spectrum of heat transfer modes experiments in which it was desirable to exceed CHF. Two groups of experiments which met these new requirements were found, the Becker and ORNL experiments.

The Becker Experiments

The Becker experiments were selected from a series of CHF and post-CHF experiments reported in (2). As the CHF in these experiments all were of the annular liquid film dryout type, the term dryout (DO) will be used henceforth. The test section used in these experiments was a vertical tube, directly heated in the tube wall and insulated on the outer surface. The inside diameter was 0.0149 m and the heated length was 7 m with an uniform power distribution. The lower 3 m was instrumented with wall thermocouples at every 0.25 m and the upper 4 m at every 0.1 m (cf Fig. B2.20).

The steady-state conditions for the seven selected cases are shown in Table 4.2.I. The cases were calculated with the computer programmes RELAP5/MOD1, TRAC(PF1) and NORAS (the steady state version of NORA) and the steady state conditions in Table 4.2.I were used as boundary conditions, viz. exit pressure, inlet mass flow, inlet subcooling and heat flux.

The first calculations of these test cases (or some of the cases) are reported in (60) to (63). As there were no provisions in RELAP5 nor in TRAC to calculate the steady state this had to be done by analyzing a transient with time-invariant boundary conditions until the solution was stable. With 20 to 35 axial

nodes the CPU-time on a CDC CYBER 170-835 computer for obtaining the steady state in these cases ended up in the range 10 to 20 minutes while the NORAS programmes required only a few seconds. For that reason only some of the selected seven cases were calculated with RELAP5 and TRAC while all of them were calculated with NORAS.

The RELAP5/MOD1 calculations were carried out with two different CHF-correlations, the W-3 correlation (4) and the Biasi correlations (5). In all of the cases using the W-3 correlation the predicted locus of DO were too far upstream. In the calculations using the Biasi correlations the high flow DO was due to a cut-off void limit of 0.96. A more thorough examination of these results revealed that the value of DO too far upstream was caused by some flow oscillations during the course to steady state in combination with the incapability of RELAP5 to rewet an initially dry surface without decreasing the surface temperature, i.e. without decreasing the power.

The results from the TRAC(PF1) calculations revealed fairly accurate DO predictions. TRAC applies the Biasi correlation; however, in none of the cases did this correlation determine the locus of DO. Rather, an arbitrarily chosen cutoff void limit of 0.97 caused DO.

Both RELAP5 and TRAC calculations revealed significant discrepancies between predicted and measured wall surface post-DO temperatures. The post-DO conditions are known to be strongly dependent on the conditions at the locus of DO. It was therefore not possible to decide whether wall temperature discrepancies were due to an erroneous prediction of post-DO heat transfer.

The NORAS calculations (63) used three different CHF-correlations: Biasi, CISE4 and Becker (64). Biasi and Becker correlations predicted DO as lying too far downstream while, on the other hand, the CISE4 correlation predicted DO as too far upstream at high quality and too far downstream at low quality. Calculations were also performed with either Biasi or CISE4 correlation adjusted by a factor to obtain predicted DO locations as close as possible to

measured values. This was made in order to obtain a reasonable comparison between predicted and measured post-DO wall surface temperatures. The results from these calculations indicated that the post-DO interfacial heat transfer needed some improvements. For Becker case 1 the interfacial heat transfer was varied until a satisfactory agreement between predicted and measured post-DO temperatures was obtained (Fig. B2.21).

The major conclusions from these calculations were that the DO predictions in all of the codes needed substantial improvements and that the post-DO heat transfer calculations needed refinements.

Some examinations of the heat transfer package of RELAP5/MOD1 (65,66) revealed that the static equilibrium quality was used as an input to correlations even though the equilibrium flow quality was used in the development of the correlations. At the DO location the vapour velocity may be much higher than that of the liquid. Consequently, the flow quality will be higher than the static quality. This means that the use of static quality in a correlation will result in higher critical heat flux than if the flow quality was used.

It was also apparent that the interfacial heat transfer was too high in RELAP5 and TRAC(PF1) and too low in NORA.

In order to examine the post-DO heat transfer calculations in RELAP5/MOD1 and TRAC(PF1) five of the Becker test cases were recalculated with the experimental locus of DO given as input (67,68). To accommodate this new input the RELAP5 and TRAC computer programme had to be somewhat modified, especially the input routines and the routine performing the CHF calculations. When the DO locus was inserted, the uncertainties in the DO predictions were eliminated and the results from the post-DO heat transfer calculations could be used to examine the pertinent models and correlations more thoroughly. The results from the calculations with RELAP5 are shown in Figs. B2.22 to B2.26. The predicted post-DO wall temperatures were significantly lower than the measured ones. Moreover, it appeared that the calculations

of the nonequilibrium effects typical for the post-DO regime were inadequate in that no vapour superheat was calculated (the liquid and vapour post-DO temperatures were about the same).

Four cases were recalculated with a test version of RELAP5/MOD 1 in which the post-DO interfacial mass transfer and the post-DO wall-to-fluid heat tranfer models were completely modified (69). The vapour phase was now allowed to be superheated when the quality exceeded the quality at DO rather than a fixed value*. In the post-DO region the vapour generation rate was calculated from a new correlation (6) and the wall heat transfer was assumed to take place from the wall surface to the superheated vapour phase only. The predicted wall temperature distributions in the post-DO region showed substantial improvements compared to the earlier calculations (Figs. B2.27 to B2.30).

The modifications outlined above had been adopted ealier in NORAS (70,71) and the Becker cases had been recalculated. The NORAS calculations then gave about the same temperature distributions in the post-DO region as the RELAP5 calculations described above. The modified NORAS was also used to simulate some rod bundle experiments conducted at ORNL. These are discussed below.

----

* Originally RELAP5 made use of a fixed static quality value to determine which phase was saturated. If the static quality was less than 0.5 the vapour phase was saturated; otherwise the liquid phase was saturated. The phase that was unsaturated was allowed to be either subcooled or superheated.

Test Section
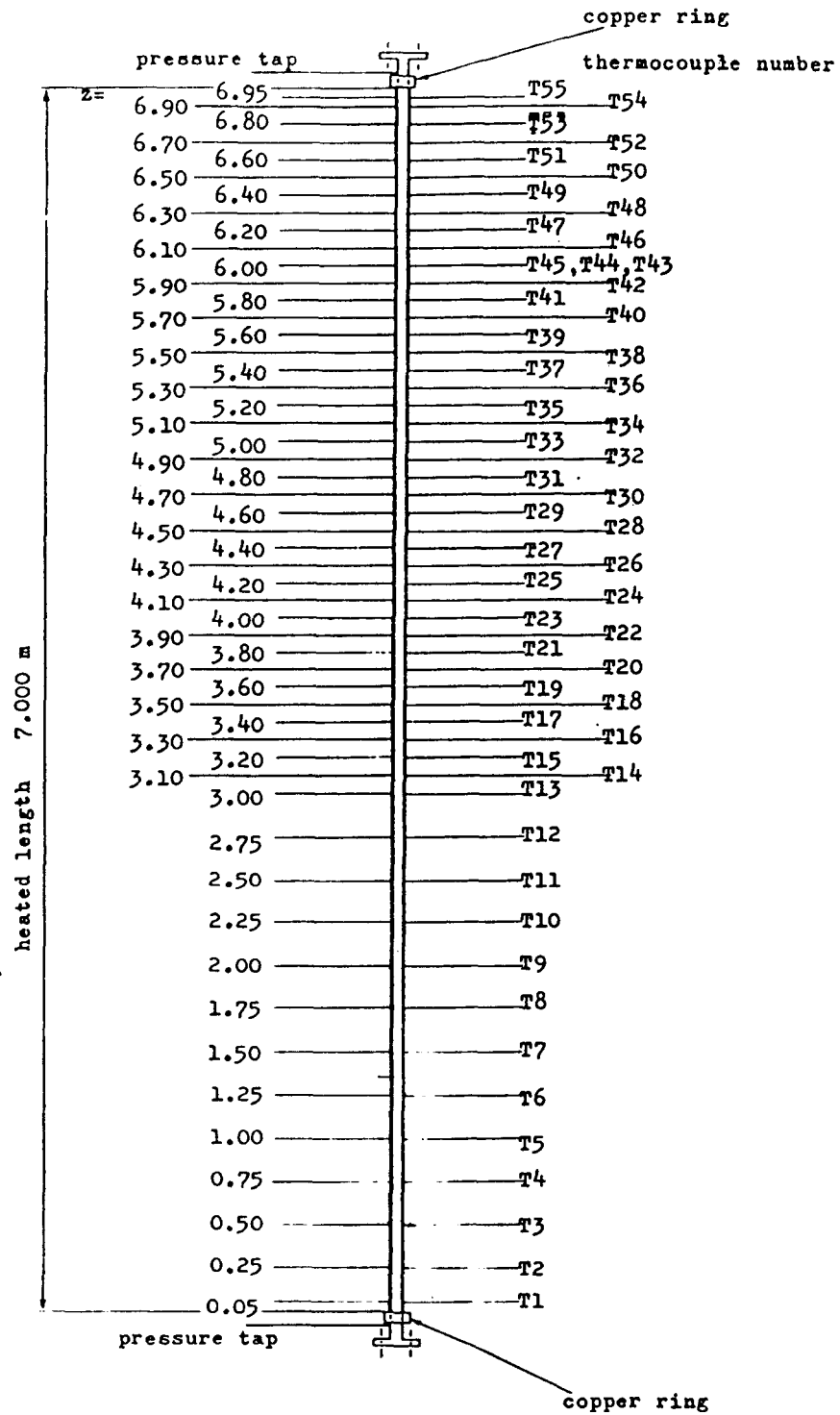
FIG. B2.20   BECKER TEST SECTION (FROM REF. 2)
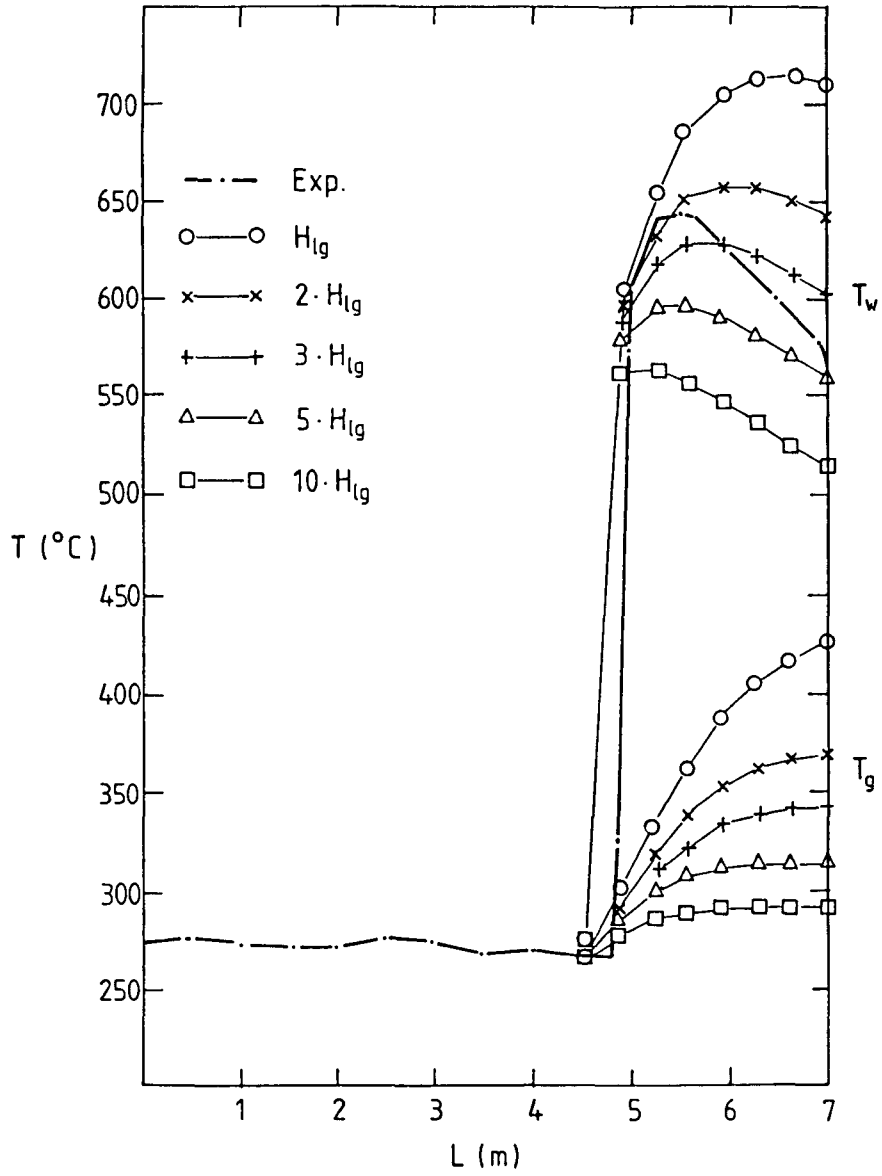
Fig. B2.21   BECKER CASE 1

NORA TEMPERATURES

P = 5.2 MPa   G = 1476 kg/m^2 s

ΔT_{sub} = 9.8 K   Q = 1.015 MW/m^2

SAEK-S   RELAP5/MOD1/019   BECKER CASE 1.
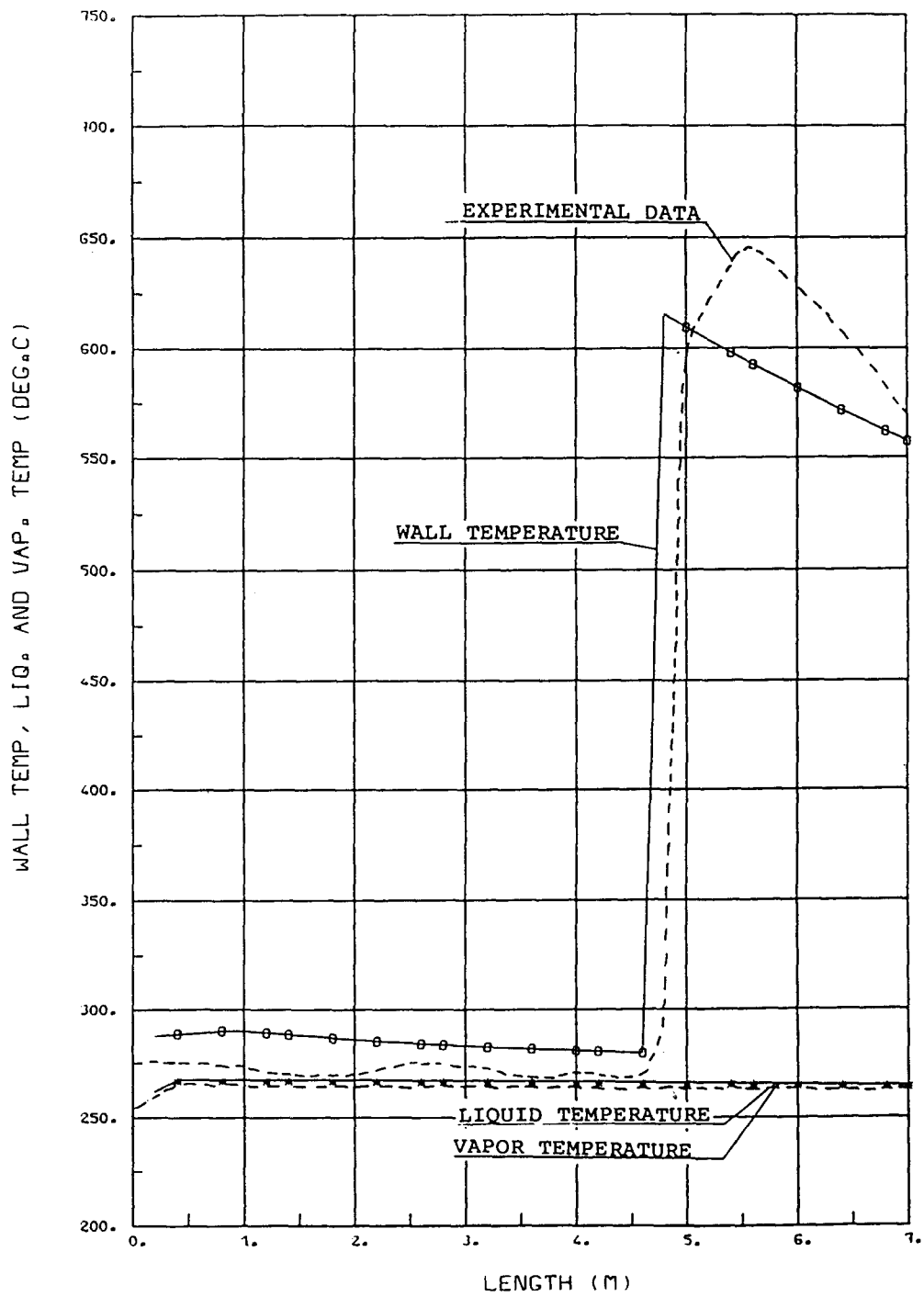
FIGURE B2.22

SAEK-5   RELAP5/MOD1/019   BECKER CASE 2.
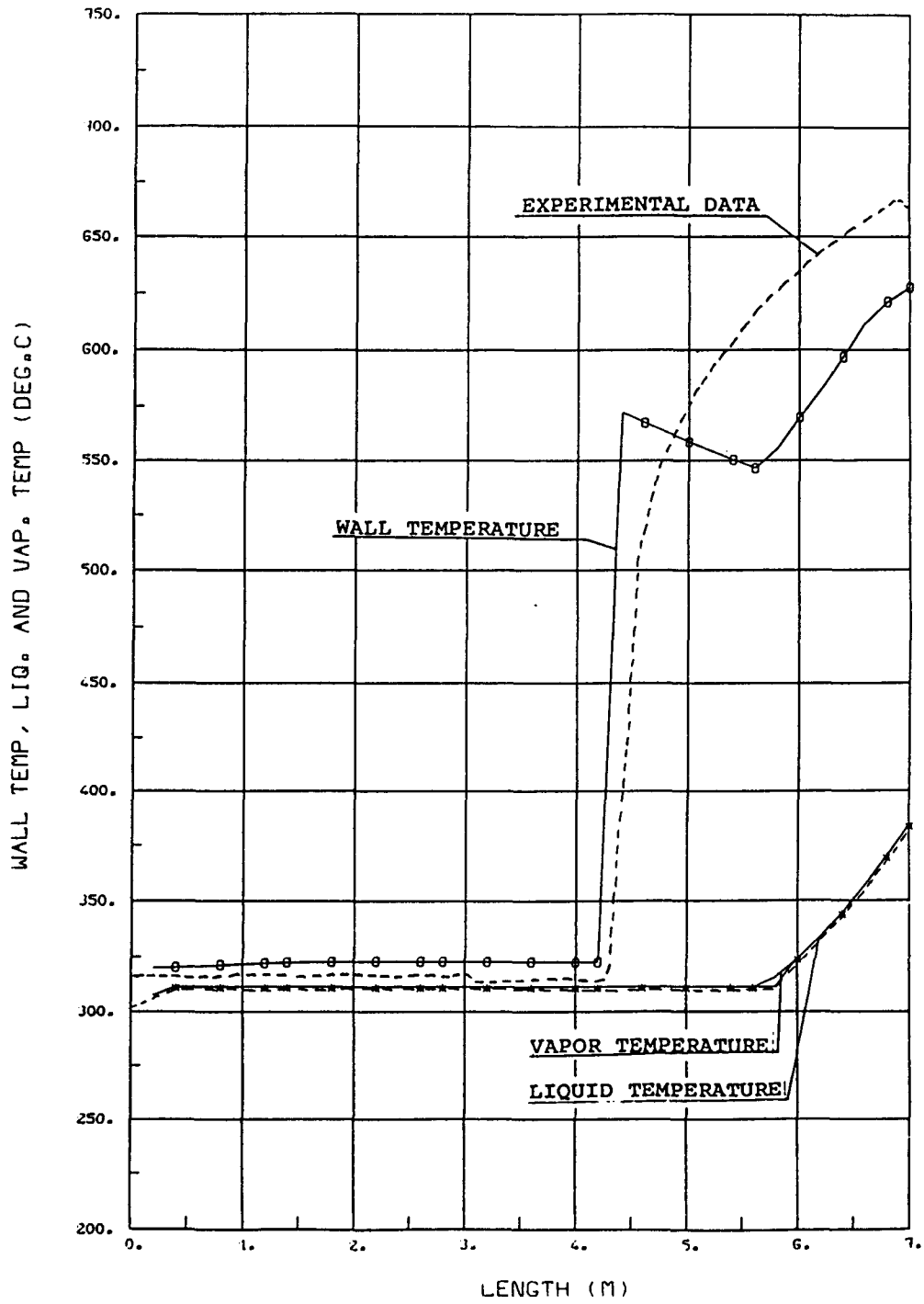
LENGTH (M)
FIGURE B2.23

SAEK-5   RELAP5/MOD1/019   BECKER CASE 3.

LENGTH (M)
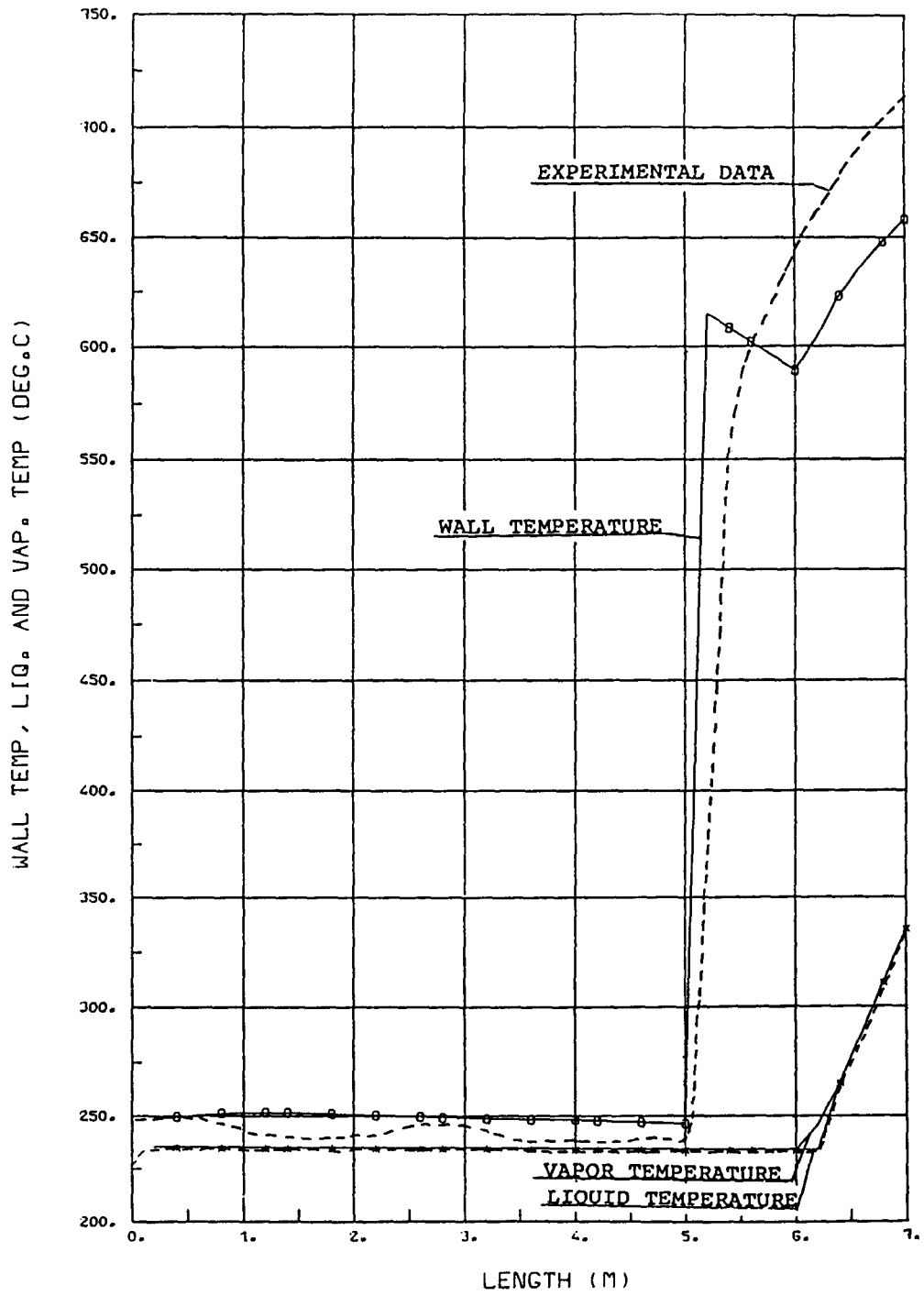
FIGURE B2.24

SAEK-5   RELAP5/MOD1/019   BECKER CASE 4.
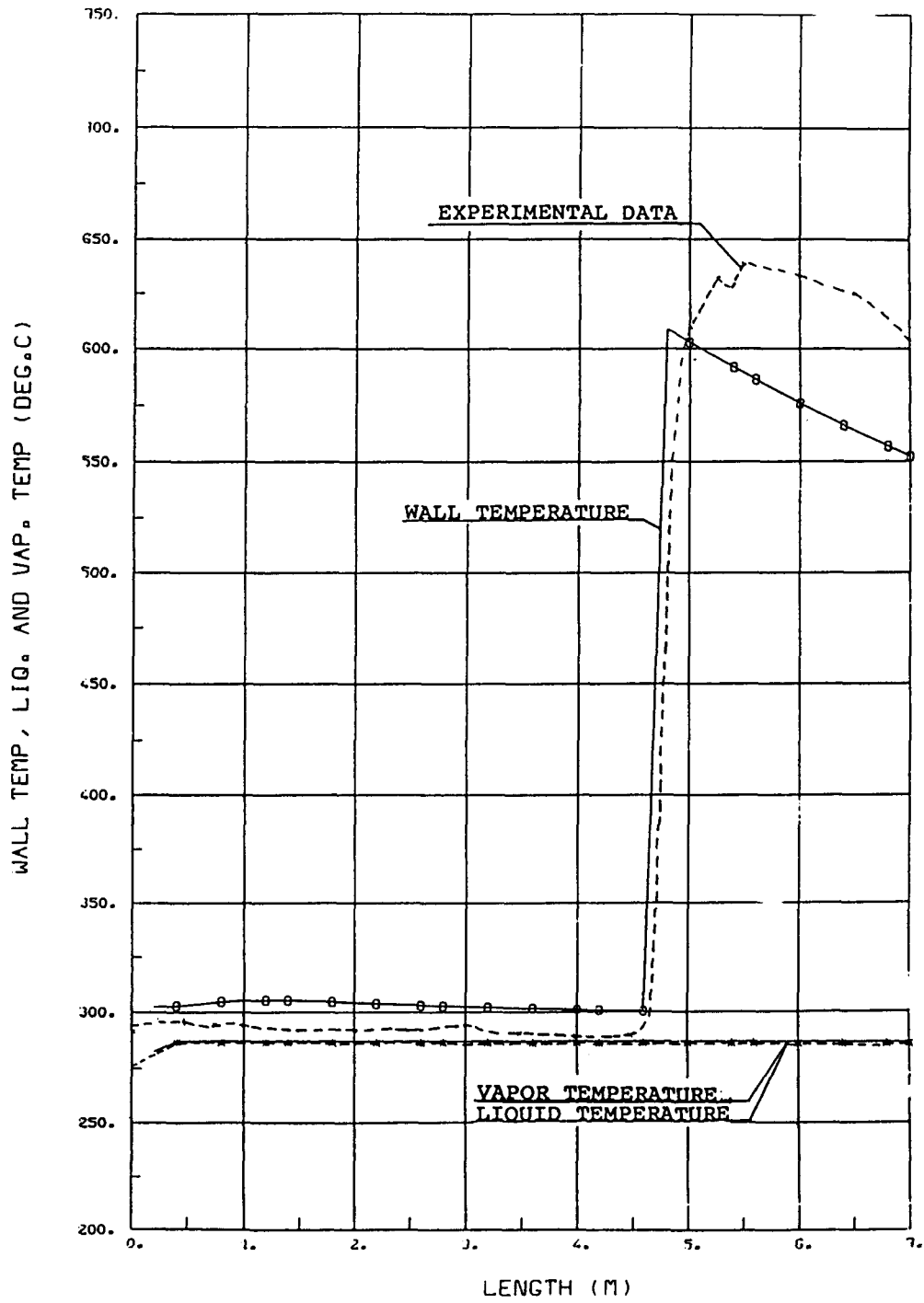
FIGURE B2.25

SAEK-5   RELAP5/MOD1/019   BECKER CASE 7.

LENGTH (M)
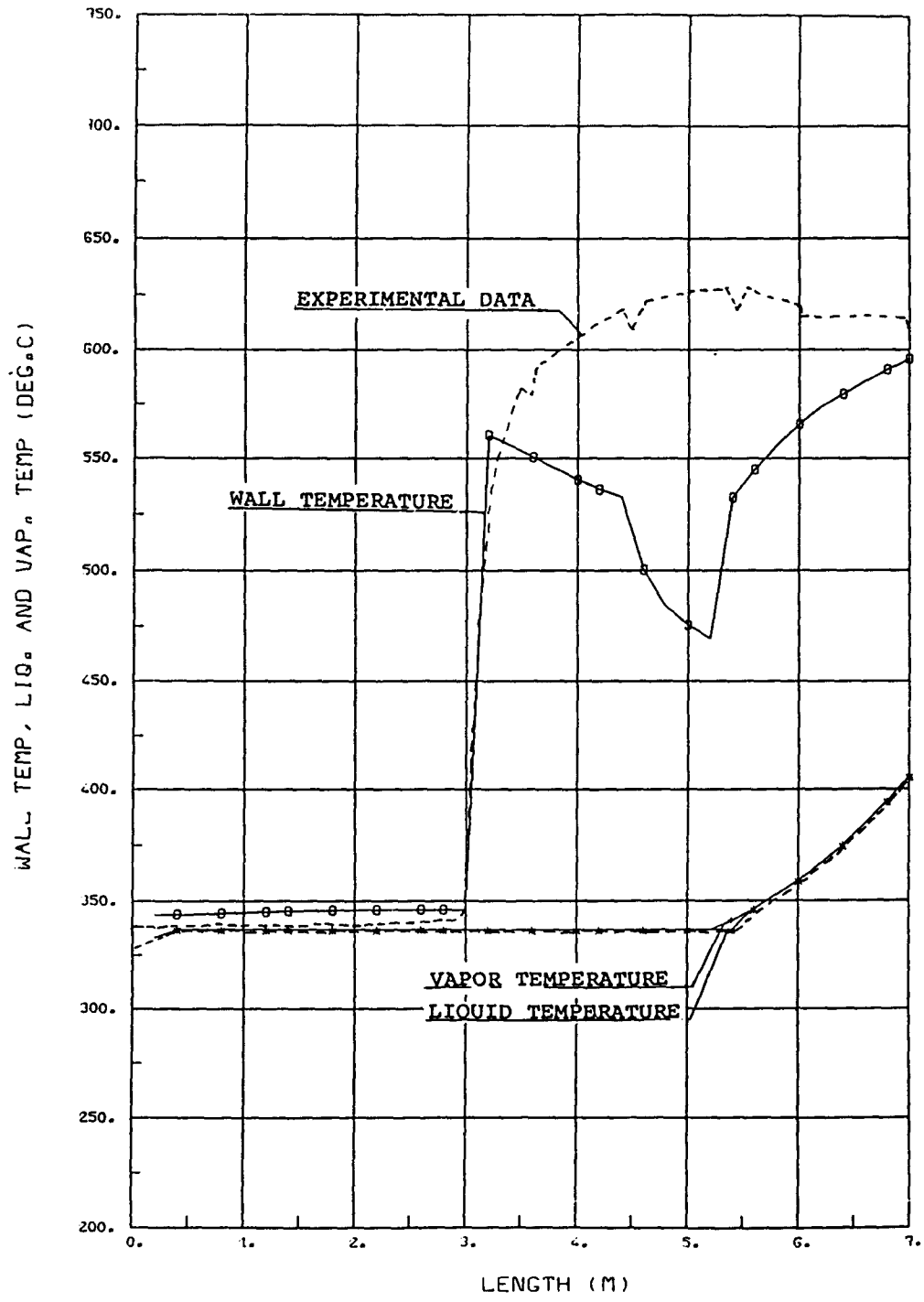
FIGURE B2.26

SAEK-5   RELAP5/MOD1/025   BECKER CASE 1.

WALL TEMP,LIQ. AND VAP. TEMP (DEG.C)

LENGTH (M)
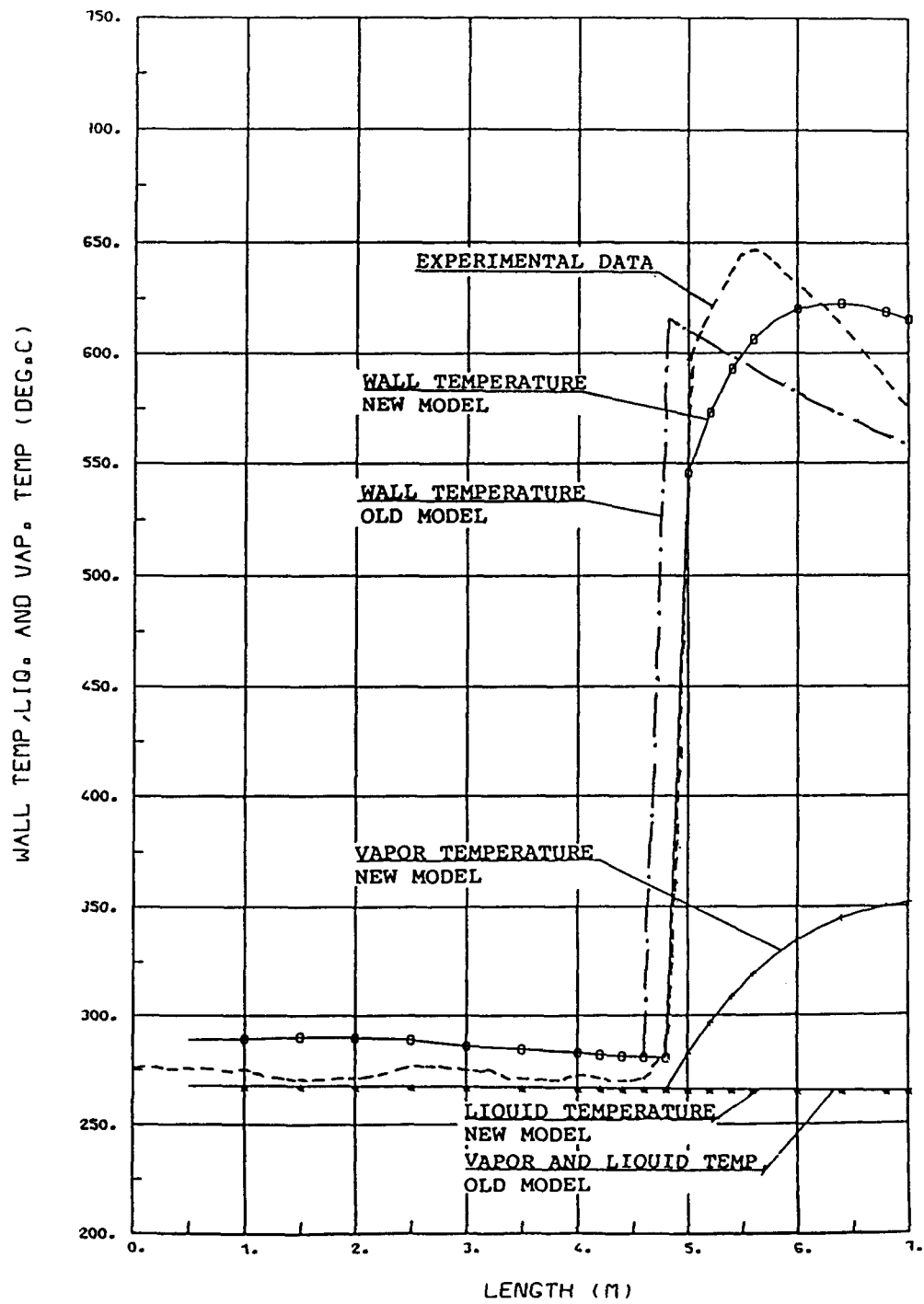
FIGURE B2.27

SAEK-5   RELAP5/MOD1/025   BECKER CASE 2.

WALL TEMPERATURE
NEW MODEL

EXPERIMENTAL DATA

WALL TEMPERATURE
OLD MODEL

VAPOR TEMPERATURE
NEW MODEL

VAPOR AND LIQUID TEMP
OLD MODEL

LIQUID TEMPERATURE
NEW MODEL

LENGTH (M)
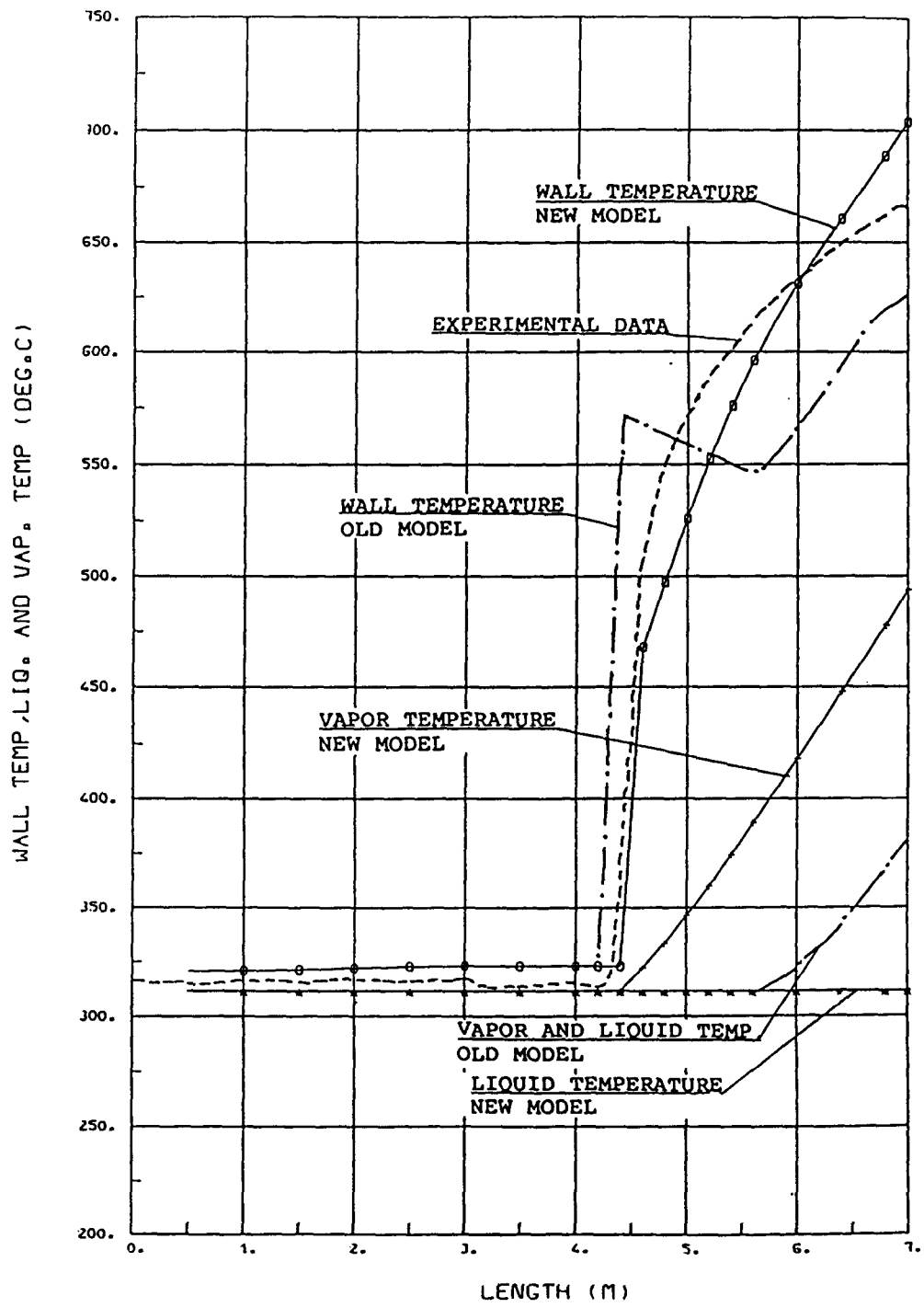
FIGURE   B2.28

SAEK-5   RELAP5/M001/025   BECKER CASE 3.
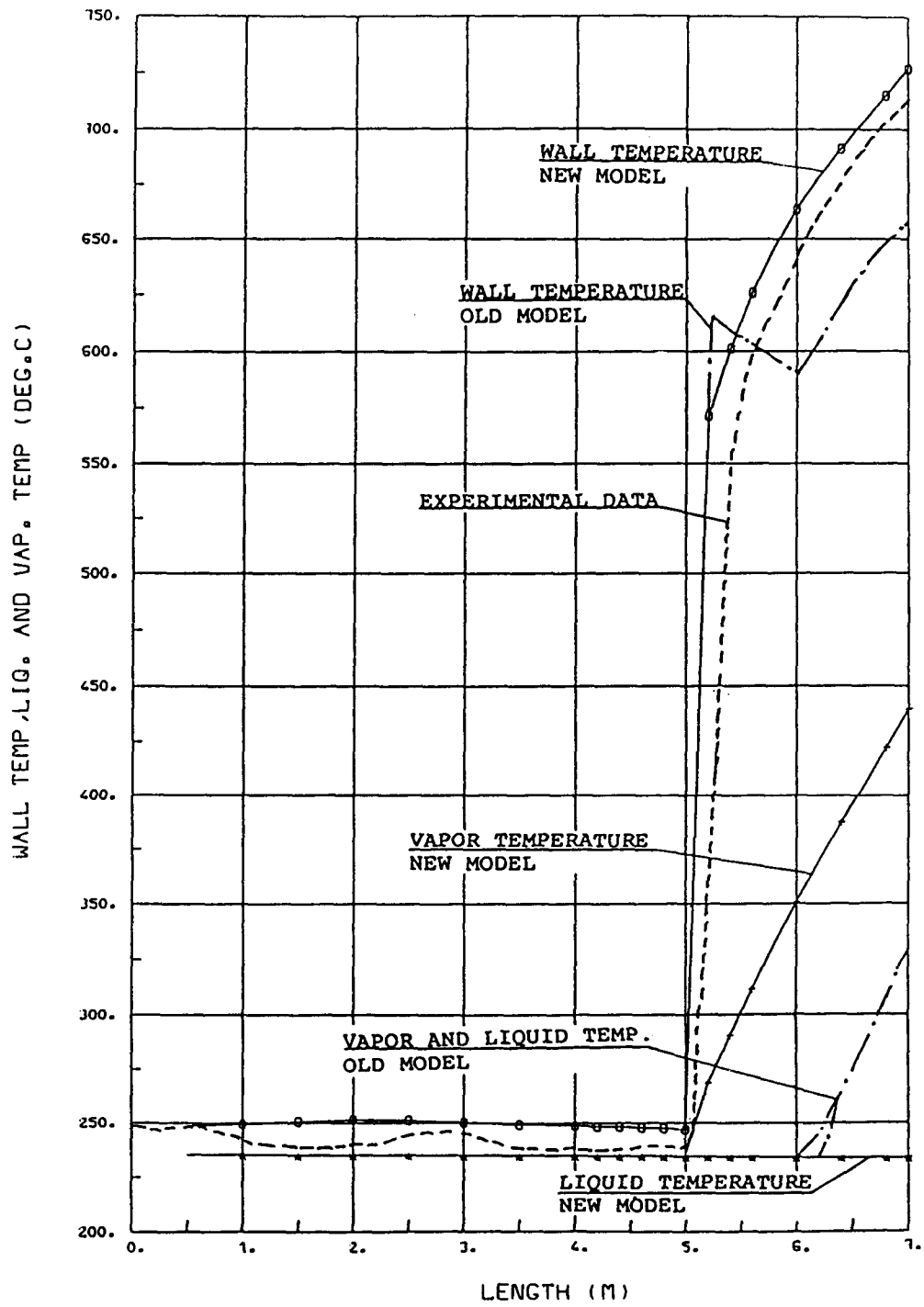
FIGURE B2.29

SAEK-5   RELAP5/MOD1/025   BECKER CASE 7
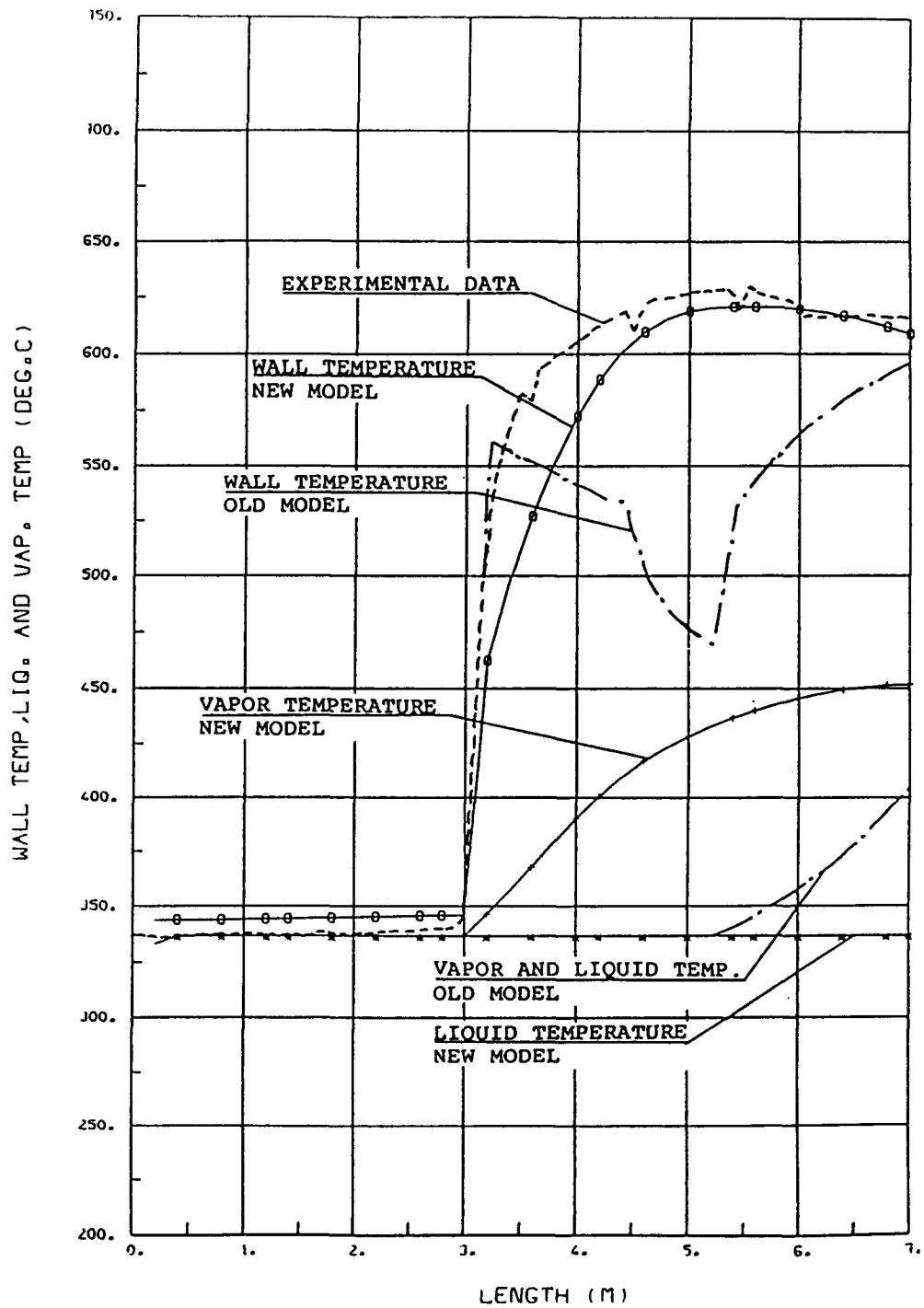
FIGURE   B2.30

The ORNL experiments

These experiments were conducted at Oak Ridge National Lab-
oratory (ORNL) in the Thermal Hydraulic Test Facility (THTF)
and are reported in (72). The test section was an electrically
heated rod bundle comprising 64 rods in a square lattice. A
cross section of the bundle is shown in Fig. B2.31 where a
cross section of one of the heater rods is shown as well. The
rod surface temperatures were estimated from measured inter-
nal temperatures and known heating power. The rod outside
diameter was 0.0095 m and the rod pitch 0.0127 m.

The power distribution was uniform both axially and radially
over the cross section. Figure B2.32 shows the axial locations
of spacer grids and thermocouple levels. The heated length was
3.66 m.

Six experiments were selected as test cases from the complete
series. The steady state conditions are given in Table 4.2.I.
The bundle was modelled in NORAS as a 3.66 m long heated
channel divided into 15 axial nodes of equal length (0.24
m). The 60 heated rods were represented by one single heated
wall with heated perimeter equal to the sum of the heated
perimeters of each heated rod. Hydraulically the bundle
geometry was represented by a single channel with hydraulic
diameter and flow area equal to those for the bundle.

The calculations were carried out with NORAS and the same mo-
dels and correlations as in the Becker cases described above
were used. Figures B2.33 to B2.38 show the calculated wall tem-
peratures in comparison with the measured values. The measured
values are given in terms of an average value for all rods at a
particular level and the standard deviation. All rods where
wetted are indicated on the top of the figures at the highest
location in the channel. At the lowest location all rods
were dry. The calculated vapour temperatures are shown as well.

The measured data clearly show the influence of the spacers.
The spacer locations are indicated on the top of the figures.

COLD RODS

316 STAINLESS
STEEL SHEATH

INCONEL 600
HEATING ELEMENT

30°

BORON
NITRIDE

0.05 CM TC
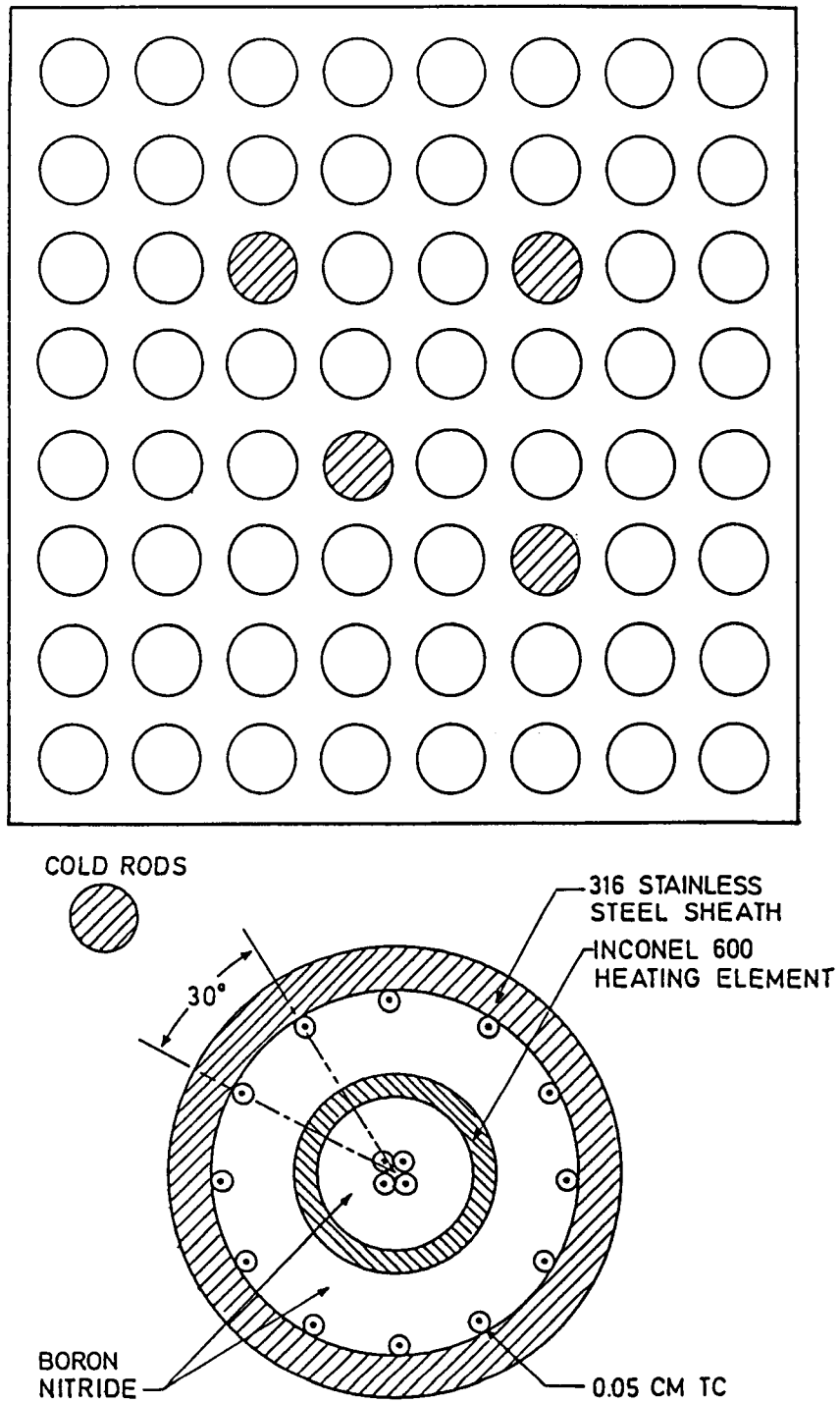
Fig. B2.31 ORNL - 64 rod test bundle. Cross section of
bundle and single heater rod (FROM REF. 72)
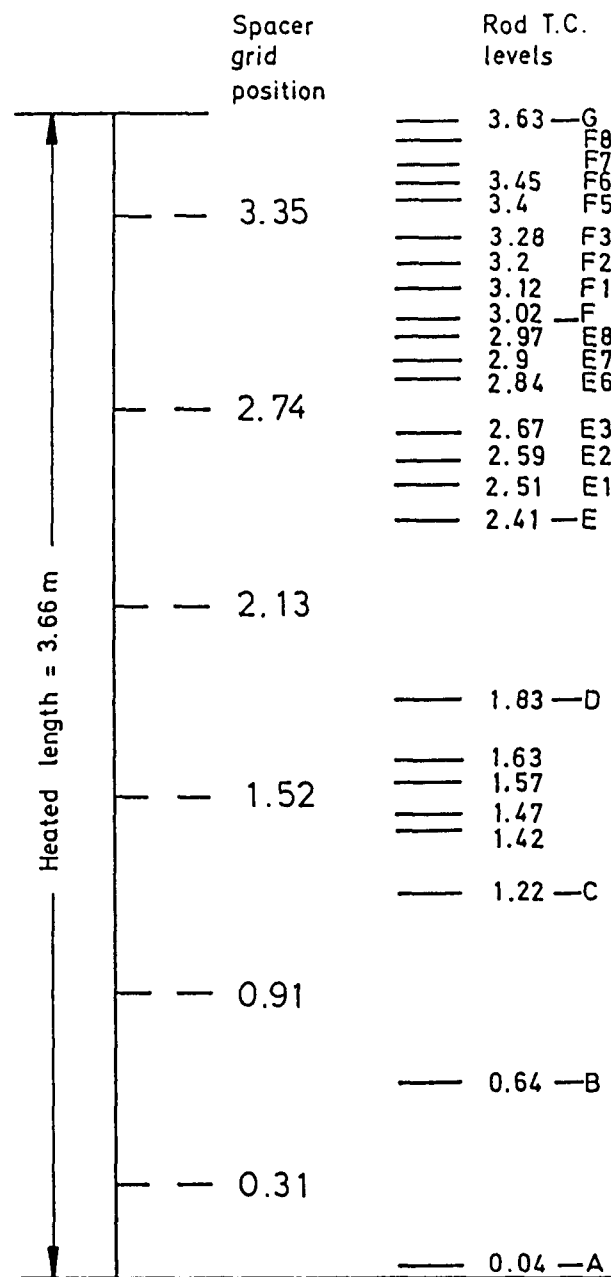
Fig. B2.32 Axial location of spacer grids and thermocouples for ORNL test bundle (FROM REF. 72)
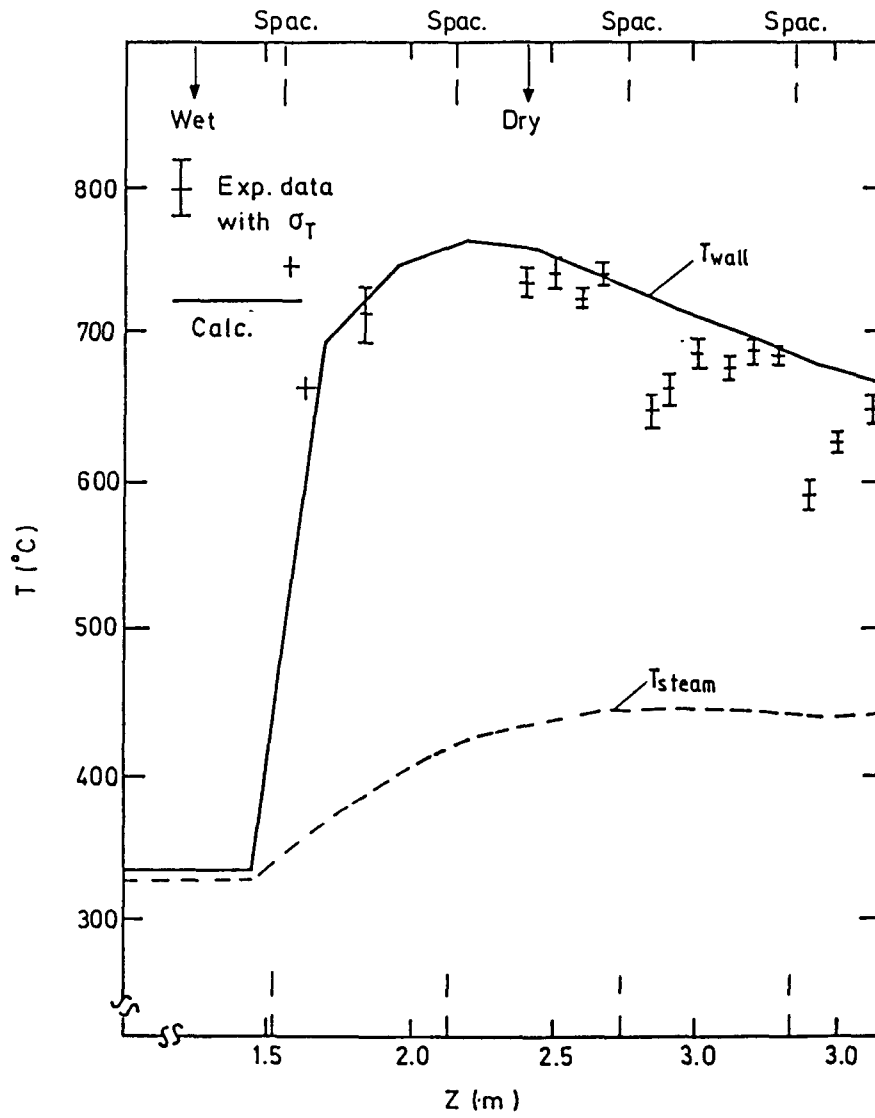
Fig. B2.33 ORNL Case B

P = 12.76 MPa	ΔT_{subc} = 19. °C
G = 712.9 kg/m²s	$T_{sat.}$ = 329.3 °C
Q = 0.91 MW/m²	
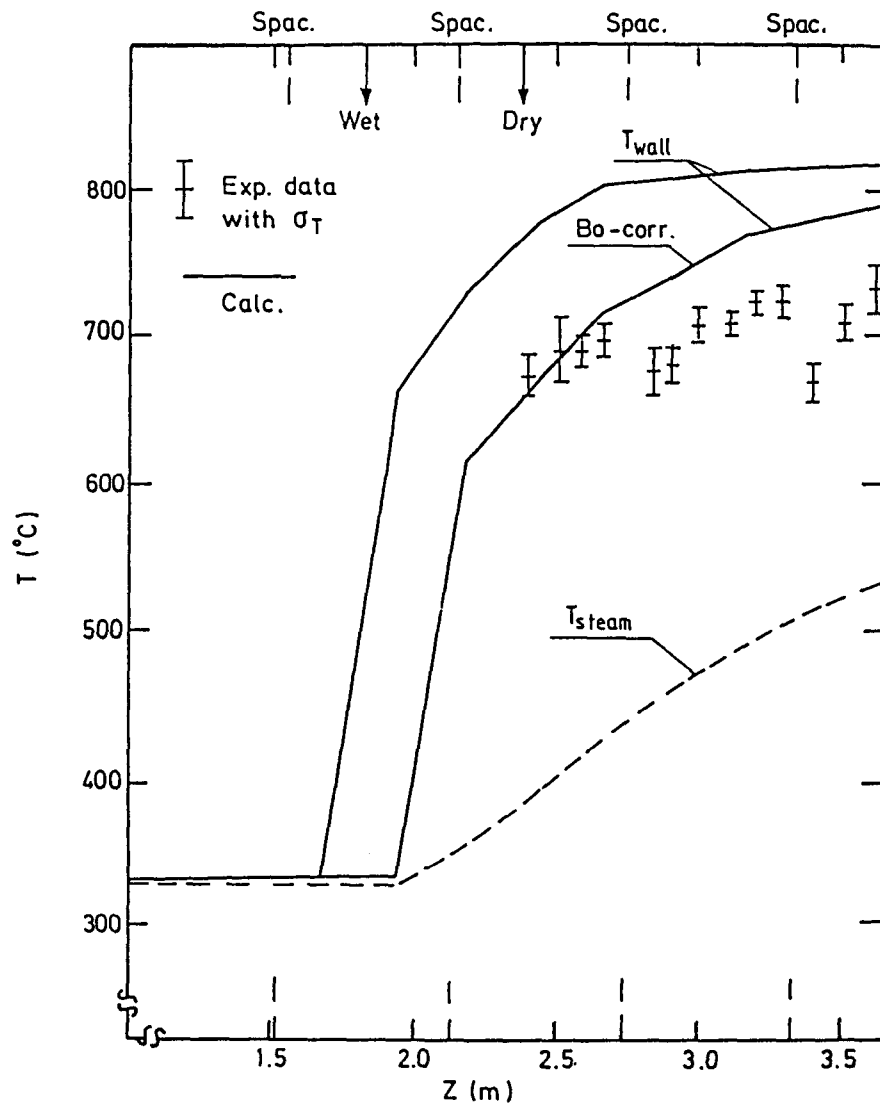
Fig. B2.34 ORNL Case C

P = 12.46 MPa ΔT_{subc} = 3.5 °C

G = 334.2 kg/m²s T_{sat} = 327.5 °C

Q = 0.56 MW/m²
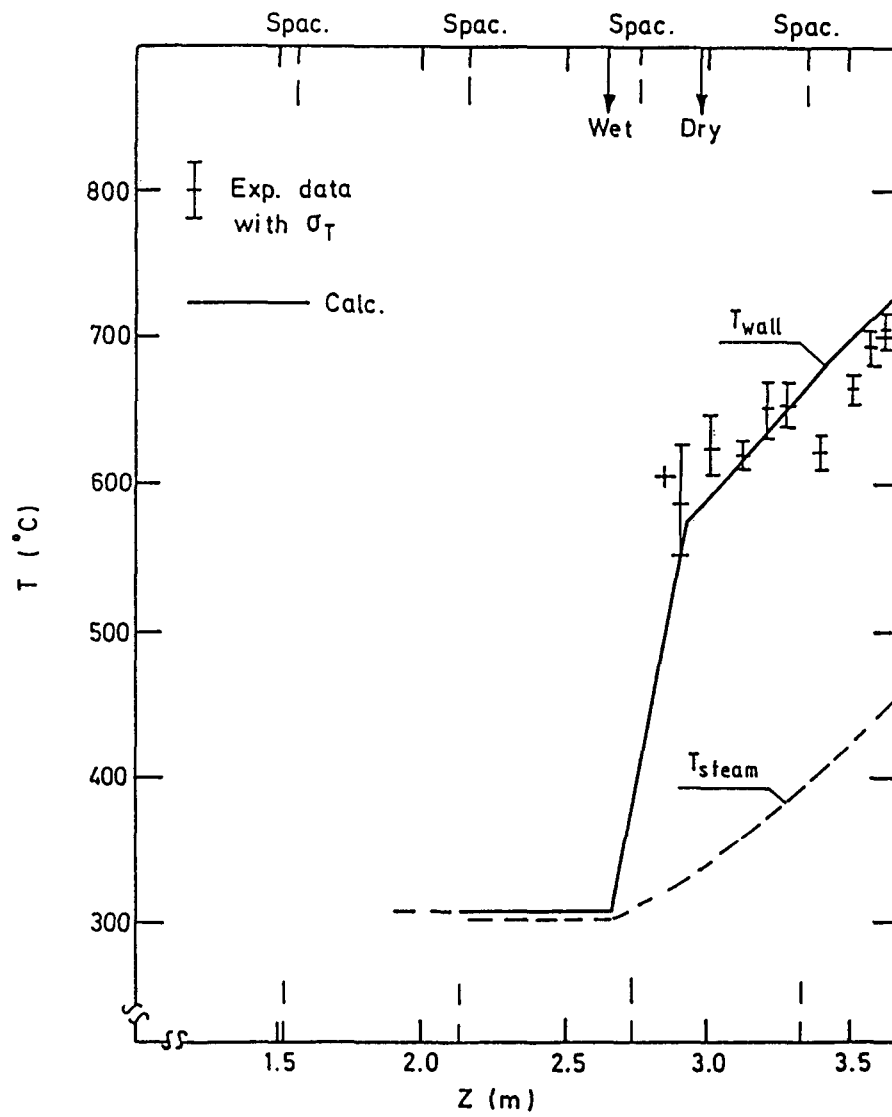
Fig. B2.35 ORNL Case H

P = 8.86 MPa ΔT_{subc} = 38. °C

G = 256. kg/m^2 s $T_{sat.}$ = 302.4 °C

Q = 0.417 MW/m^2
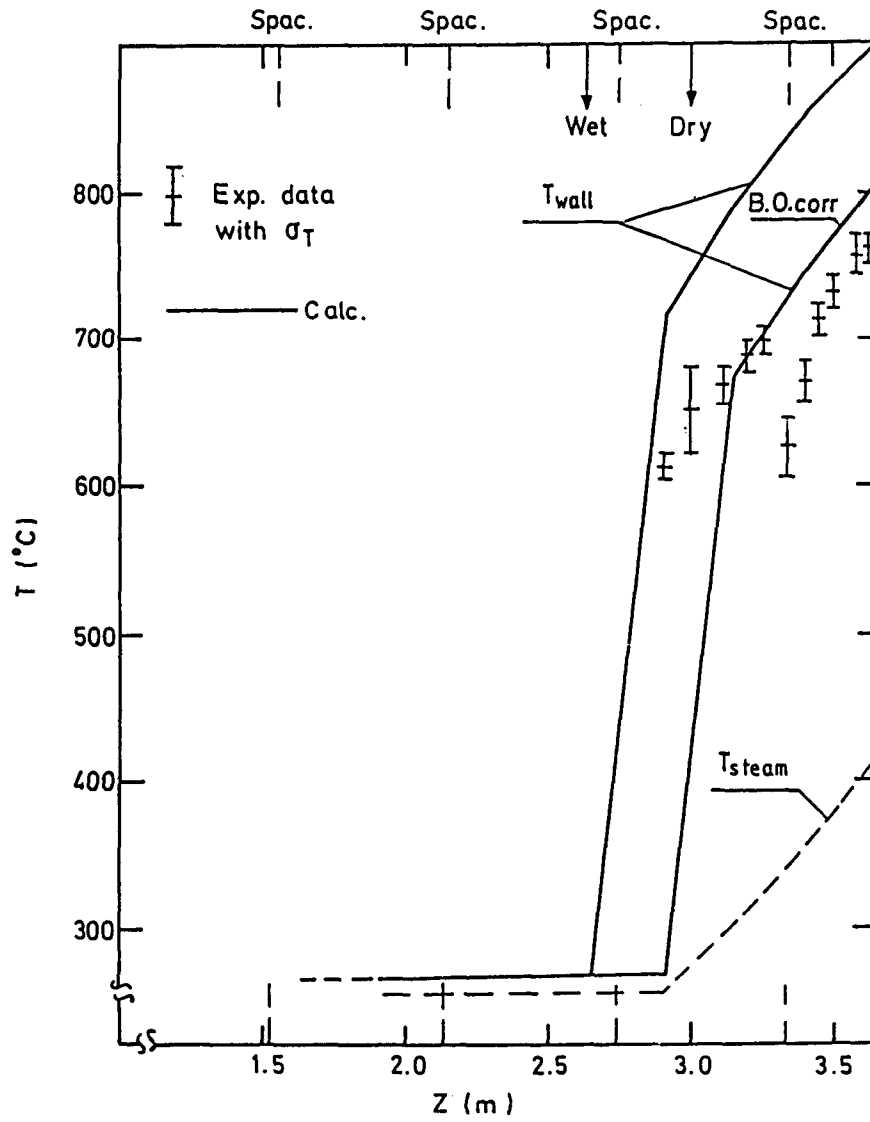
Fig. B2.36   ORNL   Case K

$P = 4.36$ MPa $\Delta T_{subc} = 45.8$ °C

$G = 226.$ kg/m^2 s $T_{sat.} = 255.8$ °C

$Q = 0.44$ MW/m^2
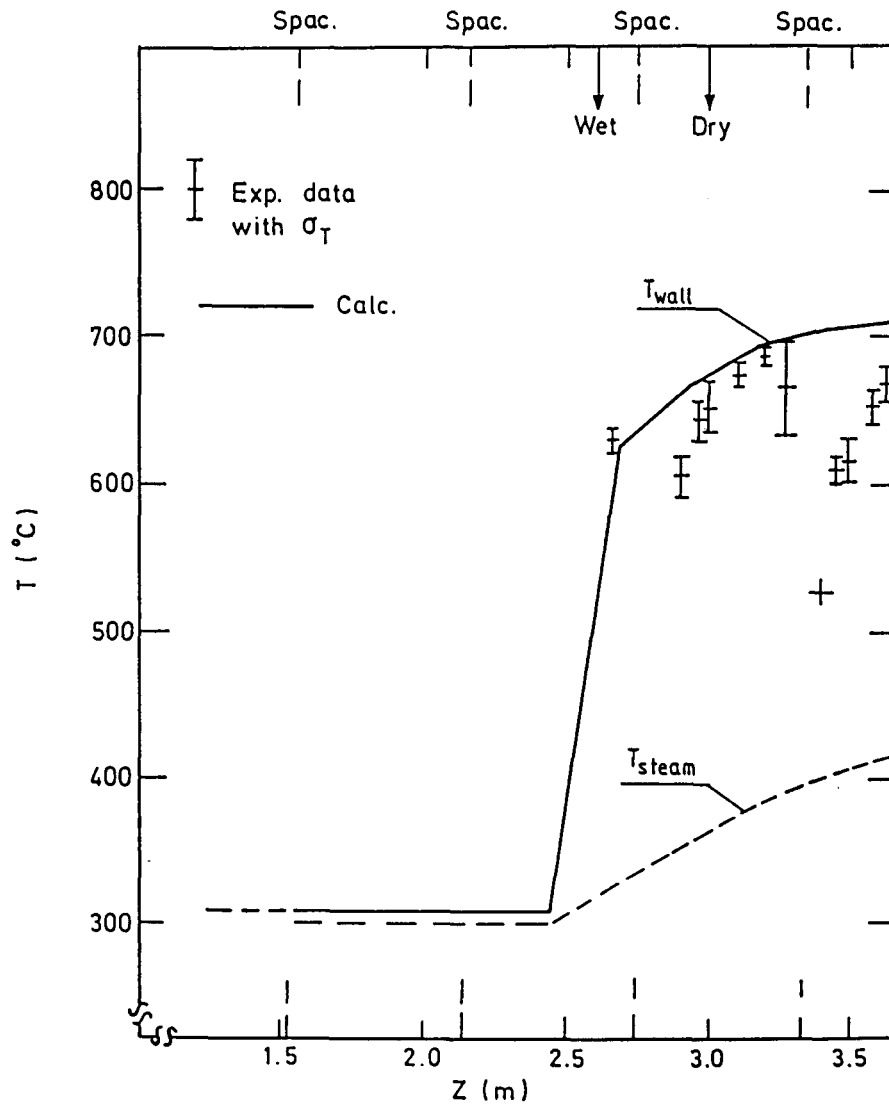
Fig. B2.37 ORNL Case N

P = 8.52 MPa ΔT_{subc} = 15. °C

G = 806. kg/m²s $T_{sat.}$ = 300 °C

Q = 0.94 MW/m²
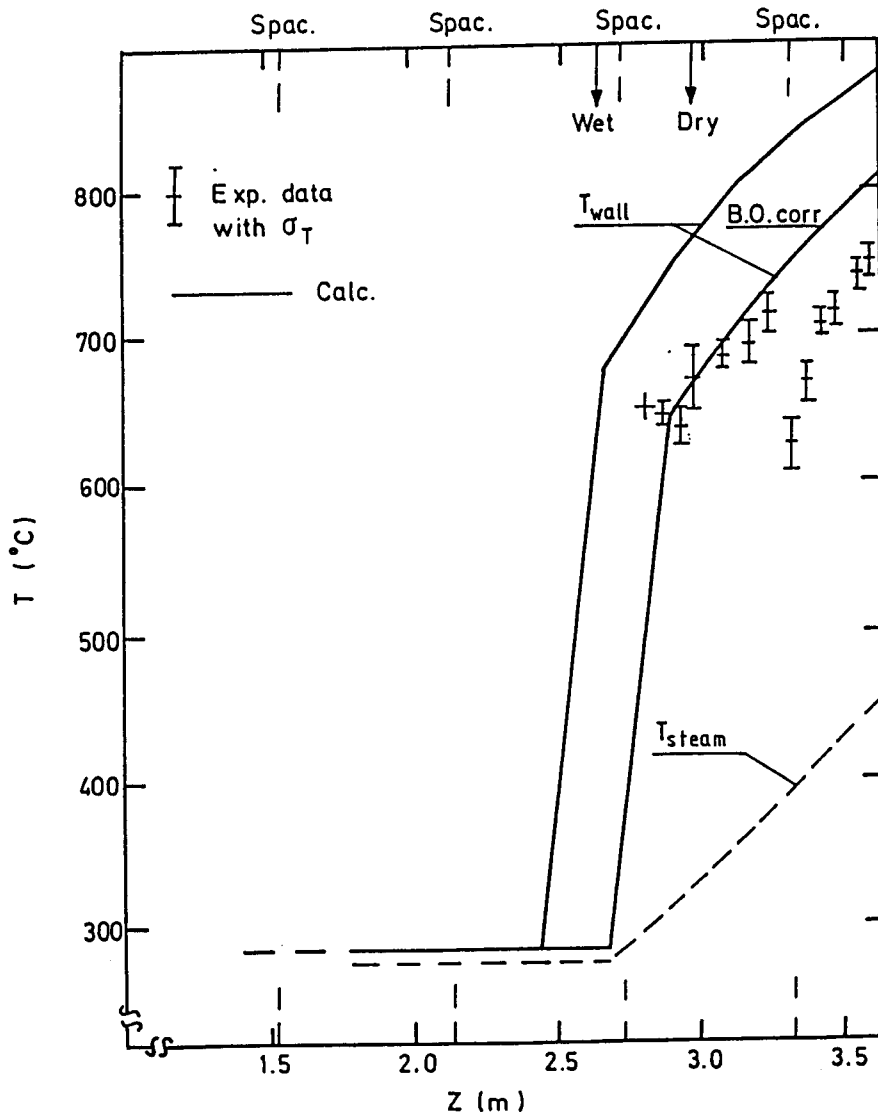
Fig. B2.38 ORNL Case O

$P = 5.98$ MPa $\quad$ $\Delta T_{subc} = 22.3$ °C

$G = 307.$ kg/m^2 s $\quad$ $T_{sat.} = 275.3$ °C

$Q = 0.53$ MW/m^2

Right downstream from a spacer the wall temperature drops due
to flow perturbations induced by it. No spacer effects were
accounted for in the calculations, however.

The locus of DO was predicted using the CISE4 CHF-correla-
tion. For some of the cases it was considered that the locus
of DO was too far upstream and these cases were recalculated
with the locus of the DO moved one node length downstream. These
new wall temperatures are indicated by "BO-corr" in the fig-
ures. The results clearly demonstrate the sensitivity of cal-
culated wall temperatures to the calculated locus of DO.

B3. Experiences using the computer programmes.

Numerical methods

The work performed in SÅK-5 project has mainly been concen-
trated on the calculation of steady state tests. For this pur-
pose the numerical method of RELAP5/MOD1 is a semi-implicit
one, which has the maximum time step of

$$\Delta t_{max} < \Delta z/u$$

where Δz is the node length and u is the velocity. In SÅK-5
work the maximum time step according to this criteria has been
in some cases less than 5 ms, which leads to excessive computing
time (~ 1000-2000 s). If a fully implicit numerical method
could be used, the steady state is obtained using a single
infinitely long time step. In that case the solution method
is iterative and the number of iteration cycles may be large,
but in spite of that the total computation time can be two
orders of magnitude less than it would be using RELAP5.

TRAC(PF1) utilizes a so-called two-step method, which avoids
the stability criteria. A similar method is also used in
RELAP5/MOD 2, which has not been used in this project. Although
the two-step method has no stability criteria, the solution
does not approach the steady state when the size of the time
step is increased. Thus steady state solutions have to be

obtained by transient calculation, which is more time con-
suming than the use of a fully implicit method. In order to
calculate the steady state in the test case, TRAC(PF1) re-
quired about 200-300 seconds computing time, while the fully
implicit method used in Finland consumed only 20-30 seconds.
A steady state version of NORA, called NORAS, consumed less
than 10 seconds, but the number of volumes was smaller (20
instead of 35). Furthermore, a direct comparison of the
execution times is not possible, because of different compu-
ters, but it seems that TRAC(PF1) consumed at least 10 times
more computing time than a fully implicit method, and RELAP/
MOD1 about ten times more than TRAC(PF1). The physical assump-
tions and spatial discretization methods have also been
different in different computer programmes. RELAP5/MOD1 u-
tilizes only one energy equations. However, this did not
cause any trouble in comparing the calculated results.

All the computer programmes have a conservative discretiza-
tion for mass and energy equations. TRAC and RELAP5 have a
non-conservative form of momentum equations. The results
depend somewhat on which form of the momentum equations is
used, but in the calculated cases the error was not signifi-
cant when the node size was 0.2 m. This is natural, because
all consistent numerical methods should have the same solut-
ion when the node size approaches zero. With a larger node
size, the difference between a conservative and non-conserva-
tive method may be more significant. In the present case
there were also more significant differences in the momentum
fluxes of the individual phases, but the difference in the
total momentum flux was small.

Constitutive equations

Heat transfer correlations are evaluated in a separate Appen-
dix; experiences with other constitutive models are shortly
described here. During the work it appeared that many cons-
titutive models were not only poorly tested, but they were
also different in different versions of the same computer

programme. An example is the interfacial drag correlation of RELAP5/MOD1-Cycle 19, which has been applied for the calculations in Finland and Sweden. The programme version used in Finland has a drag smoothing model, which caused very peculiar velocity profiles (see Fig. B3.1).

Another important constitutive model is the one used for interfacial heat transfer. These models are at present very simple and crude. In all cases the RELAP-programme predicted almost equilibrium conditions between the phases. The maximum temperature difference between the phases was always less than 1K and usually less than 0.1K (see Fig. B3.2). It can be concluded that RELAP5 behaves like an equilibrium computer programme except in the very early stages of flashing, which usually occurs only in rapid transients.

There have also been some difficulties in the application of constitutive equations. Usually the difficulties are caused by discontinuities in the set of correlation. In RELAP5 these discontinuities have been discovered in interfacial friction, wall friction and critical heat flux. These are described in the next chapter.

Difficulties in the application of correlations

The main difficulties in the application of any constitutive model are caused by discontinuities, when a correlation used is changed during the calculation. The discontinuities may prevent convergence of the numerical method and the calculated result is oscillatory. These oscillations also strongly affect the mass and energy balance and consequently the calculated result is unreliable.

In the present work the main difficulties have been caused by the models of interfacial and wall friction of RELAP5. An example is the interfacial friction coefficient depicted in Fig. B3.3. It can be seen that there is a discontinuous change in the friction coefficient when the void fraction equals 0.65. During the solution, when the void fraction is greater

than 0.65, the friction coefficient has a low value resulting
in a large velocity difference between the phases. This, in
turn, may cause a decrease in void fraction so that on the
next time step or iteration cycle the void fraction is less
than 0.65, which results in a large friction coefficient.
Hence, on the next cycle the velocity difference is again
small and the void fraction is greater than 0.65. Unless a
large amount of numerical damping is added, this oscillatory
cycle goes on forever. When a non-iterative numerical method is
used like the one of RELAP5, is used this damping can be ob-
tained only by the use very small timer steps, which are not
possible in practice.

Another example of numerical difficulties that arise is the
discontinous way wall friction is shared among the phases in
RELAP5.

It is obvious that a constitutive model should not include
computational discontinuities described above, because in
these cases the problem has either no solution at all, or the
solution is obtained only by an ultimately large computational
effort i.e. by using tiny time steps or a large number of
iterations. Because of this a modified wall friction package
has been developed, which has been used for the calculations
of Becker's test cases. In this package the partition of the
wall friction is performed so that the hysteresis phenomenon
is not possible. The results using the new package are nearly
the same as the results of the original package. The new
package results were close to the average of the oscillatory
results, when oscillations occurred in using the original
package. In all cases the total frictional pressure drop in
the channel was the same. Thus the smoothened wall friction
model didnot change the absolute values, but improved the
stability of the calculation.

B4. Comparison using separate programmes

B4.1 Critical heat flux
Due to the difficulties of making an assessment of different
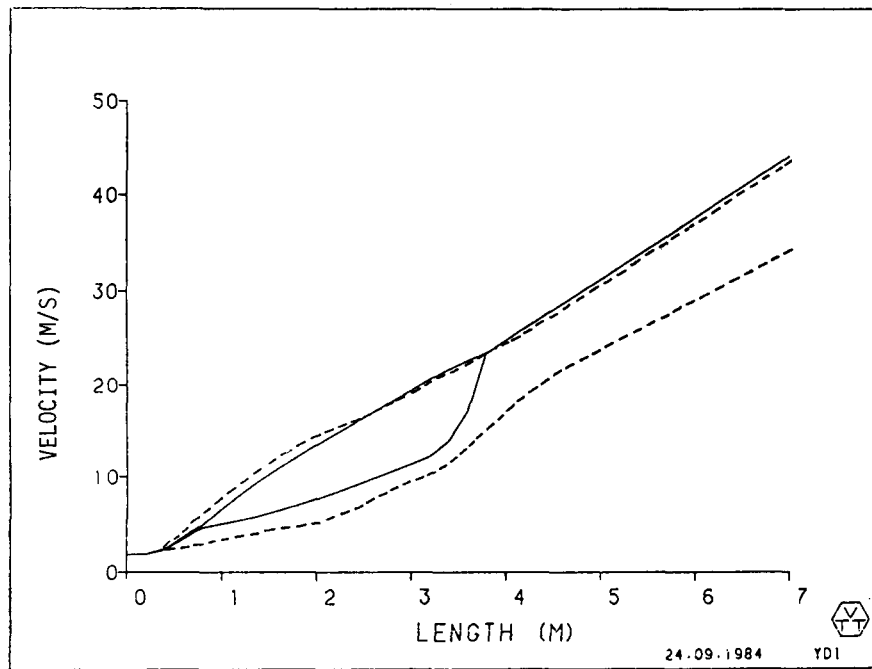
Fig.B3.1 Calculated velocity profiles in Becker's test case
no.1.____RELAP5/Mod1/CYCLE19 in Finland,
----RELAP5/Mod1/CYCLE19 in Sweden.
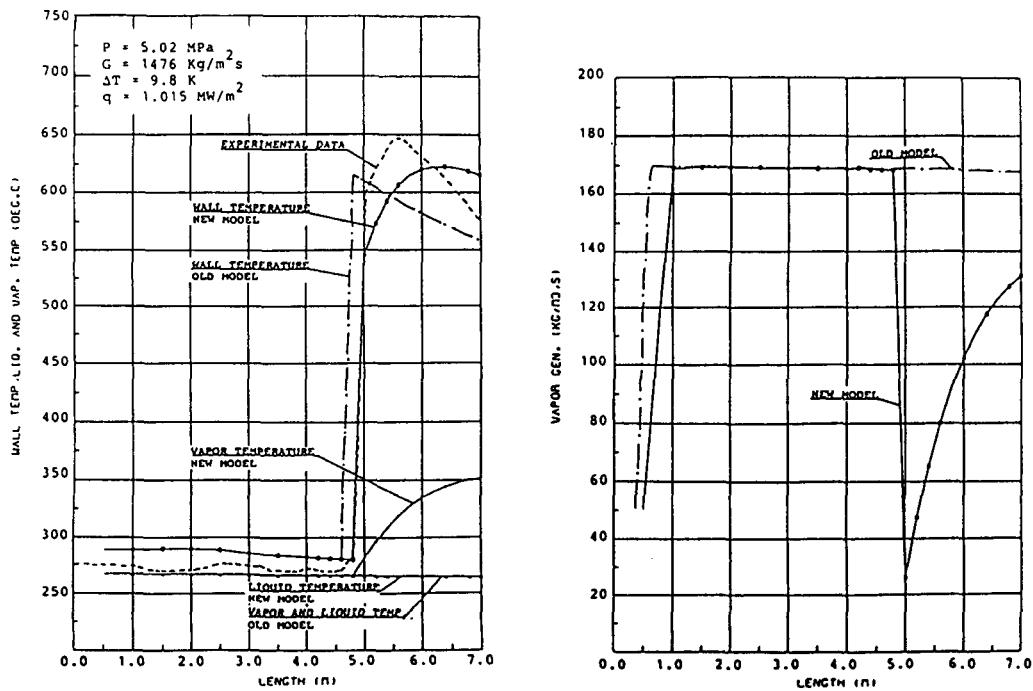
Fig. B3.2 Calculated temperatures and vapour generation rate
in Becker's test case No. 1.
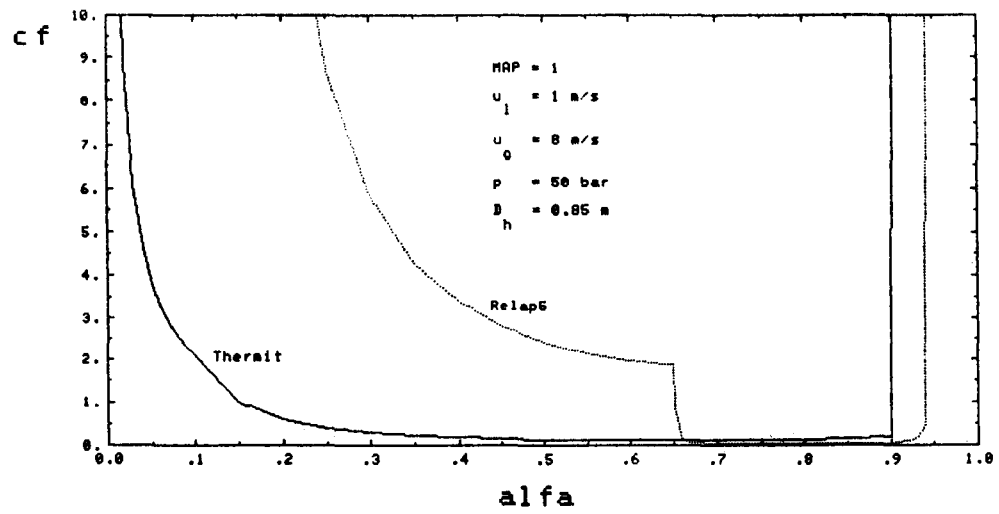
Fig.B3.3   Interfacial friction coefficient as a function of
void fraction.

CHF-correlations employing the thermohydraulic system program-
mes like RELAP5 and TRAC, a separate examination of this issue
was made. The assessment was performed as a separate part of
the SÄK-5 project and was conducted at the Royal Institute
of Technology in Stockholm. The result of this assessment is
reported in (73) and in what follows a short summary of the
work will be given. Also some additional efforts made during
the late phase of the project will be reviewed.

The assessment was limited to four different CHF-correlations
and was based on six full-scale steady-state rod bundle experi-
ments. The correlations included in the assessment were:

Barnett   (74)
Becker   (75)
Biasi   (5)
CISE-4   (76)

The Biasi and CISE-4 correlations were originally developed
for round tubes and thus the performance in rod bundle geo-
metries could be questionable. However, as they are utilized
in several of the commonly used transient computer programmes,
for instance TRAC(PF1) and RELAP5/MOD1, it was decided also to
include those correlations in the assessment. The experimental
data used for this assessment were obtained in a 64-rod bundle
(Desirello et al 77), 81-rod bundle (Pimputkar et al 78), 36-
rod bundle (Nilsson 79 and Nylund 80, 81), and 37-rod bundle
(Bowditch and Smyth 82). These experiments included axially
uniform as well as axially variable heat flux distributions.

The dryout predictions were carried out employing either the
total power hypothesis or the local conditions hypothesis.
In the total power hypothesis the total channel dryout power
was predicted assuming uniform axial heat flux distribution
and compared to the measured power. Thus this method did not
yield any information about the axial location of dryout. In
the local conditions hypothesis, proposed by Becker in 1969
(83), the dryout is assumed to be dependent only on local flow
parameters at the locus of dryout. The principle of this

method is demonstrated in Fig B4.1.1 where the experimental
heat flux is plotted versus the quality along the channel. In
the figure an arbitrary dryout correlation is also included
and the heat balance is represented by a straight line. The
locus of dryout is determined by drawing a family of heat
balance lines for different axial locations and then selecting
the line yielding the minimum value of the ratio $(q/A)_{BOPRE}$/
$(q/A)_{BOEXP}$.

Because of the difficulty of defining a proper boiling length
in transient and LOCA situations it is obvious that the
method employing the local conditions hypothesis has to be
adopted for the CHF predictions in these type of transients.
Thus the following will deal only with the results obtained
when using the local conditions hypothesis.

A total number of 269 runs were obtained in the utilized expe-
rimental studies mentioned above covering the following para-
meter ranges:

Pressure	3.0 - 9.0 MPa
Mass Flux	200 - 2400 kg/m^2s
Inlet Subcooling	12 - 286 kJ/kg
Dryout Heat Flux	0.23 - 1.49 MW/m^2
Dryout Steam Quality	0.18 - 0.805

143 of the measurements were obtained with axially non-uniform-
ly heated test sections while the remaining 126 measurements
had a uniform axial flux distribution.

Only the Becker and the Biasi correlations covered all the uti-
lized experimetal data. Concerning the CISE-4 correlation the
results at pressure 3.0 MPa were outside the range of the cor-
relation. Finally the Barnett correlation was valid only for
pressure 7.0 MPa.

The result of the comparison between measurements and predic-

tions can be illustrated by Figs. B4.1.2 to B4.1.5 showing the measured versus the predicted dryout power for the 64- and 81- rod bundles. The trends for all of the experiments were similar; the Biasi and CISE 4 correlations generally over-predicted the data considerably while the Barnett and the Becker correlations yielded rather good predictions especially for the square lattice 81, 64 and 36-rod bundles.

A summary of the results obtained with the local condition hypothesis is shown in Table B4.1.I. The best predictions were obtained with the Becker correlation yielding a RMS error of 9.7% including all the runs of the 6 experimental studies. The Biasi and CISE-4 correlations were in poor agreement with the experimental data; the reason for this is probably that these correlations were developed for predictions of dryout in circular tubes.

Also some selected experiments from the OF-64 experimental dryout series were analysed (84). This test series was conducted by ASEA-ATOM, Sweden, in 1969 and is reported in (85). The test section was designed as a full-scale simulation of an Oskarskamn I fuel assembly and consisted of 64 heated rods. The internal radial power distribution was symmetrical with a peaking factor of 1.24 while the axial power distribution was peaked towards the outlet with a peaking factor of 1.55. The tests were performed with pressures ranging from 4.8 to 8.7 MPa, mass fluxes from 400 to 2000 kg/m^2s, and bundle powers from 5.1 to 8.6 MW. Seven dryout tests were selected for separate examination and the conditions for these tests were:

Test No	Pressure (MPa)	Inlet Subcooling (K)	Mass Flux (kg/m^2s)	Power (kW)
703007	6.71	8.7	498	5957
703073	6.82	7.8	971	7683
703015	6.67	9.4	1168	7899
703075	6.72	9.5	1336	8192
703077	6.82	9.0	1535	8594
703087	8.64	9.2	1382	6843
703043	4.79	2.1	789	7693

In these analyses the Becker and for the 7 MPa cases also the Barnett correlations revealed the best agreement, while the Biasi and the CISE-4 correlations were in fairly poor agreement with data, i.e. the results were consistent with the findings in the assessment reported above. The results obtained with the Becker correlation is illustrated in Fig. B4.1.6, indicating a very good agreement although somewhat conservative.

Finally, some predictions of the locus of dryout for the above-mentioned OF-64 cases were carried out by means of Becker and Biasi correlations and compared with the measured ones (86). The conclusions from these calculations were that the Becker correlation revealed a very good correspondence between predicted and measured locus of dryout for mass fluxes above 1000 kg/m^2 s, the errors being within the measurement accuracy. For mass fluxes below 1000 kg/m^{2}s the correspondence in some cases was not quite that good, being on the conservative side though (the predicted locations were found to be upstream of the measured ones). It should also be mentioned that the Biasi CHF correlations did not predict dryout in any of the cases, thus being very non-conservative.

B4.2 Transition boiling.

The literature search resulted in the selection of 5 correlations:
1. Chen correlation (29),
2. Correlation by Tong & Young (31),
3. Correlation by Bjornard & Griffith (33),
4. EPRI correlation (87),
5. Correlation by Hsu (32).
The correlations 1, 2, 3 and 5 are shown in Table A3.I.

In 1 and partly also in 2 physical phenomena have been considered to a certain degree. The other correlations may be

	Barnett		Becker		Biasi		CISE-4	
	No. of Runs	RMS Error	No. of Runs	RMS Error	No. of Runs	RMS Error	No. of Runs	RMS Error
64-rod bundle,ref.77	18	6.5	18	11.5	18	30.7	18	21.5
81-rod bundle,ref.78	24	5.5	24	7.0	24	26.9	24	18.2
36-rod bundle,ref.79	11	15.3	18	3.3	18	20.9	16	7.9
36-rod bundle,ref.80	11	12.2	38	10.5	38	30.3	32	23.2
36-rod bundle,ref.81	26	8.4	83	12.5	83	31.3	71	22.6
37-rod bundle,ref.82	69	11.7	88	7.0	88	34.2	69	23.2
All Bundles	159	10.3	269	9.7	269	31.2	230	21.6

TABLE B4.1.I.   RMS-ERRORS OBTAINED WITH THE LOCAL

HYPOTHESIS

Y-axis: HEAT FLUX, (q/A)
X-axis: STEAM QUALITY, x

CORRELATION   HEAT BALANCE

$(x_{BO}, (q/A)_{BO})_{PRE}$
$(x_{BO}, (q/A)_{BO})_{EXP}$
$(x_{BO}, (q/A)_{AV})_{EXP}$

RADIAL HEAT FLUX DISTRIBUTION

HIGHEST RATED ROD
— — — — — —
ROD BUNDLE AVERAGE
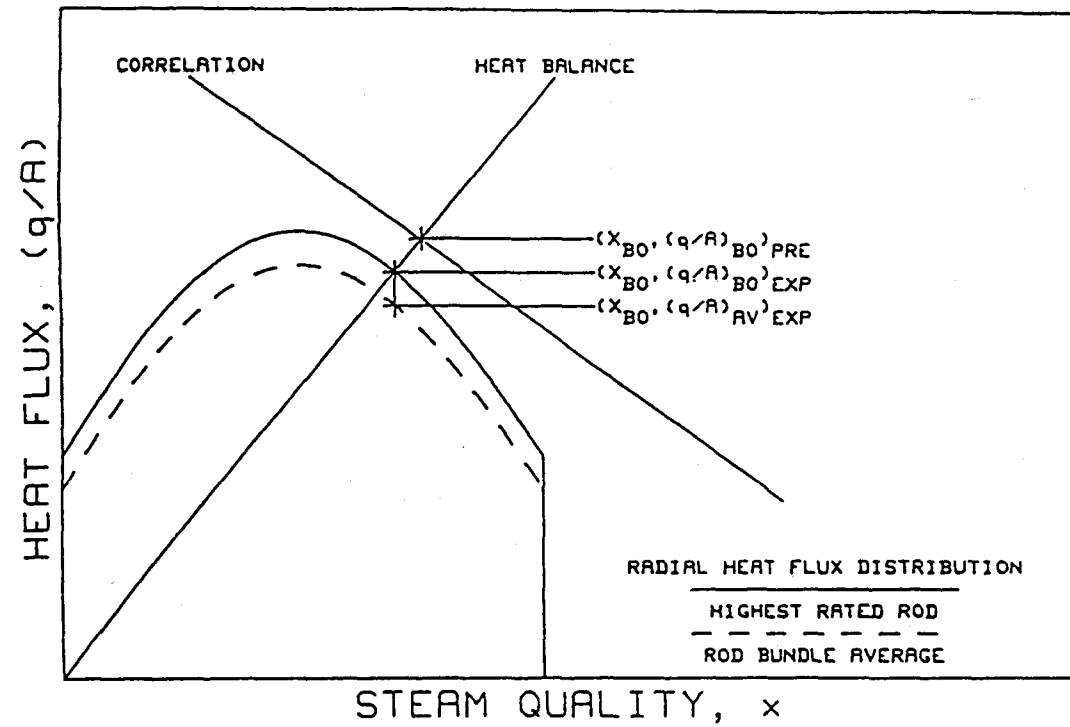
FIGURE B4.1.1 LOCAL CONDITION HYPOTHESIS
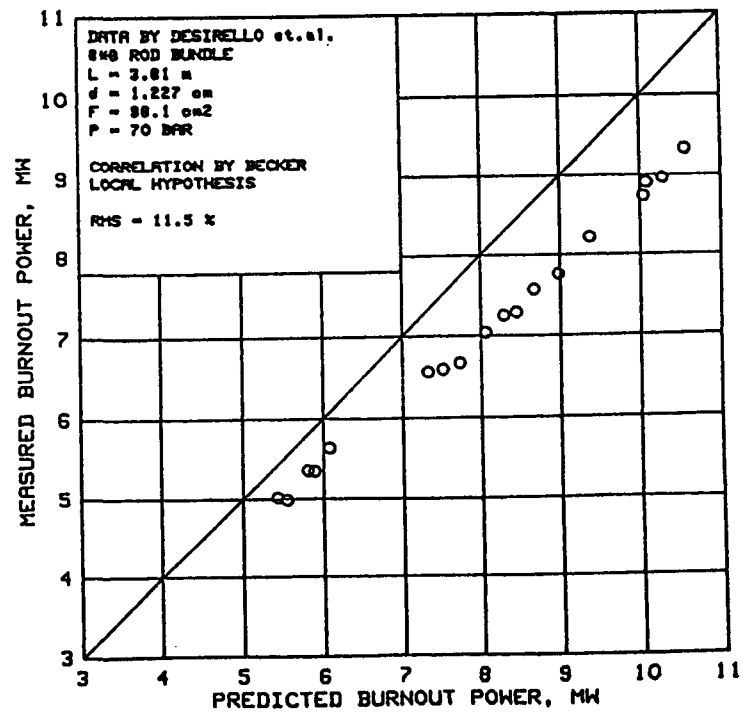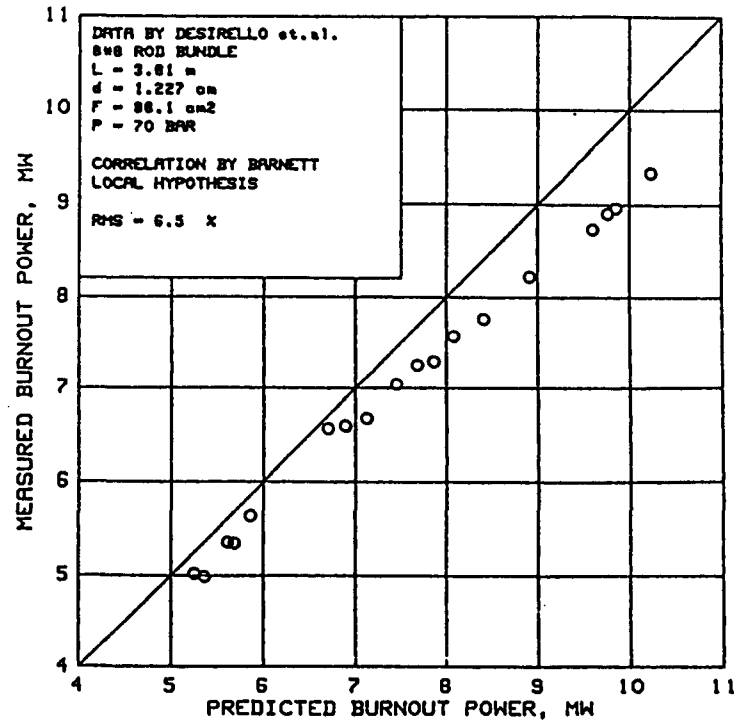
FIGURE B4.1.2 COMPARISON BETWEEN MEASURED
AND PREDICTED BURNOUT POWER
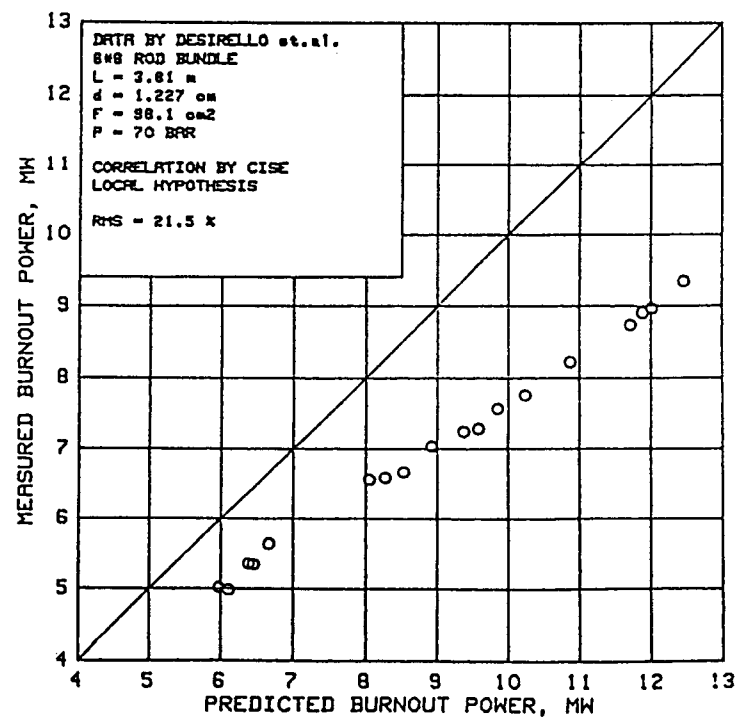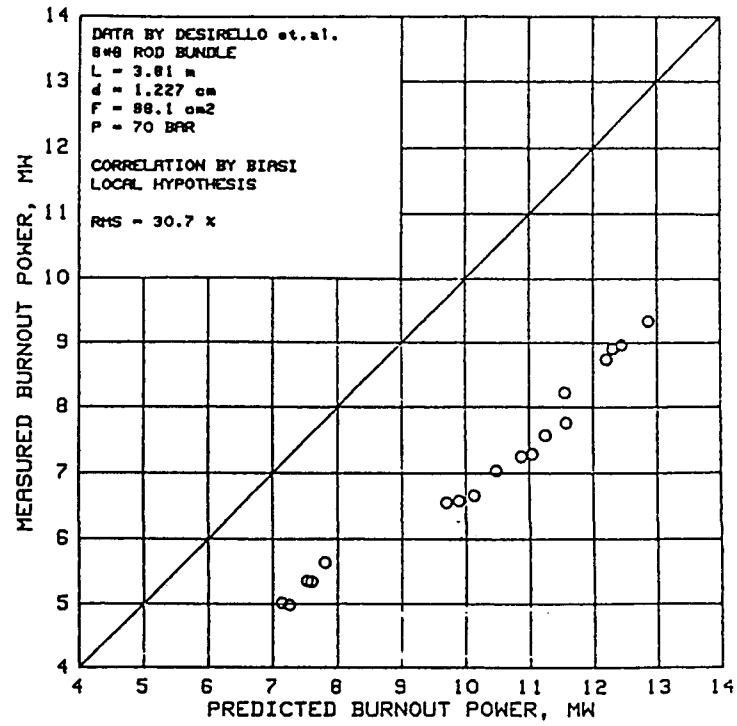
FIGURE B4.1.3 COMPARISON BETWEEN MEASURED
AND PREDICTED BURNOUT POWER
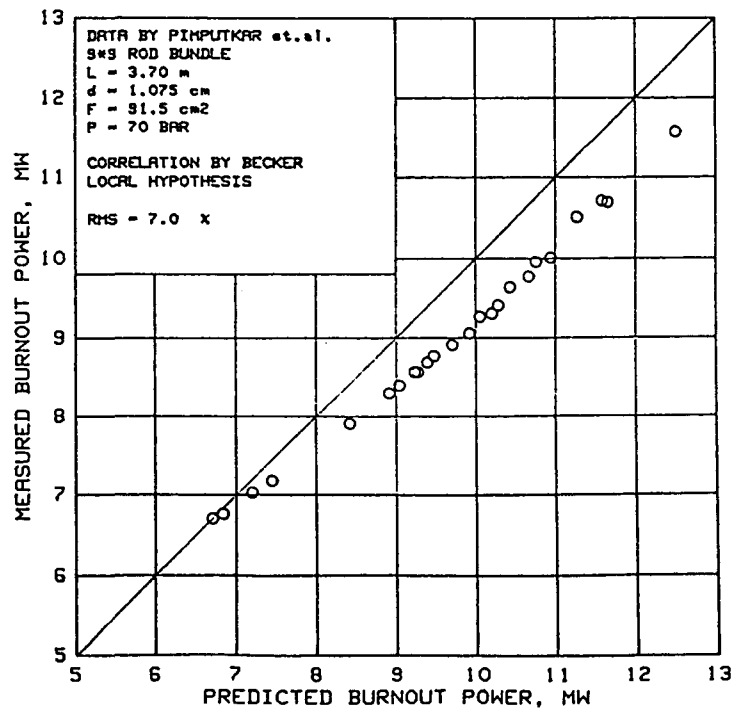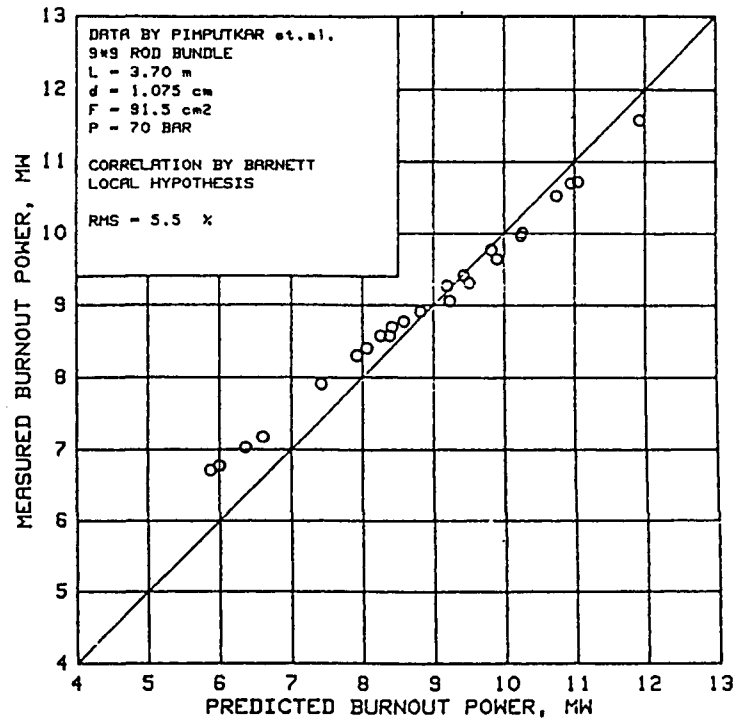
FIGURE B4.1.4   COMPARISON BETWEEN MEASURED
                AND PREDICTED BURNOUT POWER
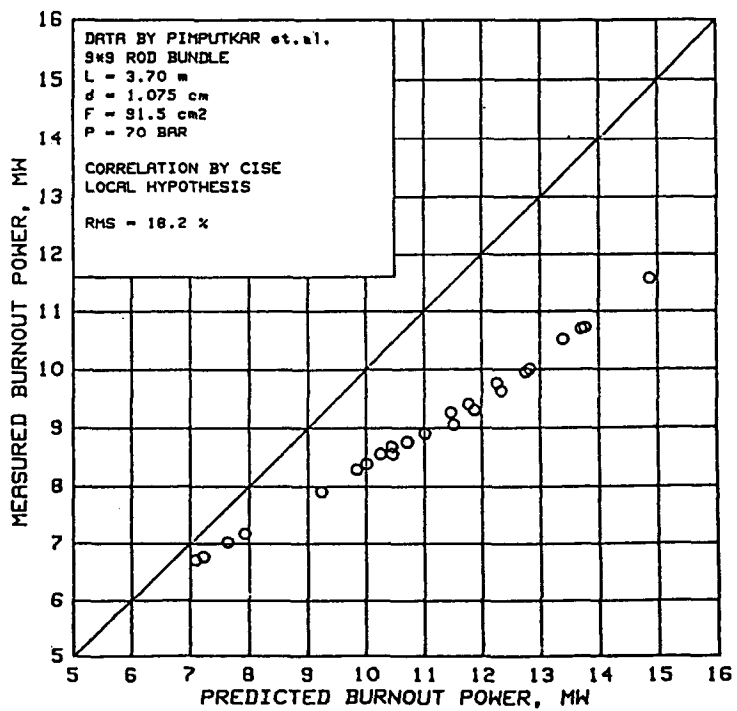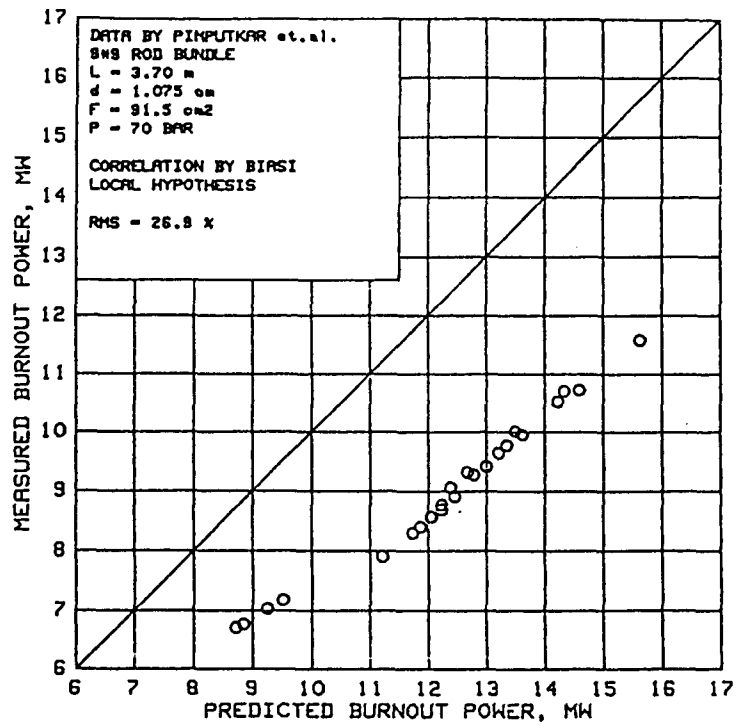
FIGURE B4.1.5 COMPARISON BETWEEN MEASURED
AND PREDICTED BURNOUT POWER
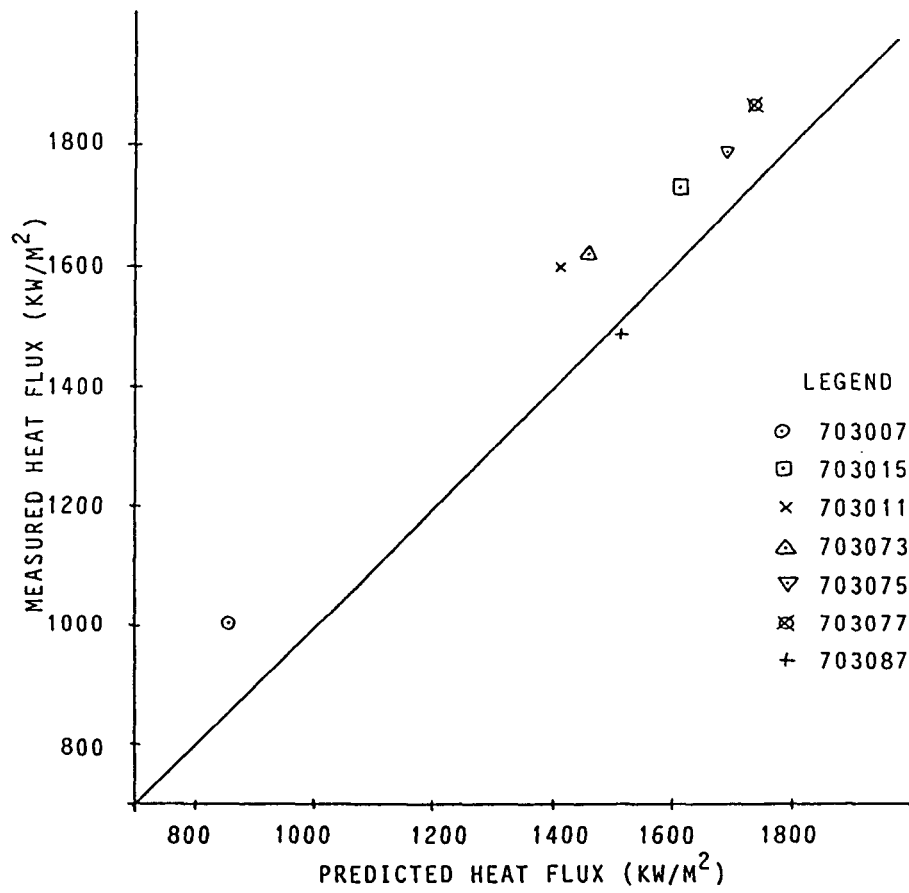
Figure B4.1.6   OF - 64. Comparison between measured
and predicted dry-out heat flux.

described as empirical correlations. All correlations are of the two-term type.

A detailed description of the correlations is given in (26). A literature search was made in order to find relevant temperature controlled test data. Very few references were found. The best and most relevant experimental data were those conducted by Prof. J. Weisman at University of Cincinnati and published by Electric Power Research Institute (EPRI),(87).

The temperature controlled surface is ensured by heating the boiling water by hot flowing mercury. The water flows upward in an annulus and the mercury flowing downward in a center tube. Measurement of wall and mercury temperatures at several elevations allows the heat transfer to be determined.

The pressures are from 1 to 4 bar. Mass fluxes used in the evaluation are from 10 to 36 kg/m^2/sec and steam qualities from 0.02 to 0.54.

A separate computer programme was written to evaluate the 5 correlations with the stated experimental data as input.

A listing of the computer programme is reproduced in Appendix B in ref. (26). The final results from the evaluation are reproduced in Appendix A of the same reference.

The Chen correlation is based on experimental data from 8 references with pressures ranging from 4 to 195 bar, mass fluxes from 16 to 3000 kg/m^2/sec, and equilibrium qualities from 0.5 to 1.7.

For some parameters the evaluation is the outside the previous range.

The first evaluations gave large deviations from the EPRI results. Two important parameters in the correlation have been examined: the thermodynamic nonequilibrium and the liquid contact area fraction (the decay factor).

Both are empirically determined and based on the experimental data mentioned above.

The vapour may be superheated, i.e. part of the heat from the surface has been used to superheat the vapour instead of evaporating the droplets. The actual vapour quality, XA, is less than the equilibrium quality, XE.

The heat balance gives the following relation between XA and XE:

$$\frac{XA}{XE} = \frac{H_{fg}}{H_{fg} + C_{pv} (T_v - T_{SAT})}$$

There are two unknowns in this equation XA and T_v, the superheated vapour temperature.

Chen defined a parameter B(P):

$$\frac{XA}{XE} = 1.0 - B(P) \cdot \frac{T_v - T_{SAT}}{T_W - T_v}$$

and determined B(P) from the experimental data:

$$B(P) = \frac{0.26}{1.15 - (P/P_c)^{0.65}}$$

P is the pressure and P_c is the critical pressure.

B(P) approaches 0.226 when P approaches 0.0, where B(P) should approach 0.0. Some of the experimental data on which B(P) is determined make it plausible to infer that B(P) is 0.0 when P is 0.0. Based only on these data B(P) may be correlated as:

$$B(P) = 8.1 \cdot 10^{-2} + 2.0 \cdot (P/P_c) - 4.0 \ (P/PC)^2$$

for pressures less than 50 bar (Figure B4.2.1). The result of this correction is that there will be vapour at lower pressures as the EPRI data will be superheated earlier than after the Chen results, in agreement with EPRI data. The deviation has however, to be examined in more detail.

Chen used his data bank to determine the decay factor using the relation:

$$FL = \frac{q_T - q_{VC}}{q_{LC} - q_{VC}}$$

The decay factor was correlated with the equation:

$$FL = \exp(-\lambda \cdot (T_w - T_{SAT})^n),$$

where λ is a function of void and mass flux.

Chen determined the exponent n to 0.5. This gave too low values of the heat transfer compared with the EPRI result, however.

The results from the calculations based on the EPRI data were therefore substituted in the relation for the decay factor; FL and the exponent n were determined. The functional relationship for λ was retained. Plot of the exponent n is shown in Fig. B4.2.2. The data have been correlated by two straight lines. It cannot be excluded that the strong increase in the exponent near the critical point is due to an inaccurate determination of the experimental total heat flux near this point cf. Figs. B4.2.3-B4.2.7. Only data above about 40 degrees in the temperature difference, $T_w - T_{SAT}$, should have been taken into into account.

As mentioned above, all experimental data used by Chen et al. are above 4 bar and most of them are at high pressure. This may be one explanation of the small exponent.

Chen et al. do not take interfacial heat transfer into account. An explanation may be that the B(P)-values after Chen's equation imply that the vapour will not be superheated.

Tong & Young published their correlation in 1974. In contradiction to Chen et al. they use the nucleate boiling heat flux at CHF as the boiling term, and a modified single-phase heat transfer correlation (Dittus-Boelter) for the convection term (see Table A3.I no.2).
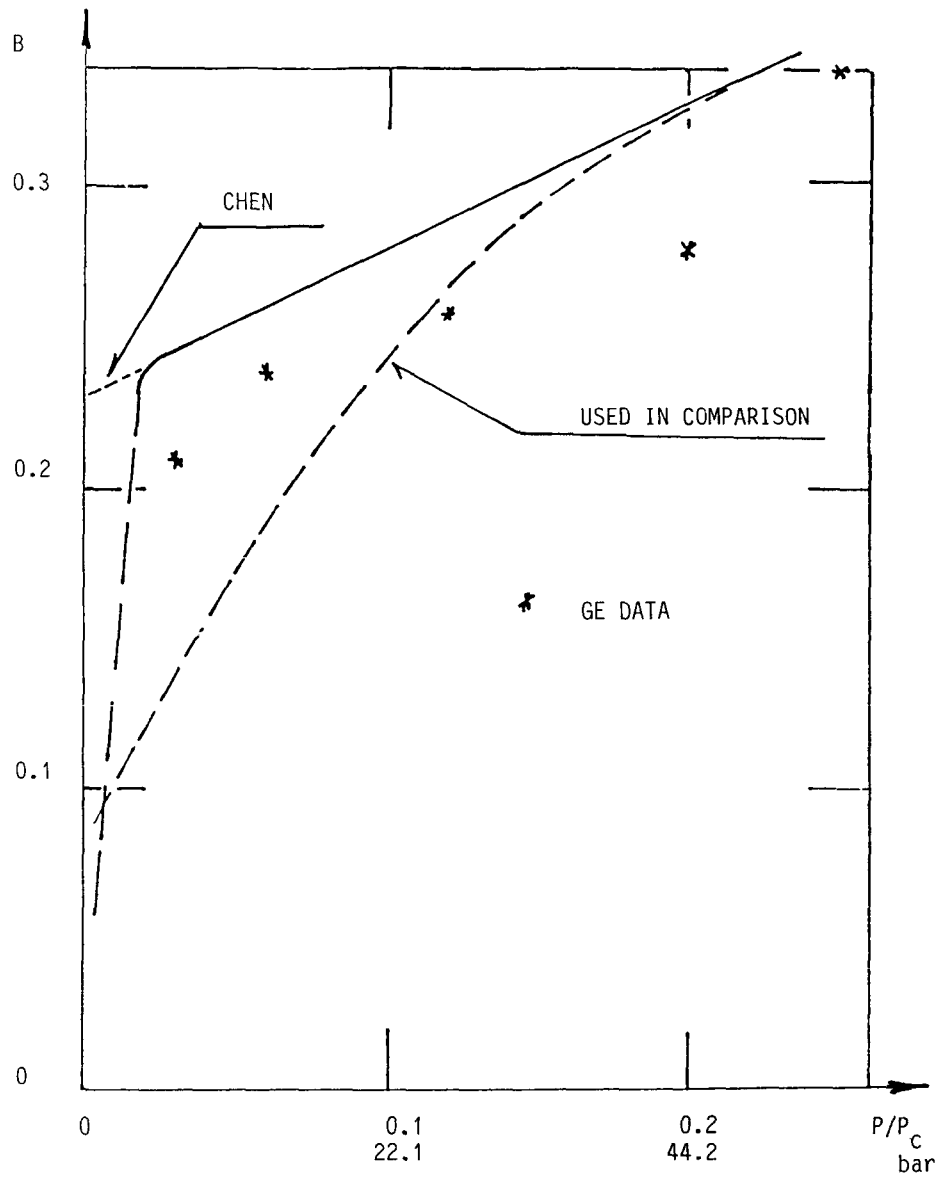
FIGURE B4.2.1
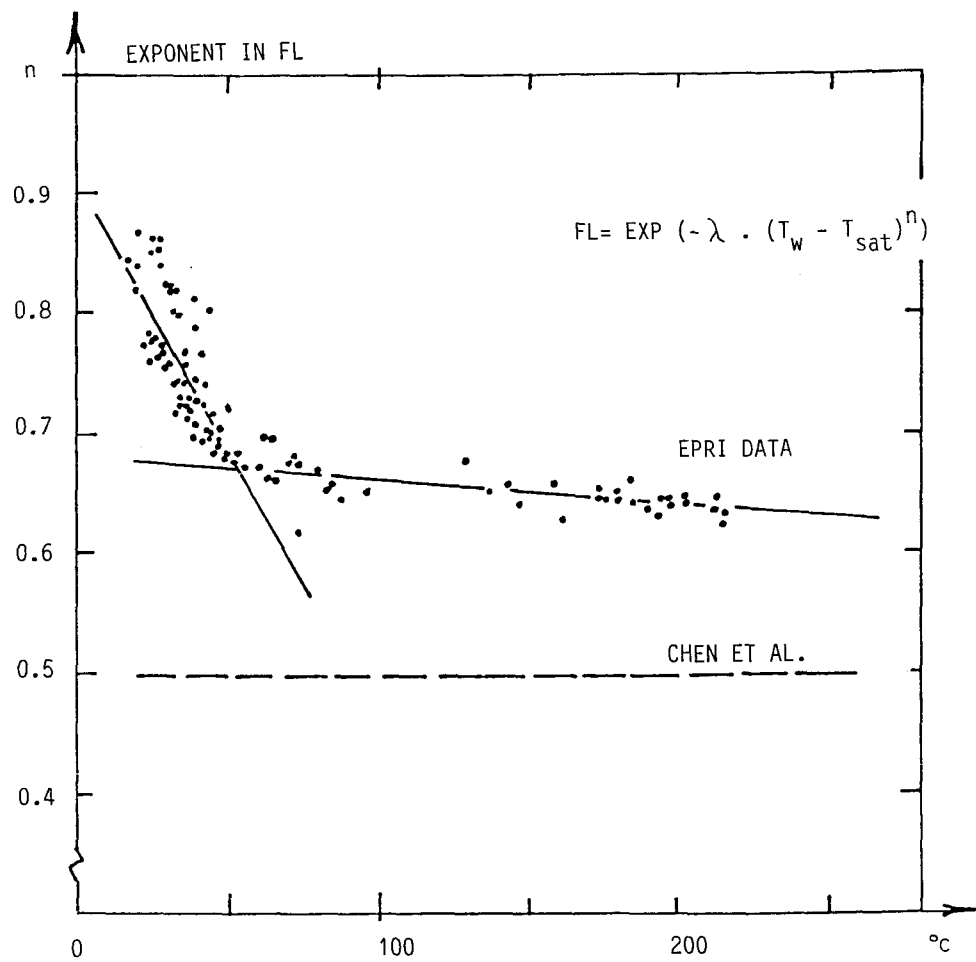
FIGURE B4.2.2

Tong & Young have used high pressure data to determine the decay factor. The use of their equation for the decay factor on the EPRI data gives values that are too high i.e. it is the boiling term, which is dominant and the correlation will be in agreement only at low temperature differences near the CHF.

The Tong & Young results are not shown in the figures.

The correlation by Bjornard & Griffith (see Table A3. I no.5) is a purely empirical two-term correlation. The two terms are defined as the limits between which transition boiling heat transfer may exist i.e. the critical heat flux and corresponding critical temperature, T_{CHF}, and the minimum film boiling heat flux and corresponding temperature, T_{MFB}.

The results of the examination are plotted the Figs. B4.2.3 - B4.2.7.

The EPRI correlation is considered because it is developed from their own experimental results as basis and may therefore give a first indication of how good are the results.

The above-mentioned correlations are all primarily evaluated in the vapour-continuous flow region.

The Hsu correlation is developed from subcooled FLECHT data, i.e. in the liquid-continuous flow region. The results using EPRI data show a heat transfer that is too high, as may be expected.

The comparison shows that the description of dispersed flow with droplets discretely distributed through the continuous vapour phase and the deposition motion of the droplets toward the wall is of fundamental importance for the heat transfer not only in the transition-boiling region, but also partly in the film-boiling region.

The dividing points between the two regions is the minimum heat

flux, which just represents the point of prevailing droplet wet collision heat transfer, over heat transferred to the vapour by convection and droplets entering the thermal boundary layer withour wetting the surface ("dry" collisions), and represents the point of incipient rewetting in emergency core cooling.

The heat transfer using a droplet deposition model may be divided into, two main questions:

1. How much heat can be carried away every time a droplet of a certain size impinges and wet the wall?
2. How many droplets per unit time of what size will penetrate the thermal boundary layer and wet the wall?

Chen et al. inferred a droplet diameter and determined the heat carried away by "wet" collisions, but did not take "dry" collisions into account. Nor did they consider the phenomena under point 2, but determined their liquid contact area fraction, the decay factor from the data base they used.

Tong & Young determined their decay factor as covering both points 1 and 2.

None of the correlations are phenomenological in the real sense of the word.

It is obvious that even some effort has been made to describe some of the important phenomena, it may be concluded from these comparisons that the correlations examined in the vapour continuous flow are valid only within the data base from which they are developed, i.e. they must still be considered as statistical correlations.

TRANSITION BOILING HEAT TRANSFER

WATT/m²   SURFACE HEAT FLUX

EXPERIMENTAL RESULTS
MODIFIED CHEN
TRAC - PF1 (BJORNARD)
EPRI

PRESSURE	1.7 - 1.8 bar
MASS FLUX	10.66 kg/m /sec
QUALITY	0.05 - 0.54

THALL - TSAT   °C

FIGURE B4.2.3

FIGURE B4.2.4

TRANSITION BOILING HEAT TRANSFER

EPRI TEST DATA
SERIE 500
250184

SURFACE HEAT FLUX

EXPERIMENTAL RESULTS
MODIFIED CHEN
TRAC - PF1 (BJORNARD)

PRESSURE	1.5 - 1.7 bar
MASS FLUX	20.22 kg/m /sec
QUALITY	0.02 - 0.27

FIGURE B4.2.5

TRANSITION BOILING HEAT TRANSFER

Legend:
- ⊙ EXPERIMENTAL RESULTS
- + MODIFIED CHEN
- △ TRAC – TF1 (BJORNARD)
- ⊡ EPRI

PRESSURE	1.6 – 2.1
MASS FLUX	27.58 kg/m /sec
QUALITY	0.03 – 0.23

Nr. 2002
AGP
Lin × Log
Modul 8333

Figure B4.2.6 — Transition Boiling Heat Transfer

EXPERIMENTAL RESULTS
MODIFIED CHEN
TRAC – PF1 (BJORNARD)
EPRI

PRESSURE   1.6 – 1.7 bar.
MASS FLUX   36.72 kg/m²/sec.
quality   0.02 – 0.17

FIGURE B4.2.7

PRESSURE   3.6 bar
MASS FLUX   7.48 kg/m²/sec
QUALITY   0.17 - 0.95

EXPERIMENTAL RESULTS
MODIFIED CHEN
TRAC - PF1 (BJORNARD)
EPRI

APPENDIX C.   DISPERSED FLOW

C1. Droplet Generation

Droplets are generated partly at all points of the water-vapour interface in pre-CHF regions due to entrainment and partly by sputtering in transition boiling in the post-CHF region.

The droplet generation by entrainment may be postulated to take place in a number of different ways governed by hydrodynamic- and surface tension forces. (88,10)

Fig. C1.1 shows the various mechanisms.

In the first type the droplets are sheared off from the wave crests of large-amplitude roll waves. The interfacial friction deforms the interface against the retaining force of liquid surface tension.

In the second type the droplets are generated by undercutting the liquid flow.

In the third type the droplet generation is related to bubbles rising to a free surface of liquid and bursting. When the bubble reaches the interface, a thin liquid film forms at the top of the bubble (Fig. C1.1. type 3 at left). As the liquid is drained from the film it may rupture resulting in a large number of entrained small droplets. (Fig. C1.1, type 3 at center).

A less numerous population of large droplets may be formed by the surging flow of liquid into the depression left after the bubble has burst. A spike-like filament rises at the center of the crater which is then disintegrated into droplets. (Fig. C1.1, type 3 at right).
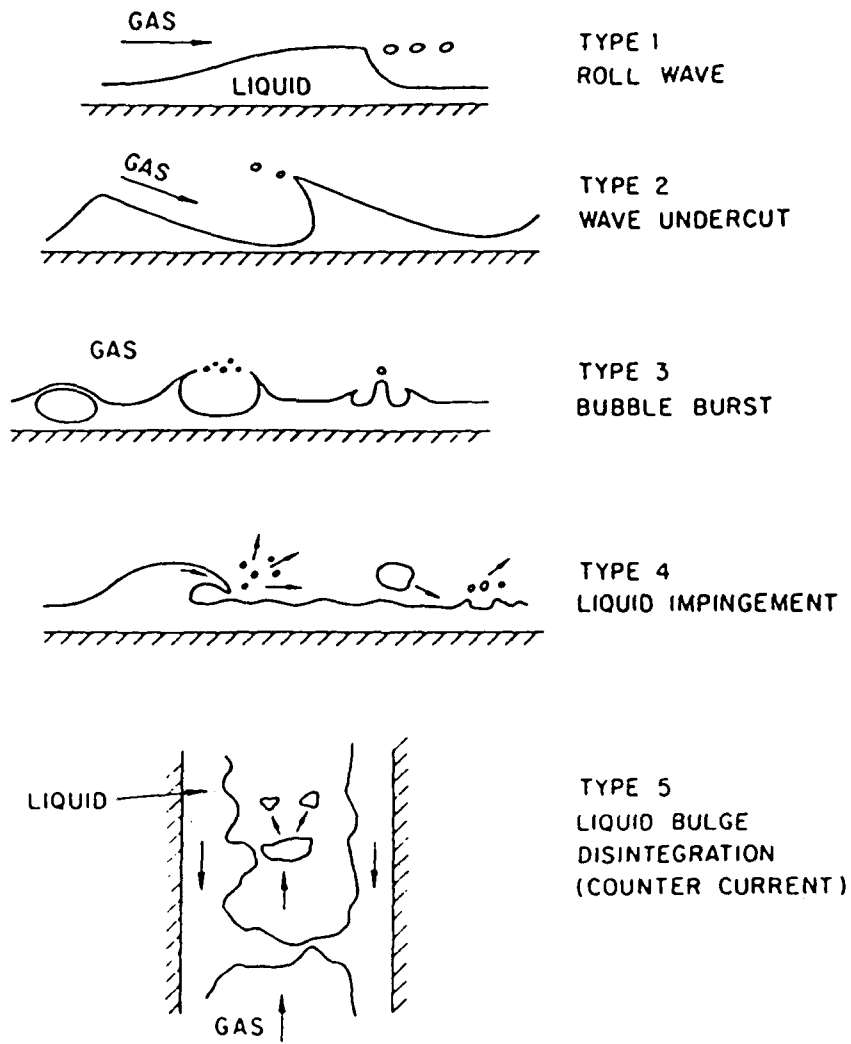
FIGURE C1.1   Droplet generation by
             entrainment (88).

In the fourth type the impingment of liquid mass or droplets may produce new droplets.

In counter-current flow the last type may occur as a result of flooding. Large amplitude waves may be separated from the liquid film to form a liquid bridge. This may disintegrate into several droplets.

Numerous small droplets are generated in convection with the quenching of the surface during the emergency cooling of the fuel rods. The quenching area is the region on the cladding surface where initial continuous contact between cladding surface and liquid is established i.e. the transition boiling region before the return to nucleate boiling.

In post-CHF regions and in vapour-continous flow further droplet generation can occur only through further breakup of larger droplets to smaller ones due to hydrodynamic forces or impingement of the droplets on a hot surface with high velocity and no rewetting.

Droplets Size.

The upper size limit of the droplet is given by the critical Weber number:

$$We_c = \frac{\rho_g \cdot d \cdot (u_g - u_\ell)^2}{\sigma}$$

A maximum stable droplet size is given by a critical Weber number of 12 - 13 (89). A value of 6.5 may be suggested to represent an average droplet size (10).

Droplet break up by impingment on a hot surface with a subsequently high velocity has been examined experimentally. The droplets will break up into a number of smaller droplets depending on the perpendicuar velocity of the droplet at the time of impingment.

The process is correlated in terms of Weber number:

$$We_p = \frac{\rho_\ell \cdot u_p^2 \cdot d}{\sigma}$$

with following classification

$$We_p \leq 30 \quad \text{no break up}$$
$$30 < We_p \leq 80 \quad \text{break up into a few large fragments}$$
$$We_p > 80 \quad \text{break up into smaller fragments.}$$

It should be noted that most experiments have been carried out with flat plates with surfaces significantly larger than the incoming droplets.

Experiments show that droplet populations can be divided into two separate groups: a population of small droplets with diameters from 10 μ to 140 μ with a maximum number at 50 - 60 μ (90), and a population of large droplets with diameter from 300 μ to 2000 μ with a maximum number at about 800 μ (90,91).

The size and also the number distribution in the axial direction depends primarily on the evaporation, i.e. interfacial heat transfer. Coagulation and further break up due to grid spacers in the fuel element and other channel restriction may also play a role.

The small droplets have a larger surface-to-volume ratio than large droplets i.e. the lifetime history is shorter for small droplets, than for the larger droplets. The energy absorption rate from these small droplets is very high so long as the small droplets continues to exist.

The initial distribution of the two droplet populations is characterized by a large but rapidly diminishing number of small droplets and evolves into one relatively stable population of large droplets which are slowly diminishing in size.

These results may serve to explain qualitatively the observed heat transfer phenomena near the return to nucleate boiling, the near-field-theories (17).

Droplet Size Distribution.

Various theories on the formation of droplets usually predict a single uniform size, cf. e.g. the critical Weber number mentioned above.

As it is noted above, droplets are generated in populations of various sizes. The droplets in a population generated by the same mechanism, may be expected to be clustered around a characteristic mean in a distribution which reflects the randomness in the process of generation, in other words be stochastic in nature.

Droplet size distribution can be represented by a plot of the number of droplets versus the diameter of droplets. The function representing the plot has various names in the literature: in the density function, the distribution curve or frequency function.

The plot function is a number distribution function of the droplets f(x) of a given diameter x. The total number of droplets is then

$$n = \int_0^\infty dn = \int_{-\infty}^\infty f(x)dx.$$

The arithmetic mean of the diameter is defined as

$$\overline{x}_d = \int_{-\infty}^\infty xf(x)dx / \int_{-\infty}^\infty f(x)dx = \frac{\int_{-\infty}^\infty xf(x)dx}{n}$$

the geometric mean diameter as

$$\ln x_g = \int_{-\infty}^{+\infty} \ln xf(x)dx / \int_{-\infty}^\infty f(x)dx.$$

The denominator is still simply equal to the total number.

In general a mean can be defined as

$$\bar{x}_{ab} = \int_{-\infty}^{\infty} x^a f(x)dx / \int_{-\infty}^{\infty} x^b f(x)dx.$$

If a is 3 and b 2 the mean most commonly used among the many averages is the Sauter mean diameter.

When using a statistical mean diameter to correlate data, it should be noticed , that it is important to use one that is relevant to the problem. The field of application of the Sauter mean diameter is in mass transfer and kinetics. When mass distribution is in question the mean diameter based on volume may be relevant, i.e. a is 3 and b zero. With respect to evaporation the diameter alone or the volume-to-diameter ratio may be relevant i.e.either a = 1, b = 0, or a = 3, b = 1 (92).

Experimental examinations of droplet distributions on probability paper show that droplet populations can be considered as a distributed logarithmic normal (log-normal distribution) (91) i.e.

$$\frac{dn}{d(\ln x)} = x \cdot \frac{dn}{dx} = x \cdot f(x) =$$

$$\frac{1}{\sqrt{2\pi} \cdot \sigma_g} \cdot \exp\left[-\frac{(\ln x - \ln\bar{x}_{ng})^2}{2\sigma_g{}^2} \right],$$

where $\bar{x}_{ng}$ is the number geometric mean diameter as defined above and σ_g is the geometric standard deviation, $\sigma_g = \ln\sigma$.

If the distribution is based on the volume of the droplets i.e.

$$V = \int_{o}^{n} k \cdot x^3 dn$$

then

$$\frac{dV}{d(\ln x)} = x \cdot \frac{dV}{dx} = xf(x^3) =$$

$$\frac{1}{\sqrt{2\pi}} \cdot \sigma_g \cdot \exp\left[-\frac{(\ln x - \ln\bar{x}_{vg})^2}{2\sigma_g^2} \right],$$

and

$$\frac{dV}{d(\ln x)} = kx^3 \cdot \frac{dn}{d(\ln x)} = kx^4 \cdot \frac{dn}{dx} = kx^4 \cdot f(x).$$

Using this on the number distribution gives:

$$\frac{dV}{d(\ln x)} = \frac{k}{\sqrt{2\pi}\,\sigma_g} \cdot \exp\left[-\frac{(\ln x - \ln\bar{x}_{ng})^2}{2\sigma_g^2} \right] -$$

$$\exp(3\ln x)$$

or

$$\frac{dV}{d(\ln x)} = \frac{k}{\sqrt{2\pi}\,\sigma_g^2} \cdot \exp\left[-\frac{(\ln x - (\ln\bar{x}_{ng} + 3\sigma_g^2))^2}{2\sigma_g^2} \right] \cdot$$

$$\exp\left(3\ln\bar{x}_{ng} + \frac{9}{2}\sigma_g^2\right)$$

A comparison of equation with the volume distribution shows that

$$\ln\bar{x}_{vg} \equiv \ln\bar{x}_{ng} + 3\sigma_g^2$$

if it can be shown that $k \cdot \exp(3\ln\bar{x}_{ng} + 9/2\,\sigma_g^2) \approx 1.0$.

If the distribution is based on surface the result would be:

$$\ln \bar{x}_{sg} \cong \ln \bar{x}_{ng} + 2\sigma_g^2$$

and for the Sauter mean, the relation is

$$\ln \bar{x}_{vsg} \cong \ln \bar{x}_{ng} + 2.5\sigma_g^2.$$

Other number distribution functions have also been used. The Nukiyama - Tanasawa distribution has the form (89):

$$f(x) = A \cdot x^m \exp(-b \cdot x^n).$$

A and b are normalization factors, whereas m and n are usually integers which sometimes can be given physical significance. This distribution function has been extensively used in pneumatic atomization.

C2. Droplet flow

In the following some discussion will be given on forces acting on droplets in the droplet-dispersed flow region. The discussion is by no means thought of as providing a thorough examination of the topic but will rather furnish a general overview of the phenomena with some deeper examinations of specific details.

In analyzing the forces acting on the droplets and the relative motion between the phases it is beneficial to start with an examination of the momentum equations for the two phases. In order to have a tractable set of equations these have to be derived from the general local instantaneous form of the momentum equations by applying some sort of averaging procedures, usually the Eulerian space and time averaging. In this way the microscopic local instant fluctuations of the fluid motion are eliminated resulting in equations describing the collective interactions of fluid particles. The averaging operations applied to the basic equations are commutative meaning that the order the averaging is carried out does not matter.

Space averaging could be done first followed by time averaging or vice versa without altering the result.

The derivation of the microscopic conservation equation can be found in different textbooks and reports, e.g. (93, 94,95). Here just one possible form of the obtained momentum equations will be given. If the space averaging is carried out for a slice with thickness Δz and cross-section equal to the constant channel area A (i.e. $\Delta V = A \cdot \Delta z$), the equation for conservation of z-direction (flow direction) momentum of phase k can be simplified to (93, 94):

$$\frac{\partial}{\partial t}(\alpha_k \langle \rho_k u_k \rangle) + \frac{\partial}{\partial z}(\alpha_k \langle \rho_k u^2_k \rangle) = -\alpha_k \cdot \frac{\partial \langle p_k \rangle}{\partial z} -$$

$$\frac{\partial}{\partial z}(\alpha_k \langle \tau_{zz,k} \rangle) + \alpha_k \langle \rho_k F_{z,k} \rangle + \langle u_k \Gamma_k \rangle_i +$$

$$+ \langle (\bar{n}_k \cdot \bar{\tau}_z) \rangle_i + \langle (\bar{n}_{kw} \cdot \bar{\tau}_z) \rangle_w + M_{ik} \qquad (1)$$

Here the angle brackets $\langle \rangle$ indicate quantites averaged over the volume ΔV. The two terms on the L.H.S. of eq. (1) are the temporal and spatial acceleration terms, respectively. The first term on the R.H.S. is the pressure force, the second represents the force due to viscous and turbulent stresses in the bulk of phase k, and the third term is the body force which in normal two-phase flow is limited to gravitational forces only. The fourth term on the R.H.S. represents the momentum transfer due to mass generation. The fifth term is the interfacial shear force. The sixth is the wall shear force and the seventh term represents the generalized drag force. Corresponding equations can be derived for the x- and y-directions.

For droplets in vapour surroundings it may be reasonable to assume that the term due to viscous and turbulent stresses inside the droplets are of minor magnitude in comparison with the remaining terms. Further, the interfacial shear force can be thought of as being inherently accounted for through the generalized droplet drag force M_{ik}.

Thus, the equation of motion in z-direction for the droplets (liquid phase ℓ) can be written as

$$\frac{\partial}{\partial t}\left[(1-\alpha)<\rho_\ell \; u_\ell \;>\right] + \frac{\partial}{\partial z}\left[(1-\alpha)< \; \rho_\ell u^2 \;_\ell>\right] = - \; (1- \; \alpha) \; \frac{\partial p}{\partial z} +$$

$$+ \; (1- \; \alpha)< \; \rho_\ell \cdot \; F_{z,\ell} \;>+<u_\ell \cdot \Gamma_\ell \;>_i \; + \; <(\bar{n}_{\ell w} \; \cdot \; \bar{\tau}_z>_w \; +M_{i\ell} \quad (2)$$

where also the void fraction α has been introduced:

$$\alpha \; = \; \alpha_v$$
$$1- \; \alpha \; = \; \alpha_\ell \qquad\qquad\qquad (3)$$

and the pressure has been assumed constant throughout the volume ΔV.

The interfacial transfer terms in eq. (2) can be related through the conservation equation across the interface, resulting in the jump conditions, whence

$$< \; \Gamma_\ell \; > \; + \; < \; \Gamma_v> \quad = 0$$
$$M_{i\ell} \quad + \quad M_{iv} \quad = 0 \qquad\qquad (4)$$

As these terms appear as source terms in eq. (2) in its vapour phase counterpart it is necessary to provide constitutive equations for Γ_ℓ and $M_{i\ell}$. The equation for $M_{i\ell}$ will be elucidated later on.

Equation (2) is given in the instantaneous volume average form or area average form if the thickness Δz of the slice is taken sufficiently small. The different terms can now be time averaged due to the commutative property of the averaging operators. In that operation the form of the equation remains exactly the same. Terms like

$$\frac{\partial}{\partial t} \; [(1-\alpha)< \; \rho_\ell u_\ell \;>)] \quad \text{become} \quad \frac{\partial}{\partial t} \; \overline{[(1-\alpha)< \; \rho_\ell u_\ell>]}$$

where the overbar denotes time or statistical averaging. In order to make eq (2) tractable it is necessary to separate an average of a product into a product of averages. This can be obtained by defining distribution coefficients of the form

$$C \equiv \frac{\overline{(1-\alpha)<u^2_\ell>}}{\overline{(1-\alpha)} \cdot \overline{<\bar{u}_\ell>}^2} \tag{5}$$

The distribution coefficients depend on the flow and void fraction profiles. To illustrate the magnitude of the distribution effects the coefficient C has been calculated for the power law velocity and void fraction profiles shown in figure 1 (from ref. (94)). For af flat velocity profile (m →∞) the distribution coefficient equals unity and it deviates significantly from unity only for very peaked velocity profiles. Thus, for high velocity droplet flow where the velocity profile usually is flat it seems reasonable to assume C=1.0. For lower velocities the distribution effect becomes increasingly important and then it is also necessary to incorporate the droplet concentration evaluated at the wall which has been shown to have pronounced influence on the distribution coefficient (96). It is felt that this wall concentration of droplets can be closely related to the liquid film breakdown at the locus of dryout and thus be one parameter when explaining the near and far field post-CHF heat transfer regions found in experiments.

Another approach for dealing with the distribution effects is to set up conservation equations for each part of a phase in which the distribution can be assumed fairly uniform (distribution coefficient set equal to unity). A study of the CHF phenomena using this approach can be found in (97). Thus the problem of treating the distribution coefficient is shifted to one of regarding transfer relationships between the separated parts of the two phases. This seems to be a more appealing approach especially for film-type flow regions like annular flow and for regions with an extremly peaked concentration profile like the subcooled boiling region.

In what now follows there will be a discussion of the constitu-

tive relationships for the wall friction and for the genera-
lized interfacial drag terms of eq. (2). It is necessary that
these momentum interaction terms are properly modeled, other-
wise the advantage of the two-fluid model over the mixture mo-
del disappears and, in certain cases, numerical instabilities
may occur (98).

Wall friction

The term $<(\bar{n}_{\ell w} \cdot \bar{\tau}_z)>_w$ in eq. (2) is the volume average wall
shear stress component in the z-direction for the liquid phase.
Thus this represents the portion of the wall friction caused
by droplets penetrating the boundary layer at the wall. In the
vapour phase momentum equation a corresponding term appears
which in the same way represent the portion of the total wall
friction caused by the vapour. Thus the problem arises of how
to make a proper partition of the overall two-phase friction
pressure drop between the two phases.

The normal way of expressing the overall two-phase friction
pressure drop is by means of two-phase friction multipliers.
Thus, the overall pressure drop can be expressed in terms of the
liquid- and vapour-alone wall friction pressure drop:

$$\left(\frac{\Delta p}{\Delta z}\right)_{TP} = \phi_\ell^2 \cdot \left(\frac{\Delta p}{\Delta z}\right)_\ell \tag{6}$$

$$\left(\frac{\Delta p}{\Delta z}\right)_{TP} = \phi_g^2 \cdot \left(\frac{\Delta p}{\Delta z}\right)_g \tag{7}$$

where ϕ_ℓ^2 and ϕ_g^2 are the liquid- and vapour-alone two-
phase friction multipliers, respectively, and

$$\left(\frac{\Delta p}{\Delta z}\right)_\ell = f_\ell' \cdot 1/2 \cdot \rho_\ell \cdot u_\ell^2 \cdot 1/D \tag{8}$$

$$\left(\frac{\Delta p}{\Delta z}\right)_g = f_g' \cdot 1/2 \cdot \rho_g \cdot u_g'^2 \cdot 1/D \tag{9}$$

The prime quantities are evaluated when each phase is assumed to flow alone in the channel (superficial velocities) i.e.

$$u_\ell' = (1 - \alpha) \cdot u_\ell \tag{10}$$

$$u_g' = \alpha \cdot u_g \tag{11}$$

and f_ℓ' and f_g' are functions of Reynolds number at velocities u_ℓ' and u_g', respectively.

The term $<(\overline{n}_{\ell w} \cdot \overline{\tau}_z)>_w$ is frequently approximated by the value obtained for steady flow with no evaporation. If eq (2) is applied to a volume $\Delta V = A \cdot \Delta z$ for those conditions it can be written as

$$-(1 - \alpha) \cdot \left(\frac{\Delta p}{\Delta z}\right)_{TP} + <(\pi_{\ell w} \cdot \tau_z)>_w + M_{i\ell}^* = 0 \tag{12}$$

where M_{il}^* is the static drag per unit volume

By means of eq. (6) and taking the limit as Δz approaches zero, it yields

$$<(\pi_{lw} \cdot \tau_z)>_w = \phi_\ell^2 \left(\frac{\partial p}{\partial z}\right)_\ell (1 - \alpha) - M_{i\ell}^* \tag{13}$$

A corresponding equation can be obtained for the vapour phase by means of eq. (7)

$$<(\pi_{vw} \cdot \tau_z)>_w = \phi_g^2 \left(\frac{\partial p}{\partial z}\right)_g \alpha - M_{iv}^* \tag{14}$$

These two equations provide the rationale for partition the overall two-phase friction pressure drop between the phases. The multipliers ϕ_ℓ^2, ϕ_g^2, may be interrelated through the Lockhart - Martinelli parameter, defined as

$$X^2 = \frac{\phi_g^2}{\phi_\ell^2} \tag{15}$$

For turbulent flow with the single phase friction factor as $f = C_o/Re^{0.2}$ this parameter can be expressed as

$$X_{tt}^2 = \left(\frac{1 - XE}{XE}\right)^{1.8} \cdot \left(\frac{\rho_g}{\rho_\ell}\right) \cdot \left(\frac{\mu_f}{\mu_g}\right)^{0.2} \tag{16}$$

The Generalized Drag Force

The generalized drag force in eq. (2) is expressed as a total force exchange per unit mixture volume. This can be related to af total drag force F_T per typical droplet by means of

$$M_{i\ell} = \frac{1 - \alpha}{V_d} \cdot F_T \tag{17}$$

where V_d is the volume of a typical droplet.

The force F_T can be divided into a number of forces some of which can be shown to have a pronounced influence on the numerical stability of the two-fluid model. Here the following forces will be dealt with: the skin and form drag force, virtual mass force, Basset force and forces due to asymmetrical evaporation. Additional forces may be taken into account if necessary for a specific analysis, e.g. diffusion forces due to concentration gradients may be important in slow flow if droplets are very nonuniformly distributed over the channel cross sectional area. It is assumed that the total drag force can be obtained simply by superposition of the included forces.

The Skin and Form Drag Force

This "standard" drag force acting on a droplet under steady
state conditions can be given as

$$F_D = - C_D \cdot \frac{\rho_\ell \cdot u_r \cdot |u_r|}{2} \cdot A_d \qquad (18)$$

where

C_D is a drag coefficient

A_d is the projected area of the droplet facing the flow

u_r is the relative velocity given by

$$u_r = u_\ell - u_v \qquad (19)$$

The total skin and drag force per mixture volume can be expres-
sed as

$$F_{TD} = - \frac{1 - \alpha}{V_d} \cdot C_D \cdot \frac{\rho_\ell u_r |u_r|}{2} \cdot A_d \qquad (20)$$

For a dispersed flow system it is common to define some im-
portant length scales (98, 99)

Sauter mean radius $\quad r_{sm} \equiv \dfrac{3 \cdot V_d}{A_i} \qquad (21)$

Drag radius $\qquad r_D \equiv \dfrac{3 \cdot V_d}{4 \cdot A_d} \qquad (22)$

Equivalent radius $\quad r_e \equiv \left(\dfrac{3}{4\pi} \cdot V_d\right)^{1/3} \qquad (23)$

Surface radius $\qquad r_s \equiv \left(\dfrac{A_i}{4\pi}\right)^{1/2} \qquad (24)$

Here A_i is the surface area of a typical droplet. For spherical
droplets these defined radii are all equivalent.
By introducing the area concentration given by

$$a_i = \frac{1-\alpha}{V_d} \cdot A_i \qquad (25)$$

eq. (20) can be written by means of eqs. (21) and (23) as

$$F_{TD} = - a_i \cdot \frac{C_D}{4} \cdot \frac{r_{sm}}{r_D} \cdot \frac{\rho_l \cdot u_r |u_r|}{2} \tag{26}$$

Thus the total skin and drag force per mixture volume is proportional to the interfacial area concentration and the drag force for the droplets. The ratio of the Sauter mean radius to the drag radius can be thought of as a shape factor for the droplets. For spherical droplets this shape factor equals unity.

It is evident that in order to have an accurate evaluation of F_{TD}, proper knowledge of the interfacial area concentration as well as the drag coefficient is essential. The problems concerning the area concentration are closely related to the droplet number density and are discussed in chapter C1. Here only a few comments on the drag coefficient will be given.

The Drag Coefficient

A thorough examination of the drag coefficient in different flow regions can be found in ref. (100, 101).

For a liquid droplet dispersed system there are two regions that have to be separated: the viscous region or undistorted droplet regions and the distorded droplet region. In the former the viscosity has a pronounced influence on the droplet motion, i.e. the drag coefficient is strongly dependent on the Reynolds number of the droplets. In the latter region C_D is essentially independent of Reynolds number.

For the viscous region two similarity hypothesis were introduced (100). First it was assumed that the drag coefficient C_D can be given as a function of the droplet Reynolds number

$$C_D = C_D (Re_d) \tag{27}$$

where the Reynolds number was defined in terms of the mixture viscosity μ_m as

$$Re_d \equiv \frac{2 \cdot \rho_v \cdot |u_r| \cdot r_d}{\mu_m} \tag{28}$$

The effect of other droplets results in additional deformation of the flow field. This deformation will give rise to additional stresses meaning that an original droplet sees an increase in the resistance to its motion which can be thought of as an increase of the viscosity. Thus, the mixture viscosity should be used when analyzing the motion of dispersed liquid droplets in vapour surroundings. The mixture viscosity can be calculated as (101):

$$\frac{\mu_m}{\mu_v} = (1 - \frac{\alpha_\ell}{\alpha_{\ell m}})^{-2.5 \cdot \alpha_{\ell m} \cdot \mu^*} \tag{29}$$

$$\mu^* = \frac{\mu_\ell + 0.4 \cdot \mu_v}{\mu_\ell + \mu_v} \tag{30}$$

where $\alpha_\ell = 1 - \alpha$ and $\alpha_{\ell m}$ is the maximum packing liquid volume fraction.

For droplets in a vapour flow it is reasonable to approximate μ^* to unity and $\alpha_{\ell m} \sim 0.62$ to 1.0 (98). If $\alpha_{\ell m}$ is assumed to equal unity the result for liquid droplets in vapour flow will become

$$\frac{\mu_m}{\mu_v} = \alpha^{-2.5} \tag{31}$$

The second similarity hypotheses introduced in (101) was that a complete similarity exists between a single-droplet system and a multi-droplet system. Therfore the functional form of C_D for a multi-droplet system is exactly the same as for a single-droplet system. Thus

$$C_D = 24 \frac{1 + 0.1 \cdot Re_d^{0.75}}{Re_d} \tag{32}$$

This correlation indicates that C_D increases with a decreasing vapour void fraction. For very small Reynolds number ($Re_d < 1$) eq. (32) reduces to the well-known Stokes drag law

$$C_D = \frac{24}{Re_d} \tag{33}$$

In the distorted droplet region the single-droplet drag coefficient depends only om droplet radius and fluid properties (101)

$$C_{D\infty} = \frac{4}{3} \cdot r_d \cdot \sqrt{\frac{g \cdot \Delta\rho}{\sigma}} \tag{34}$$

It was assumed (101) that for a multi-droplet system the increased drag due to other droplets was caused by the turbulent eddies in the droplets wake region in a similar way as for a solid-particle system and a multiparticle system, an equation for the drag coefficient of the multiparticle system was obtained in (101). Thus this equation combined with eq. (34) was assumed to be valid also for a multi-droplet system. By means of the approximation given by eq. (31) the following was obtained for a multi-droplet system (101):

$$C_D = \frac{4}{3} r_d \sqrt{\frac{g \cdot \Delta\rho}{\sigma}} \cdot \left[\frac{1 + 17.67 \cdot \alpha^{2.6}}{18.67 \cdot \alpha^3}\right]^2 \tag{35}$$

This correlation indicates that the momentum coupling between the phases increases with increasing droplet concentration (decreasing void fraction α).

For a single droplet in an infinite medium the viscous region extends up to about $Re_\infty = 10$ where

$$Re_\infty \equiv \frac{2r_d \cdot \rho_v |u_{r\infty}|}{\mu_v} \tag{36}$$

$$u_{r\infty} = u_\ell - u_{v\infty} \tag{37}$$

$u_{v\infty}$ is the undisturbed vapour velocity. For higher Reynolds number the drag coefficient is essentially constant, i.e. the distorted droplet region is prevailing. In this region the

drag coefficient is proportional to the droplet size. Thus, the upper limit of the drag coefficient is governed by the maximum size of the droplet. This droplet size can be determined from a critical Weber number:

$$We_{cr} \equiv \frac{2\ \rho_v \cdot u_r^2 \cdot r_d}{\sigma} = 12 \qquad\qquad (38)$$

The terminal velocity corresponding to eq (34) is

$$u_{r\infty} = \sqrt{2} \cdot \left[\frac{g \cdot \sigma \cdot \Delta\rho}{\rho_v^2} \right]^{1/4} \qquad\qquad (39)$$

Eqs. (38) and (39) thus yield

$$r_{dmax} = 3 \cdot \sqrt{\frac{\sigma}{g \cdot \Delta\rho}} \qquad\qquad (40)$$

which with eq. (34) gives the maximum drag coefficient $C_D=4$.

There is no thorough treatise in ref. (101) of how to handle the region transition for a multi-droplet system. A suggestion is to assume that the transition occurs at Re ~ 10, where the Reynolds number is based on the mixture viscosity according to eq.(28).

The above model was compared with one described by a large number of experimental data where satisfactory agreements were obtained for wide ranges of droplet concentration and Reynolds number (98, 101). Thus, the similarity hypothesis discussed above were concluded to be reasonable approach when developing the multidroplet drag coefficient.

Virtual Mass Force and Basset Force

The virtual mass force and the Basset force are transient forces occurring when a particle (bubble, droplet) is accelerating relative to the surrounding phase (liquid, vapour). When a droplet is moving in vapour surroundings these forces are usually very small compared, for instance, to the drag force. However, despite of its magnitude it has been shown

that the virtual mass force in particular has a pronounced influence on the numerical stability of the two-fluid model (102).

The virtual mass force can be explained briefly as follows: when a particle is set in motion relative to the surrounding medium it is given kinetic energy. In addition, the fluid which it displaces by its movement also is given a certain amount of kinetic energy. The total work done in accelerating the particle is therefore greater than if only the particle itself were moved, and the result is the same as if the mass of the particle were increased by a specified amount. This extra amount of mass is known as the added mass or induced mass of the particle, and the sum of the actual mass and the added mass is known as the virtual mass. It can be shown by potential flow theory (103) that for a sphere in unrestricted three-dimensional flow the added mass is half the mass of the fluid displaced by the sphere.

The forms of the virtual mass force and the Basset force for a collection of droplets simultaneously accelerating in the vapour phase are not firmly established. Newer and more adequate formulations of these forces are continually reported.

Zuber (104) studied the effect of concentration on the virtual mass force. From potential theory outlined in (105) and assuming low droplet concentration Zuber obtained an expression for the virtual mass force acting on one representative droplet as

$$F_V = -\rho_v \cdot V_\ell^* \cdot \frac{3-2\alpha}{\alpha} \cdot \frac{du_r}{dt} \tag{41}$$

where as before α is the vapour void fraction and u_r the relative velocity as in eq. (19). $\rho_v \cdot V_\ell^*$ is the added or induced mass for one droplet. For a spherical droplet V_ℓ^* can be expressed as

$$V_\ell^* = \frac{1}{2} \cdot \frac{\pi}{6} \cdot (2 \cdot r_{sm}) \tag{42}$$

Equation (41) is valid for accelerating a spherical droplet in the centre of a vapour-filled hollow fixed sphere. The radius of the hollow sphere is taken so that at this distance from the droplet the vapour is assumed to be undisturbed.

In ref. (106) a reinterpretation of Zuber's result is made where the induced vapour flow caused by the droplet motion was also taken into account. From this analysis the virtual mass force became

$$F_V = -\rho_v \cdot V_\ell^* \cdot \alpha \; \frac{du_r}{dt} \tag{43}$$

In ref. (101) a new form of F_V is proposed based on Zuber's result and the work reported in (102). The resulting equation is

$$F_V = -\rho_v \cdot V_\ell^* \cdot \frac{3-2\alpha}{\alpha} \cdot (\frac{\partial u_r}{\partial t} - u_r \cdot \frac{\partial u_v}{\partial z}) \tag{44}$$

Equations (43) and (44) reveal quite a different trend when the void fraction decreases (droplet concentration increases). For decreasing void fraction the virtual mass force decreases accordingly to eq. (43) while it increases following eq. (44). Which one is most accurate is not readily pointed out. They represent both small terms compared to other forces and contribute only by a minor amount to the numerical result while their influence on the numerical stability is quite definite. In view of both their small magnitude for droplet dispersed flow and the overall uncertainty concerning the droplet shape and size distributions in full-scale systems it is not worthwhile to examine this issue more deeply here. Thus, the different formulations, eqs. (43) and (44), can be taken as evidence on the uncertainty in the present state of the art and it is expected that further research will shed more light on these phenomena.

The Basset force is the result of acceleration on the viscous drag and boundary layer development around the droplets. This

force can be expressed as (c.f. ref. (104))

$$F_B = -6 \cdot r^2 \sqrt{\pi \; \rho_v \cdot \mu_m} \int_t \frac{du_r}{d\xi} \cdot \frac{d\xi}{\sqrt{t-\xi}} \qquad (45)$$

where r is the droplet radius and μ_m the mixture viscosity according to eqs. (29) and (30). The integration is carried out for the acceleration time span.

In ref. (104) an analysis is carried out to find out under what conditions the Basset force can be neglected in comparison with the virtual mass force. By means of the mean value theorem of integral calculus the integral of eq. (45) can be related to the time function:

$$\int_o^t \frac{du_r}{d\xi} \frac{d\xi}{\sqrt{t-\xi}} \leq 2 \cdot \frac{du_r}{dt} \cdot \sqrt{t} \qquad (46)$$

By comparing the Basset force using eq. (46) with the virtual mass force, eq. (44), assuming that the spatial derivative is zero the following is obtained:

$$t \leq \frac{1}{216} \cdot \frac{\rho_v \cdot V_\ell^*}{\pi^2 \cdot r \cdot \mu_m} \left(\frac{\alpha}{3-2\alpha} \right)^2 \qquad (47)$$

As long as the acceleration time t obeys eq. (47) the Basset force can be neglected. Normally for fast transients in droplet-dispersed flow eq. (47) is fulfilled and thus the Basset force is of minor importance.

Evaporation Forces

The evaporation forces have transverse directions resulting in droplet movements in a plane normal to the flow direction away from the heat transfer surface. Because of the high temperature gradient inside the thermal boundary layer at the heat transfer surface a droplet residing within this layer will experience a nonuniform evaporation. The droplet side facing the heat transfer surface will have a higher vapour generation than the opposite

droplet side resulting in different vapour velocities normal to the droplet surface. This will create a force with a tendency to push the droplet away from the heat transfer surface. It can be expected that these evaporation forces give rise to substantial droplet transversal trajectories at the locus of CHF when the wall liquid film is boiled off and thus can be one major aspect to be taken into account when modelling the near- and far-field post-CFH heat transfer regions observed in experiments (17).

The derivation is quite straightforward. In (107) a linear temperature gradient within the thermal boundary is assumed:

$$T = T_{SAT} + (T_w-T_{SAT}) \cdot (1- \frac{y}{\delta}) \tag{48}$$

and by assuming a constant heat transfer coefficient between the droplet surface and superheated vapour an integration of vapour generation for each half of the droplet yields the following average vapour velocities normal to the wall surface

$$u_h = \frac{h}{H_{fg} \cdot \rho_v} \cdot (T_w-T_{SAT})[(1- \frac{y}{\delta}) + \frac{d}{4\delta}] \tag{49}$$

$$u_c = \frac{h}{H_{fg} \cdot \rho_v} \cdot (T_w-T_{SAT})[(1- \frac{y}{\delta}) + \frac{d}{4\delta}] \tag{50}$$

for the hot and cold side of the droplet, respectively.

These velocities give rise to a resulting accelerating force according to

$$F_E = \rho_v \cdot \frac{\pi d^2}{4} (u_h^2-u_c^2) \tag{51}$$

By means of eqs. (49) and (50) the force is obtained as

$$F_E = \frac{\pi d^2}{4} \cdot \frac{h^2}{H_{fg}^{2} \cdot \rho_v} (T_w-T_{SAT})^2 \cdot \frac{d}{\delta} \cdot (1- \frac{y}{\delta}) \tag{52}$$

This force is expressed for one droplet and is of course active only within the boundary layer.
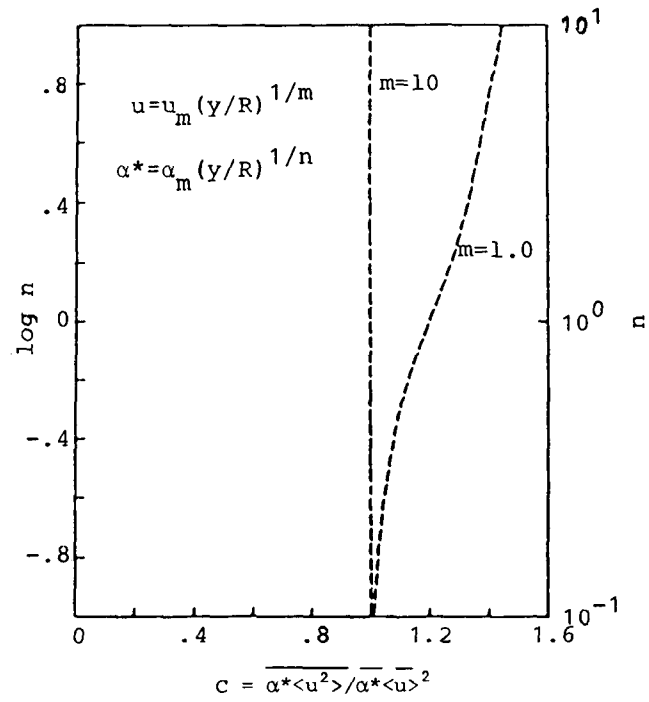
Distribution coefficient for various velocity and void fraction profiles.

From ref (2)

FIGURE C2.1

C3. Droplet flow heat transfer.

The problems of heat transfer will be considered here in general.
Some correlations are proposed, but no evaluations with a com-
puter programme including these correlations have been performed.
In order to find the best fit correlation comparisons with
experiments are needed using a computer programme including
different proposed correlations. The correlations discussed
are representative in such a way that they have been used in
several two-fluid programmes or in simple mechanistical program-
mes for the modelling of droplet-dispersed flow heat transfer.

The examination of the modelling of heat transfer must start
with the energy equation for two-phase flow. The equations are
derived as local, instantaneous differential equations for
three-dimensional flow. The equations are written in an
Eulerian form, where the diffusion term is neglected. The real
physics cannot be calculated using microscopic volumes in a
class of few millimeters, which is the scale of basic subpro-
cesses in two-phase flow. For microscopic volume used in
calculating different kinds of averaging procedures must be
used, including both averaging in space and time. In this
chapter two averaging procedures for space will be defined.
The volume averaging denoted with angle brackets (<>) means
instantaneous averaged conditions in the volume. The time
average denoted with an overbar ($^-$) means the statistical
average value for the volume average, e.g. that resulting from
many repeated measurements with same experimental conditions.
The time averaging is possible before volume averaging, too.
The local temperature measurement with a single thermocouple
is an example of this.

The thermocouple may give a good average for the local tem-
perature, but the value may not be representative as a volume
average. The generalized conservation equations for two-phase
flow system may be written as (93)

$$\frac{\partial}{\partial t}\left(\alpha_k \langle \rho_k \Psi_k \rangle\right) + \frac{\partial}{\partial z}\left(\alpha_k \langle n_z \cdot \left(\rho_k \ \Psi_k v_k + j_k\right)\rangle\right) + \alpha_k \langle \rho_k S_k \rangle$$

$$= - \frac{1}{V} \int_{a_i} (\dot{m}_k \ \Psi_k + \bar{j}_k \cdot \bar{n}_k) dS - \frac{1}{V} \int_{a_{kw}} \bar{n}_{kw} \cdot \bar{j}_k dS$$

The $\rho_k \ \Psi_k$ is a generalized phase quantity to be considered, α_k the phase volume fraction defined as a instantaneous volumetric fraction for the phase ($\equiv \langle \alpha_k \rangle$), n_z the direction vedtor in the axial direction, n_k the direction vector perpendicular to the interphase surface, j_k the flux of Ψ_k, and S_k the source of Ψ_k.

The interfacial mass transfer rate may be written as

$$\dot{m}_k = \rho_k n_k \cdot (v_k - v_i)$$

The generalized form may be used for the derivation of the conservation equations for each quantity, as mass, momentum in the z direction, and energy. The quantities Ψ_k, j_k and S_k have separate meanings for the mass conservation equation, momentum conservation equation, and energy conservation equation. Here only the energy conservation equation will be considered.

For the energy equation the generalized terms are:

$$\Psi_k = E_k = (e_k + u_k^2/2)$$

$$\bar{j}_k = \dot{\bar{q}}_k + (p_k \bar{\bar{I}} - \tilde{\tau}_k) \cdot \bar{v}_k$$

$$S_k = \bar{F}_k \cdot \bar{v}_k + Q_k$$

Here e_k is internal energy ($e \equiv h - p/\rho$), q_k heat flux to phase k, p_k pressure of phase k, I identity tensor, τ_k stress tensor, Q_k heat source in the fluid, F_k external force like gravity potential in the fluid, v_k velocity field in the fluid, and u_k the velocity component in the z-direction.

In addition to the volume averaging, volume-averaged quantities have been defined in the equation over both the interfacial and wall contact areas. These integrals are included into the generalized equation. The volume averaging discussed earlier is defined by an integral

$$< \ > \ = \ 1/V \int \ (\ \ )$$

Further, the interfacial jump conditions are needed for two phase flow. The generalized jump conditions may be expressed as:

$$\sum_{k=1}^{2} \ (\rho_k \overline{\Psi_k}(\overline{v}_k - \overline{v}_i) + \overline{j}_k) \cdot \overline{n}_k = 0$$

The averaging procedure is needed as well for interfacial jump conditions as for the original conservation equations. A discussion is needed for further understanding of two-phase physics of what is vanishing from physical reality due to other simplifications during the averaging process.

The real two-phase flow includes a high degree of turbulence. Both volume- and time-averaging do not take this subprocess into account. This process may be significant for the mixing and is the origin for the crosswise movement of droplets causing the impingment on the wall and enchances the wall heat transfer.

The volume average describes only one velocity component for each phase in each coordinate direction and then the information on real velocities for different droplet sizes vanishes. If this information should be conserved, the conservation equations for a single liquid have to be split into equations for two droplet classes. The method based on distribution functions will be discussed later. If different field equations for one phase have been derived, a question may arise as to which interfacial jump conditions are valid between different droplet classes and between droplet. The impingment may be expected

to cause mass transfer and momentum transfer terms between fractions, but modelling problems for energy equation may be overstated due to small enthalpy differences.

In further simplifications the phase pressures are assumed to be the same, i.e. $p = p_1 = p_2$. Then in the interfacial jump condition, the differential terms for the phase pressures $<p_{1i}> - <p_{2i}>$ vanishes. This pressure difference between phases is significant in the energy equation during rapid blowdown conditions, when the initiation of flashing is delayed. The pressure inside microscopic vapour bubbles is higher than in the water, corresponding to the difference in saturation temperature of 3....10 K. If different phase pressure are not calculated, the delay has to be included into interfacial heat transfer correlations.

The water pressure inside droplets is slightly higher than in the vapour pressure around them, depending on the surface tension and droplet diameter. This is the reason, why a cloud of very small droplets may exist in superheated vapour for quite a long time without evaporation. The mass of these micro-size droplets is small, however, and they are not needed to be considered separately in the energy conservation equation.

After assuming same phase pressures the only pressure terms in the energy equation are

$$\frac{\partial}{\partial z}\left(\alpha_k <p_k u_k>\right) \text{ and } <p_k> \frac{\partial \alpha_k}{\partial t}$$

The kinetic energy conservation equation is usually used together with the momentum conservation equation for modelling pressure losses of the real structure. The pressure losses in venturis and area changes may be changed to reversible and irreversible pressure losses.

The generalized conservation equation cannot be used for comparison with experimentally measured parameters, because usual instruments measure only local parameters which may be time averaged e.g. a gamma beam void fraction measurement where the single beam signals may be considered as time averaged and the volume average has to be calculated as a combination of parallel time averages.

The time average for main parameters, velocity and enthalpy, are defined as

$$\overline{<u_k>} = \frac{\overline{\alpha_k <u_k>}}{\overline{\alpha_k}}$$

$$\overline{<h_k>} = \frac{\overline{\alpha_k <h_k>}}{\overline{\alpha_k}}$$

Because the main parameter can be directly chosen as time average in conservation equations, no further interpretation is needed between primitive and averaged parameters in equations. The problem is how to formulate time averages for terms consisting of products of several main parameters. It is well known from the combination rule, that the average of a product is not equal to the product of two averages. Theorists have proposed a solution to overcome the combination rule by the use of distribution parameters that take into account the different conditions over the cross section.

The distribution parameters may be used both in momentum and energy conservation equations. There is a disadvantage, however, that distribution parameters defined for different subprocesses differ unless the processes are analogous. The convective term in the differential equation needs the averaging of $<\alpha_k><h_k u_k>$.

The distribution parameter for the energy equation requires e.g. the distribution parameter

$$C_k = \frac{\overline{\alpha_k \langle h_k u_k \rangle}}{\overline{\alpha_k} \langle h_k \rangle \langle u_k \rangle}$$

The corresponding distribution parameters are needed for the interfacial jump condition, as for the interfacial surface area. In practice very few data distribution parameters exists and the parameter in computer models is usually set to unity. The situation typically reflects disagreements between theorists and programme developers. Although a theorist recommends the use of distribution parameters for the complicated two-phase flow form including droplet and film fields, the programme developer may find it easier to use split field equations.

The use of distribution parameters is easier for a droplet field that consists of several droplet sizes. Then the log-normal distribution can be used as a basis in the calculation of distribution parameters.

The distribution parameter becomes significant for vapour enthalpy convection if a nonflat vapour temperature profile must be expected over the cross section. This is possible, e.g. in a rod bundle, where the periphery of the bundle is not so hot as the central part.

For the discussion of problems in modelling of interfacial heat transfer the interfacial area is very essential, because the heat flux is expressed as a product of heat transfer coefficient, interfacial surface area and temperature difference between superheated vapour and interfase. The interfacial area is related to void fraction and droplet diameter by:

$$A_i = n \, \pi \, d^2 = \frac{6 \, (1 - \alpha)}{d}$$

The question that arises is: How well is the droplet size distribution known for different void fraction regions? In many models the average droplet size is calculated from the Weber number criteria using phase velocity difference as a parameter, and further, the differential velocity is calculated from the drag gravity balance, as in TRAC using (10)

$$V_r = \frac{4(\rho_\ell - \rho_g)g \; d}{3 \; \rho_g}$$

One possible problem may be mentioned, however. The Weber number criterion is perhaps some kind of time average in limited experimental conditions. The interfacial drag models are based typically on measurement with solid spheres in gas stream. The combination of these two criteria may work poorer in computer programmes than it is generally believed. The Weber criterion in particular is not easy to apply in computer programmes because the droplet size is a drastic function of the velocity difference. The phase separation model before the droplet entrainment must be well fitted to theWeber number criterion, in order to give the correct velocity difference between phases. Some experiments for reflooding indicate that the droplets typically have a size of 1...3 mm. Using Weber the number criterion only a narrow range of velocity differenses is then possible.

Because interfacial heat transfer depends on the interfacial area, the integration method should conserve the interfacial area in the convection term. The need is similar for the interfacial momentum conservation. The mass conservation equation does not directly give the droplet size as solution. Then an extra equation is needed for this, unless the distribution parameters solve the problem.

In the heat transfer coefficient between interfases, only the heat transfer resistance from vapour to droplet surface is significant and the heat transfer resistance from the droplet surface into liquid is negligible. Then it follows that practically liquid is saturated in dispersed flow. If cold liquid is injected to saturated or superheated vapour the subcooling may be assumed to vanish at once by condensation.

The correlations using droplet Reynolds number may be recommended for the interfasial heat transfer. As an example the correlation of Lee and Ryley may be mentioned (108)

$$Nu_d = 2 + 0.74 \, Re_d^{0.5} \, Pr_g^{0.3}$$

The correlation is based on measurements with solid spheres in a gas stream. There is one advantage in this kind of correlation: The heat transfer rate is proportional to the square root of the velocity difference. This dependency makes the iteration process more stable than, e.g. the nucleate boiling heat transfer as it is proportional to the second power of temperature difference. The Reynolds number is defined as:

$$Re_d = \frac{d(u_g - u_d) \, \rho_g}{\mu_g}$$

In the wall heat transfer two components have to be separated, the heat flux to vapour and the heat flux directly to liquid. The first assumption is that the wall is superheated so much that droplets cannot wet the wall.

The heat transfer to vapour is a product of surface area heat transfer coefficient, and temperature difference. The first approach is to use Reynolds' analogy between wall friction and wall heat transfer. Reynolds' analogy is expressed by $St = 0.5 \, f_w$. The modified Reynolds' analogy proposed by Blair is (108)

$$St = 0.5 \, f_w \, (1.18 + 1.3 \, T)$$

$$St = Nu/(Re \, Pr)$$

Here f_w means the Fanning friction and T turbulent intensity of free stream ($T = \sqrt{u'^2} / u$). The Dittus-Boelter correlation is one result of Reynolds' analogy. For wall to vapour heat transfer in dispersed flow the Dittus-Boelter correlation is not the best choice, but rather the modification of it. In (48) the Dougall-Rohsenow correlation is recommended:

$$Nu_g = 0.023 \ Re^{0.8} \ Pr_g^{0.4}$$

$$Re = \frac{D \ G}{\mu_g} \ (XE + \frac{\rho_g}{\rho_\ell} \ (1 - XE))$$

There are some models like that of Chen & Webb and that of Hein, which tend to correlate the interfacial heat transfer without any specific droplet size. The models are empirical. In SÄK-5 tests with NORA programme good results were obtained by using the Chen & Webb model. The explanation for the success without droplet diameters may be, that in reality the droplet size spectra in free flow is quite narrow, without the break-up caused by structures. Only in spray nozzles and close to restrictions (like spacers) may a wider droplet size spectrum be expected.

The heat transfer between wall and liquid consists partly of radiation and partly of direct contact with the wall. The calculation is simpler for radiation because the heat absorption to droplets is only a function of void fraction and temperature difference. The formulation of radiation heat transfer is well presented by Sun & Conzales (109).

The direct contact heat transfer to liquid would be correlated as a product of time-averaged contact area, heat transfer coefficient, and temperature difference. The heat transfer mode is quite difficult to handle. The time-averaged contact area is a function of droplet density and radial droplet velocity caused by turbulence. The turbulent velocity components for the liquid flow are not known as well as for the gas flow. Some experiments have been made for droplets impinging on a hot surface. From these experiments quite sophisticated models have been formulated. The formulation is perhaps too complicated to be used in computer models. If Reynolds' analogy is assumed for the dispersed flow (homogenous approximation), the Dougall-Rohsenow correlation predicts the heat flux to vapour-liquid mixture well.

The direct liquid contact heat transfer has been applied in many programmes. The model is very simple in the German re-flooding programme FLUT. Varone (110) has used a complicated model proposed by Kendall & Rohsenow in his own programme.